

UNIVERSITY OF OKLAHOMA  
GRADUATE COLLEGE

UNMANNED AERIAL VEHICLE-BASED FAR-FIELD ANTENNA  
CHARACTERIZATION SYSTEM FOR POLARIMETRIC WEATHER RADARS

A DISSERTATION

SUBMITTED TO THE GRADUATE FACULTY

in partial fulfillment of the requirements for the

Degree of

DOCTOR OF PHILOSOPHY

By

ARTURO YOSHIYUKI UMEYAMA MATSUMOTO

Norman, Oklahoma

2020

UNMANNED AERIAL VEHICLE-BASED FAR-FIELD ANTENNA  
CHARACTERIZATION SYSTEM FOR POLARIMETRIC WEATHER RADARS

A DISSERTATION APPROVED FOR THE  
SCHOOL OF ELECTRICAL AND COMPUTER ENGINEERING

BY THE COMMITTEE CONSISTING OF

Dr. Jorge L. Salazar-Cerreno

Dr. Caleb J. Fulton

Dr. Robert D. Palmer

Dr. Boon Leng Cheong

Dr. Phillip B. Chilson

Dr. Rouzbeh G. Moghanloo

© Copyright by ARTURO YOSHIYUKI UMEYAMA MATSUMOTO 2020  
All Rights Reserved.

*To my family and friends.*

## IEEE Copyright Notice

The contents of two journal papers were reused substantially in Chapters 3 and 4 of this work. The papers, for which I am the first author, have been slightly modified in structure to accommodate the dissertation format.

Chapter 3 is composed primarily of material extracted from [1] (©2020 IEEE), with additional or modified figures, and analysis. Chapter 4 is composed primarily of material extracted from [2] (©2020 IEEE).

## Acknowledgments

First and foremost, I would like to thank my advisors Dr. Jorge Salazar, and Dr. Caleb Fulton, for allowing me to pursue my PhD education, and letting me take charge of this ambitious research topic, always providing excellent mentoring and guidance to ensure my personal, academic, and professional success. I will be forever grateful for this opportunity I have been given. Thanks to Dr. Robert Palmer, and the members of my committee for providing support and insights to constantly improve the quality of my work.

Additional thanks to my friends and colleagues at the ARRC: Dr. Rodrigo Lebrón, Dr. Javier Ortiz, José Díaz, Antonio Segalés, Dr. David Schwartzman, Dr. Andrew Byrd, for being my family away from home. I will always remember your support when I needed some cheering up.

To everyone who assisted me in the SENSR-UAV project, in particular to Brenton Wolf, whose help was invaluable for this research, and Antonio Segalés for enabling the successful completion of this project.

And last but not least, I am forever grateful to my family, especially my parents, Yukiko and Shigeki, for always encouraging me to venture out and take opportunities to further advance in life.

This work was sponsored by the US Spectrum Efficient National Surveillance Radar (SENSR) program through NOAA/NSSL and the FAA.

## Abstract

The use of phased array radars for the US weather radar network (NEXRAD) has been proposed in lieu of the current mechanically steered dish-based systems, owing to its many attractive features, e.g., electronic steering and fast update rates, and others. Scatterer identification (hydrometeors and non-hydrometeors), accurate estimation of rainfall rates, and determination of propagation effects is possible in weather radars through polarimetry. However, the existence of cross-polarization, and co-polarization mismatch in the H- and V-polarization radiation patterns introduces biases in the polarimetric weather radar products, which can adversely affect the accuracy of the estimates of byproducts, thus imposing strict antenna requirements on the co-polarization mismatch of no greater than 0.1 dB, and cross-polarization levels of no greater than about -45 dB. Since the radiation characteristics of phased arrays are inherently dependent on the scanning direction, it becomes even more challenging to meet these requirements. Furthermore, ensuring that each system in this large network meets the requirements becomes an additional challenge where accurate characterization and calibration will be critical. Clearly, the system and instrumentation used for characterization also need to meet or exceed the system level requirements to provide reliable weather-radar-based estimates.

Given that radar and other communications systems require in-situ calibration, it is hypothesized that a UAV-based antenna measurement system is able to replace conventional outdoor ranges in virtue of its low cost and flexibility of operation. The proposed solution is a UAV-based in-situ antenna characterization system with the necessary RF instrumentation to perform accurate measurements of a typical weather radar, along with general guidelines and procedures to ensure optimal results. This solution attempts to provide a portable and cost-effective alternative to conventional outdoor antenna ranges, which can be deployed in multiple sites with few to no modifications. While previous works in the literature have had successful results in

the use of UAVs for far-field (FF) antenna measurements in a variety of operating frequencies, no other work has currently shown the RF performance needed to meet the stringent requirements expected in an application such as polarimetric weather radars. It is shown in this work, that the characterization and calibration of real polarimetric weather radar systems is possible to a high degree of accuracy set forth by the most critical requirements, i.e., co-polarization mismatch no greater than 0.1 dB and cross-polarization levels below -45 dB.

# Contents

<b>List Of Tables</b>	<b>xiii</b>
<b>List Of Figures</b>	<b>xiv</b>
<b>1 Introduction</b>	<b>1</b>
1.1 Motivation . . . . .	1
1.2 Literature Review . . . . .	4
1.3 Problem Statement . . . . .	7
1.4 Research Scope . . . . .	8
1.5 Contribution . . . . .	9
1.6 Dissertation Overview . . . . .	10
<b>2 Fundamentals</b>	<b>12</b>
2.1 Antenna Measurements . . . . .	12
2.1.1 Coordinate Systems . . . . .	13
2.1.2 Pattern Cuts . . . . .	15
2.1.3 Field Regions . . . . .	15
2.1.4 Polarization . . . . .	16
2.1.5 Friis Transmission Equation . . . . .	18
2.1.6 Radar Range Equation . . . . .	19
2.2 Phased Array Antennas . . . . .	20
2.2.1 The Array Pattern . . . . .	20
2.2.2 Array Scanning . . . . .	21
2.2.3 Beamwidth and Directivity . . . . .	22
2.3 Polarimetric Weather Radar . . . . .	23
2.3.1 Polarimetric Radar Variables . . . . .	24
2.3.2 Polarimetric System Requirements . . . . .	27
2.3.3 Basic Signal Model . . . . .	28
2.3.4 Basic Calibration Process . . . . .	29
2.4 Summary . . . . .	30
<b>3 Guidelines, Simulation and Error Analysis</b>	<b>31</b>
3.1 FF Guidelines for UAV-based Measurements . . . . .	32
3.1.1 Design Considerations . . . . .	33
3.1.1.1 Effect of Phase Curvature . . . . .	33

3.1.1.2	Effect of Transverse Amplitude Taper . . . . .	34
3.1.1.3	Effect of Ground Reflections . . . . .	35
3.1.1.4	Summary of Criteria . . . . .	36
3.1.2	RF Instrumentation . . . . .	36
3.1.2.1	Transmitting and Receiving Subsystems . . . . .	37
3.1.2.2	Positioning, Recording, and Data-processing Subsystems . . . . .	38
3.1.3	Procedures . . . . .	38
3.2	Simulation Framework . . . . .	40
3.2.1	Basic Signal Model . . . . .	41
3.2.1.1	AUT and Probe Antennas . . . . .	41
3.2.1.2	Transmission Model . . . . .	42
3.2.2	UAV Structure Influence . . . . .	43
3.2.3	Error Sources . . . . .	44
3.2.3.1	Coupling . . . . .	44
3.2.3.2	Extraneous Reflections . . . . .	46
3.2.3.3	Position and Orientation Misalignment . . . . .	48
3.2.4	Total Measured Signal . . . . .	49
3.3	Analysis . . . . .	49
3.3.1	Probe in Elevated Range . . . . .	50
3.3.2	Probe Mounted on a UAV . . . . .	52
3.3.2.1	Hover Mode . . . . .	52
3.3.2.2	Vertical Grid Mode . . . . .	54
3.3.3	Misalignment Error Analysis . . . . .	56
3.3.4	Discussion . . . . .	59
3.4	Summary . . . . .	61
<b>4</b>	<b>Frame, Gimbal and Probe Antenna Coupling</b>	<b>63</b>
4.1	Simulations . . . . .	64
4.1.1	Dipole . . . . .	65
4.1.2	Microstrip Patch . . . . .	67
4.1.3	Patch Array Antenna . . . . .	69
4.1.4	Horn . . . . .	70
4.2	Performance Analysis . . . . .	71
4.2.1	Description of Metrics . . . . .	71
4.2.1.1	Co-polarization Mismatch . . . . .	71
4.2.1.2	Ripples . . . . .	72
4.2.1.3	Cross-polarization Metrics . . . . .	73
4.2.2	Analysis . . . . .	74
4.2.2.1	Dipole . . . . .	74
4.2.2.2	Patch . . . . .	76
4.2.2.3	Array . . . . .	78
4.2.2.4	Horn . . . . .	80
4.2.3	Probe Selection . . . . .	82
4.3	Measurements . . . . .	84

4.3.1	Follow Mode . . . . .	84
4.3.2	Tracking Mode . . . . .	88
4.4	Summary . . . . .	90
<b>5</b>	<b>System Description and Operations</b>	<b>93</b>
5.1	Platform History . . . . .	94
5.1.1	DJI Phantom 3 Professional (2015-2016) . . . . .	94
5.1.2	OU-UAVRF1250 (2016-2017) . . . . .	96
5.1.3	DJI S900 (2017-2019) . . . . .	98
5.1.4	DJI Matrice 600 Pro (2019-present) . . . . .	100
5.2	System Description . . . . .	100
5.2.1	Mechanical Subsystem . . . . .	101
5.2.1.1	UAV and Gimbal . . . . .	101
5.2.1.2	Positioning Performance . . . . .	104
5.2.1.3	Orientation Performance . . . . .	107
5.2.2	RF Subsystem . . . . .	108
5.2.2.1	Probe Antenna: “Stop Sign” . . . . .	108
5.2.2.2	Signal Generator . . . . .	110
5.2.2.3	Polarization Switch: “Twitchy” . . . . .	111
5.2.2.4	Receivers . . . . .	111
5.3	Outdoor Operations . . . . .	113
5.3.1	Methodology . . . . .	114
5.3.1.1	Hover Mode . . . . .	114
5.3.1.2	Circular Mode . . . . .	117
5.3.1.3	Vertical Grid Mode . . . . .	119
5.3.1.4	Other Modes . . . . .	121
5.3.2	Results . . . . .	126
5.3.2.1	Fixed Reference . . . . .	127
5.3.2.2	UAV Hover Mode . . . . .	129
5.3.2.3	UAV Circular Mode . . . . .	131
5.3.2.4	Analysis . . . . .	133
5.4	Summary . . . . .	135
<b>6</b>	<b>UAV-based Measurements of Real Systems</b>	<b>136</b>
6.1	Cylindrical Polarimetric Phased Array Radar (CPPAR) . . . . .	137
6.1.1	UAV Hover Mode . . . . .	140
6.1.2	Analysis . . . . .	143
6.2	Summary . . . . .	147
<b>7</b>	<b>Epilogue</b>	<b>149</b>
7.1	Conclusion . . . . .	149
7.2	Future Work . . . . .	153

<b>A Part 107 Regulations</b>	<b>168</b>
A.1 General . . . . .	168
A.2 Operational Limitations . . . . .	169
A.3 Remote Pilot in Command Certification and Responsibilities . . . . .	171
A.4 Aircraft Requirements . . . . .	173
A.5 University Research Operation Requirements . . . . .	173

## List Of Tables

1.1	Summary of work related to UAV-based antenna measurements. . . .	6
2.1	Summary of polarimetric requirements. Adapted from [4]. . . . .	27
3.1	Summary of design considerations for UAV-base antenna measurements.	36
4.1	Summary of relevant performance metrics. . . . .	82
5.1	M600P platform specifications. . . . .	102
5.2	Ronin-MX gimbal specifications. . . . .	103
5.3	Standard deviations of the UAV positions for different ground locations.	104
5.4	Flight performance for hover mode under S 21 mph winds for GPS and RTK. . . . .	107

## List Of Figures

2.1	Typical coordinate systems used in antenna measurements and in weather radar. . . . .	14
2.2	Radiating field regions of an antenna. . . . .	16
2.3	An illustration of the Friis transmission equation geometry. . . . .	18
2.4	An illustration of the radar range equation geometry for a monostatic configuration. . . . .	19
2.5	An illustration of the generalized array configuration. . . . .	21
2.6	An example of a polarimetric weather radar PPI scan depicting the radar products: $Z_H$ (top-left), $\bar{v}_r$ (top-right), $Z_{DR}$ (bottom-left), and $\rho_{HV}$ (bottom-right). Extracted from [73] with permission. . . . .	25
3.1	FF measurement configuration for the UAV, probe antenna, and AUT. The sketch depicts a spherical wave front leaving the probe antenna and impinging on the aperture of the AUT. . . . .	34
3.2	(a) Geometry for two radiating elements at the extremes of the arms of an hexacopter. (b) Antenna pattern for probe (co-polarization, solid; cross-polarization, dashed), and probe mounted on UAV (co-polarization, dash-dotted; cross-polarization, dotted). . . . .	45
3.3	Generic measurement setup and geometry of the ground-reflected rays.	47
3.4	Case of the probe in an elevated range. (a) Simulated measurements with (blue, red) and without (black) errors for H-polarized (blue) and V-polarized (red) antenna patterns, with top lines corresponding to co-polarization patterns, and bottom lines corresponding to cross-polarization patterns. (b) Zoomed-in plot. . . . .	52
3.5	Case of the probe mounted on a UAV. (a) Simulated UAV-based measurements with (blue, red) and without (black) errors for H-polarized (blue) and V-polarized (red) antenna patterns, with top lines corresponding to co-polarization patterns, and bottom lines corresponding to cross-polarization patterns. (b) Zoomed-in plot. . . . .	53
3.6	Normalized variations for the different directions in the $x$ - (east), $y$ - (north), and $z$ - (north) axes as function of the bias in position for: (a) co-polarization mismatch levels, and (b) cross-polarization level increment. . . . .	54
3.7	(Top) Sketch of the scanning grid, and the simulated co-polar mismatches at a distance of $x = 425.15$ [m] without (left) and with (right) measurement errors. . . . .	56

3.8	Normalized variations as function of the bias in gimbal elevation for: (a) co-polarization mismatch levels, and (b) cross-polarization level increment. . . . .	58
3.9	Normalized variations as function of the bias in gimbal azimuth, and for different probe array configurations of $1 \times 1$ , $2 \times 2$ , $3 \times 3$ , $4 \times 4$ , $8 \times 8$ , and $80 \times 80$ elements, for: (a) co-polarization mismatch levels, and (b) cross-polarization level increment. . . . .	59
4.1	H-polarization model of the probe antenna and UAV (first column), and radiation patterns in the E- (second column), H- (third column), and D-planes (fourth column) for: (a) dipole, (b) patch, (c) 4x4 array, and (d) horn antenna. Colored lines correspond to the radiation patterns of the probe antenna mounted on the UAV, while black lines correspond to the probe antenna in free space. . . . .	66
4.2	H-polarization surface currents induced in the UAV for: (a) dipole, (b) patch, (c) 4x4 patch array, and (d) horn antenna. . . . .	67
4.3	V-polarization radiation patterns in the E- (first column), H- (second column), and D-planes (third column), and surface currents on the UAV for: (a) dipole, (b) patch, (c) 4x4 patch array, and (d) horn antenna. Colored lines correspond to the radiation patterns of the probe antenna mounted on the UAV, while black lines correspond to the probe antenna in free space. . . . .	68
4.4	Performance of the simulated dipole in terms of: (a) co-polarization mismatch for free space (black) and mounted on the UAV (orange), (b) H- (red) and V-pol (blue) ripples in co-polarization pattern, (c) cross-polarization patterns of free space (black) and mounted on UAV (orange) for H- (dotted) and V-pol (dash-dotted), and (d) model of the UAV and dipole. . . . .	75
4.5	Performance of the simulated patch in terms of: (a) co-polarization mismatch for free space (black) and mounted on the UAV (orange), (b) H- (red) and V-pol (blue) ripples in co-polarization pattern, (c) cross-polarization patterns of free space (black) and mounted on UAV (orange) for H- (dotted) and V-pol (dash-dotted), and (d) model of the UAV and patch. . . . .	77
4.6	Performance of the simulated 4x4 patch array in terms of: (a) co-polarization mismatch for free space (black) and mounted on the UAV (orange), (b) H- (red) and V-pol (blue) ripples in co-polarization pattern, (c) cross-polarization patterns of free space (black) and mounted on UAV (orange) for H- (dotted) and V-pol (dash-dotted), and (d) model of the UAV and patch array. . . . .	79
4.7	Performance of the simulated horn in terms of: (a) co-polarization mismatch for free space (black) and mounted on the UAV (orange), (b) H- (red) and V-pol (blue) ripples in co-polarization pattern, (c) cross-polarization patterns of free space (black) and mounted on UAV (orange) for H- (dotted) and V-pol (dash-dotted), and (d) model of the UAV and horn. . . . .	81

4.8	Qualitative flight and RF performances for different antenna types. . .	83
4.9	Measurement setup in planar near-field anechoic chamber: UAV with landing gear in engaged position with probe antenna (4x4 patch array) mounted on gimbal. The measurements were performed in the NF (pictured above) and FF anechoic chamber facilities of the University of Oklahoma's (OU) Advanced Radar Research Center (ARRC). . .	85
4.10	Normalized measured antenna radiation patterns of the truncated 4x4 patch array antenna used as a probe in free space (black) and mounted on the UAV (blue/red) for: (a) H-pol, E-plane, (b) H-pol, H-plane, (c) V-pol, E-plane, and (d) V-pol, H-plane. . . . .	86
4.11	Performance of the measured array in terms of: (a) co-polarization mismatch for free space (black) and mounted on the UAV (orange), (b) H- (red) and V-pol (blue) ripples in co-polarization pattern, and (c) cross-polarization patterns of free space (black) and mounted on UAV (orange) for H- (dotted) and V-pol (dash-dotted). The gimbal orientation angles are $\alpha_r, \alpha_p, \alpha_y = 0^\circ$ relative to the UAV frame. . . .	87
4.12	Radiation characteristics of the probe antenna mounted on the UAV and gimbal: (a) radiation patterns in co- (solid) and cross-polarization (dashed), for H- (red) and V-pol (blue), for different gimbal yaw angles relative to the nose of the UAV, (b) mismatch at boresight ( $0^\circ$ for each pattern in (a)) between H- and V-pol, and (c) cross-polarization levels at boresight (same as (b)) for H- (red) and V-pol (blue). . . . .	89
5.1	Timeline of the changes in the platform in terms of hardware, flight, and RF performance. . . . .	94
5.2	The DJI Phantom 3 Professional platform. . . . .	95
5.3	The OU-UAVRF1250 platform with the custom made gimbal and the 3x3 FR4 array probe antenna. The frame is an octocopter, with the differential GPS mounted on top, and a retractable landing gear. . . .	97
5.4	The DJI S900 platform with the InfinityMR PRO v2 gimbal and the SS probe antenna. . . . .	99
5.5	The DJI Matrice 600 Pro platform with the Ronin-MX gimbal and the SS probe antenna, with triple GPS sensors for redundancy during flight, and dual RTK antennas for increased positioning accuracy. . .	101
5.6	Footprint of the UAV in ENU coordinate system for different ground locations with standard GPS data shown in blue tracks, and RTK data in red: (a) Zoomed out showing all the different positions. (b) Zoomed in on position 1 for clarity. (c) Zoomed in on position 2. (d) Zoomed in on for position 3. . . . .	105
5.7	UAV tracks in ENU coordinate system relative to home (takeoff) position during hover mode in RTK (blue), and GPS (red) operation. . .	106
5.8	Orientation performance measured in terms of RF variability through gimbal drift. . . . .	108
5.9	The Stop Sign (SS) antenna front and back (top), and the return losses in H and V (bottom). . . . .	109

5.10	Windfreak Technologies SynthHD signal generator mounted on the gimbal. . . . .	110
5.11	Twitchy circuit used for polarization switching between H and V. . .	111
5.12	Some of the instrumentation for the receiver subsystem: amplifier board, FieldFox N9917A, an AD9371 transceiver board, and the SS AUT. . . . .	112
5.13	Illustration of a hover mode method for UAV-based antenna measurement. The UAV hovers in a point in space while the AUT scans mechanically in azimuth and/or elevation. . . . .	115
5.14	Hover flight pattern extracted from the flight log. The UAV is hovering at a nominal altitude of 30 m AGL. . . . .	116
5.15	Illustration of a circular mode method for UAV-based antenna measurement. The AUT is stationary, while the UAV scans around the nominal AUT phase center. . . . .	118
5.16	Circular flight pattern extracted from the flight log. The radius of flight is 5 m. Higher density of samples corresponds to a slower flight speed, while the lower density corresponds to a faster flight speed. . .	118
5.17	Illustration of a vertical grid mode method for UAV-based antenna measurement: (a) grid lines are at a constant altitude, (b) grid lines are vertical. . . . .	120
5.18	Vertical grid flight pattern extracted from the flight log. The grid lines are nominally spaced 15 m apart in height. . . . .	121
5.19	Illustration of a rectilinear mode method for UAV-based antenna measurement. The UAV scans in rectilinear flights in two orthogonal directions to extract the radiation patterns of the principal planes. . . .	123
5.20	Illustration of a horizontal grid mode method for UAV-based antenna measurement. The UAV performs a horizontal scan above the AUT. This method is suitable for “bird bath” mode. . . . .	124
5.21	Illustration of a spherical mode method for UAV-based antenna measurement: (a) azimuth flights (conical cuts), (b) elevation flights (half great circle cuts). . . . .	125
5.22	Illustration of relevant flight strategies in bird-bath mode for UAV-based antenna measurements: (a) horizontal grid, (b) rectilinear. . . .	126
5.23	SS radiation patterns for H (top) and V (bottom) polarizations obtained from indoor chamber measurements (black) and outdoors (blue). Co-polarization patterns are shown in solid lines, while cross-polarization patterns are shown in dashed lines. . . . .	128
5.24	SS radiation patterns from UAV-based system in hover mode for H (top) and V (bottom) polarizations. Co-polarization patterns are shown in solid lines, while cross-polarization patterns are shown in dashed lines. 130	
5.25	SS radiation patterns from UAV-based system in circular mode for H (top) and V (bottom) polarizations. Co-polarization patterns are shown in solid lines, while cross-polarization patterns are shown in dashed lines. Multiple passes are shown overlapped. . . . .	132

5.26	A comparison of SS radiation patterns from different sources for H (top) and V (bottom) polarizations. Co-polarization patterns are shown in solid lines, while cross-polarization patterns are shown in dashed lines. Fixed reference is shown in black, UAV-based in hover mode is shown in red, and UAV-based in circular mode is shown in blue. . . . .	134
6.1	CPPAR system mounted on the rooftop of the Radar Innovations Laboratory (RIL), and the UAV-based system during a mission. . . . .	138
6.2	CPPAR radiation patterns measured with the FF tower (fixed reference) at 2.80 GHz for conical cuts at 3.3° elevation, a relative height of 13.7 m and range of 227 m. The co- and cross-polarization patterns for H (top) and V (bottom) polarizations are shown as a function of azimuth. Multiple consecutive scans are overlapped (colored) with the mean value (gray). . . . .	139
6.3	Positioning accuracy throughout the operation at ~13 m for H- (top two) and V-polarized (bottom two) probe under average wind speed of 25 mph and gusts at 38 mph. The plots show the range and the height of the UAV relative to the POI at a specific time. . . . .	141
6.4	Positioning accuracy throughout the operation at ~26 m for H- (top two) and V-polarized (bottom two) probe under average wind speed of 25 mph and gusts at 38 mph. The plots show the range and the height of the UAV relative to the POI at a specific time. . . . .	142
6.5	CPPAR radiation patterns measured with the UAV at 2.80 GHz for conical cuts at 3.3° elevation, a relative height of 13 m and range of 227 m. The co- and cross-polarization patterns for H (top) and V (bottom) polarizations are shown as a function of azimuth. Multiple consecutive scans are overlapped (colored) with the mean value (gray). . . . .	144
6.6	CPPAR radiation patterns measured with the UAV at 2.80 GHz for conical cuts at 6.5° elevation, a relative height of 26 m and range of 227 m. The co- and cross-polarization patterns for H (top) and V (bottom) polarizations are shown as a function of azimuth. Multiple consecutive scans are overlapped (colored) with the mean value (gray). . . . .	145
6.7	CPPAR radiation patterns measured with the FF tower (black) and the UAV (red) at 2.80 GHz for conical cuts at 3.3° elevation, a relative height of ~13 m and range of 227 m. The co- and cross-polarization patterns for H (top) and V (bottom) polarizations are shown as a function of azimuth. . . . .	146

# Chapter 1

## Introduction

### 1.1 Motivation

The US Multi-mission Phased Array Radar (MPAR) concept began with the goal to combine and replace the nation's air traffic control, air surveillance, and weather surveillance radar systems with a single radar type [3], [4]. The solutions proposed in the past have included a large number of small X-band arrays operating in a distributed manner [5], but the conventional thought is that such a system would take the form of a large S-band array [6] with distribution locations, coverage, and size characteristics similar to the current weather and air surveillance systems. In the recent decade, there have been efforts to migrate the current dish-based and mechanically steered weather radar system (WSR-88D and NEXRAD [7]) into fully digital dual-polarized phased array weather radar systems with electronic scanning capabilities. Dual polarization is required in order for a modern weather radar to best identify types of precipitation, estimate rainfall rates accurately, and determine the effects of propagation on these measurements. The principal drivers of the main requirements for these systems are: differential reflectivity ( $Z_{DR}$ ), correlation coefficient ( $\rho_{HV}$ ), and specific differential phase ( $K_{DP}$ ) [8]. Measurements of  $\rho_{HV}$  are corrupted by cross-polarization errors and radiation pattern mismatch, and degrade the ability

to distinguish between different types of hydrometeors and non-hydrometeor scatterers, while biases in  $Z_{DR}$  and  $K_{DP}$  can widely impact rainfall rate estimates [9]–[11] and are affected not only by mismatches between the horizontal (H) and vertical (V) antenna radiation patterns, but also by the existence of cross-polarization [12]. This imposes a strict requirement on the mismatch between the co-polarization patterns of no greater than 0.1 dB, and cross-polarization levels of no greater than about -45 dB, of the antenna for simultaneous transmit and simultaneous receive (STSR) operation mode [4]. The essential challenge in meeting these requirements is that phased arrays have inherent dependence of their radiation characteristics on scan angle while mechanically steered dish-based systems do not. Ultimately, each system in the network will require accurate characterization and calibration of its components to ensure that no errors are being introduced in the polarimetric weather radar products. Therefore, an in-situ antenna measurement method that complies with such demands is necessary to calibrate each radar in the network.

To accurately characterize antennas, specialized indoor or outdoor antenna range facilities are required for testing and evaluating the antenna's radiation characteristics. They consist of the appropriate RF instrumentation, technical procedures, and physical space required for the measurements. The design and construction of such facilities can introduce additional space and cost constraints upon the antenna installation site and, furthermore, an antenna characterized in an indoor facility will not necessarily perform identically in an outdoor environment under normal operating conditions [13]–[15]. In other words, the intrinsic radiation characteristics and the overall performance of an antenna may be substantially modified due to a number of factors of its working environment (e.g., temperature, humidity, weather conditions, ground clutter, RF interference, morphology, component failure rate, and others) [16]. An outdoor in-situ range can adequately measure the antenna system's performance

in its final installation site, to ensure that it meets the requirements, and that its interaction with the environment is predictable [13]–[15]. For example, elevated ranges are typically used to test physically large antennas where the antennas are mounted on elevated structures and/or terrains, and are generally designed to operate over a mostly flat area and to mitigate the effects of its surroundings by a number of design criteria, which include a careful selection of the probe antenna, its mounting structure and position, the terrain, and other structural elements to redirect or absorb reflected energy [13]–[15]. Unfortunately, it can easily become cost-prohibitive and impractical to develop such facilities for networks with a large number of non-mobile radars. To overcome this, a wide variety of methods and equipment for mobile in-situ antenna measurements have been employed in the past, which do not require large facilities around the antenna under test (AUT), including tethered balloons [17] and helicopters [18], [19]. These airborne methods [17]–[35] have been used in measuring the far-field (FF) radiation patterns of large antennas for a wide variety of applications and operating frequencies, offering improvements over cost constraints and allowing antenna test and evaluation solutions to be deployable for multiple sites. The measurements are performed using a probe antenna mounted on an airborne platform, which can range from manned aircraft [18], [19], up to small and micro unmanned aerial vehicles (UAV) [20]–[35]. In this context, a UAV-based antenna range could provide a cost-effective method for in-situ antenna characterization since it does not require extensive modification of the antenna test site and is generally portable from one site to the other. It is still unknown, however, how and to what extent environmental factors, flight strategies, and stability of the UAV may affect the measurements, especially in the case of polarimetric phased array weather radars which require a high degree of accuracy in the co- and cross-polarization antenna patterns. Furthermore, the probe antenna used for characterizing the antenna under test (AUT) must also adhere to the strict requirements imposed by the characterization and calibration requirements

of the weather radar system. Due to scattering and diffraction effects from the UAV structure (i.e., interaction of the probe antenna and UAV), the radiation characteristics of the probe antenna are degraded by the introduction of ripples in the pattern, which affects the co-polarization matching between the H and V polarizations, and the cross-polarization levels negatively. To adequately calibrate such systems, it is important that these effects are accurately characterized, and proper steps are taken to compensate or mitigate the impact on the probe antenna radiation characteristics.

While [36] explores the calibration of a weather radar using a UAV and a metallic sphere, as of the time of this writing, no other work relates to the radiation pattern-level characterization and calibration of polarimetric weather radars using UAVs.

## 1.2 Literature Review

One of the first works in in-situ antenna radiation pattern measurements was presented in the mid 60s. Steele [17] introduced this idea by using a tethered balloon with a dipole as the probe antenna for the measurement of a HF array, and successfully obtained partial elevation gain patterns with the balloon at different distances and directions while the AUT was rotating. The main disadvantage of tethered balloons is the inability to control its position accurately.

Overcoming this limitation, in the late 80s, [18], [19] introduced a helicopter-borne measurement method of antenna gain patterns capable of operating in HF up to S-band ranges. A wide-beam probe antenna is mounted under the aircraft, while it flies in different paths (for azimuth and elevation cuts), recording the field strength measurements transmitted by the AUT, and the position for post-processing, which allowed for accurate characterization of the antenna radiation pattern over real terrain. Although the use of manned aircraft can provide high precision measurements and allow for a large payload, it is definitely not cost-effective nor practical to implement.

The field of RF measurement and characterization using UAVs, ranging from micro and small to medium and large frames, has seen a fast-paced evolution in the past decade, in virtue of the increased availability of commercial off-the-shelf flight solution suites with high degree of precision and performance at lower costs. Generally, these systems are additionally equipped with the necessary instrumentation to record the position of the UAV accurately using on-board GPS and IMU, and some form of field strength measurement system (e.g., portable spectrum analyzer, power recorder), and a probe antenna, at the very minimum. Most of these research efforts have been focused in radio astronomy applications operating in VHF bands, although with the advent of 5G technologies, the demand for accurate antenna radiation pattern characterization has increased in microwave telecommunication systems as well, for diagnosing performance, coverage, and standards compliance.

As an example in radio astronomy, in 2015, [33] presented a hexacopter system where a telescopic dipole is mounted on, with the ability to perform measurements of large aperture arrays at frequencies from 50 MHz up to 650 MHz, showing good agreement between simulated and measured co-polarization antenna patterns for E- and H-plane cuts. Later in 2018, [37] presented more results in measuring and validating the 2D radiation pattern of a large ultra wide band array radio telescope; their results found discrepancies in the measured patterns, while highlighting the importance of calibration. In these systems, meeting the FF distance criterion becomes a challenge due to the large aperture sizes; additionally, the AUTs are usually measured in bird-bath mode (i.e., pointed towards zenith) such that there is less contamination from ground reflections. In the same context, [38] explored sampling the near-field (NF) radiation surrounding the AUT to overcome the FF distance limitations.

For telecommunication, [32], [39], [40] presented a compact, low-cost system for S and C bands, capable of centimeter-level accuracy, by sampling the NF radiation and

using a combination phaseless sources reconstruction method and NF-to-FF transformation to obtain the measured FF radiation patterns. Then, [41] further improves on these achievements by adding an extra probe and increased positioning accuracy with a dual-band RTK GNSS. A high degree of positioning precision becomes critical at higher operational frequencies, where the errors in position are in the order of a wavelength.

Most of the research efforts discussed thus far presented good results in the measurement of co-polarization radiation patterns at different frequencies, however, characterization of the cross-polarization pattern and polarimetric systems remains to be fully explored. In the weather radar field, where the latter are key components, a predecessor to this work [16] provided an overview and preliminary results of the efforts in UAV-based antenna measurements and  $Z_{DR}$  calibration for polarimetric weather radars. On the other hand, [36] presented a method of obtaining the antenna and radar constants by means of a metallic sphere and UAV. As far as UAV-based antenna characterization and calibration is concerned, these works have contributed substantially in advancing the state of the art, albeit there still remain unanswered questions that were discussed in the motivation. A list of all the work currently available in literature related to RF measurements with UAVs is summarized and compiled in the table below.

Application	Frequency Band	UAV Type	References
Radio Astronomy	HF, VHF, UHF	Hexacopter, Octocopter	[20]–[28], [30], [33], [37], [38], [42]–[54]
Telecommunications	S, C, K	Hexacopter	[32], [39]–[41], [55]–[58]
Defense	VHF, UHF, L	Tricopter, Octocopter, Airplane, Helicopter	[29], [59]–[61]
Space and Atmospheric	VHF, S, C, X	Quadcopter, Hexacopter, Octocopter	[16], [31], [34]–[36], [62]–[64]

Table 1.1: Summary of work related to UAV-based antenna measurements.

With respect to polarimetric phased array calibration, [65] provides an overview of the state of the art and past weather radar calibration efforts, as well as outlining measurement errors and metrics to quantify performance, with a detailed presentation of the polarimetric calibration method which will be used herein. Additionally, [4]

presents an update of the most current challenges and potential solutions within this framework.

### 1.3 Problem Statement

The use of phased array technology for the US weather radar network has been proposed [3] in lieu of the current mechanically steered dish-based systems owing to its many attractive features, e.g., electronic steering and fast update rates, and others. Scatterer identification (hydrometeors and non-hydrometeors), accurate estimation of rainfall rates, and determination of propagation effects is possible in weather radars through polarimetry [66]. The existence of cross-polarization, and co-polarization mismatch in the H- and V-polarization radiation patterns introduces biases in the polarimetric weather radar products, which can adversely affect the accuracy of the estimates of byproducts [12]; and imposes strict antenna requirements on the co-polarization mismatch of no greater than 0.1 dB, and cross-polarization levels of no greater than about -45 dB, in STSR operation mode [6]. Since the radiation characteristics of phased arrays are inherently dependent on the beam direction, it becomes even more challenging to meet these requirements. Furthermore, each system in this large network will require accurate characterization and calibration to ensure that the requirements are met. Clearly, the system and instrumentation used for the measurement and characterization also need to meet or exceed the system level requirements to provide reliable results.

Given that radar and other communications systems require in-situ calibration, it is hypothesized that a UAV-based antenna measurement system is able to replace conventional outdoor ranges in virtue of its low cost and flexibility of operation. The proposed solution is a UAV-based in-situ antenna characterization system with the necessary RF instrumentation to perform accurate measurements of a typical weather radar, along with general guidelines and procedures to ensure optimal results. The

solution attempts to provide a portable and cost-effective alternative to conventional outdoor antenna ranges that can be deployed in multiple sites with few adjustments. Additionally, the on-site measurement feature allows the assessment of the impact of extraneous environmental effects on the performance of the weather radar system under test. Lastly, the results of the UAV-based antenna characterization can be ingested into a calibration algorithm [4] to compensate for deviations from ideal operational conditions.

## 1.4 Research Scope

The preliminary stages of this research involves investigating the feasibility of using UAVs for S-band antenna characterization from a theoretical standpoint. Following [13], an assessment of the field conditions can be performed beforehand to derive the best measurement configuration in terms of height, range, flight mode, wind conditions, and extraneous reflections mitigation by accounting for error sources in FF antenna measurements. The MATLAB framework developed in this context provides the means for a quick evaluation of the impact of potential error sources before performing in-situ measurements, with the use of adequate models of the AUT, probe antenna, and environmental factors.

Next, an extensive study on the EM interaction of the probe antenna and the UAV structure is performed, with the objective of determining the best type of probe antenna to be used for this particular application. This is done through EM simulations in HFSS, and the probe performance is validated with anechoic chamber measurements. Additionally, practical strategies to mitigate the undesired effects are discussed and analyzed.

After the groundwork has been laid, the concept platform is introduced and discussed thoroughly. The evolution of the test platform and the road map leading to its different revisions and its current state is presented. Preliminary results of flight

tests and field experiments are provided as proof of concept, then the outdoor measurements are compared to indoor measurements for a specific AUT, and the validity of the results is studied. The final goal is to characterize and apply the calibration scheme on a real system, and to provide a qualitative and quantitative analysis of the outcome of the pre- and post-correction performance.

The last stage of the research attempts to provide the foundation for future work, with a discussion on the limitations, and additional strategies (e.g., signal processing, hardware upgrade, etc.) to further improve the current platform.

## 1.5 Contribution

The principal contribution of this work is a UAV-based antenna characterization system geared towards polarimetric weather radar calibration. Currently, no other work in UAV-based measurement systems relates to the characterization and calibration of polarimetric phased array weather radars. In addition, other individual contributions are:

- A formal compilation of guidelines and considerations for FF antenna measurements using UAV for polarimetric phased arrays.
- A MATLAB simulation framework for UAV-based FF antenna measurements that ingests models of AUT, probe antenna, and environmental factors (wind conditions, extraneous reflections), and produces simulated measurements which can be used for qualitative and quantitative analysis of potential error sources.
- An evaluation and validation of the EM interaction effects between UAV structure and different probe antenna types, which can be used to establish criteria for probe selection, and strategies for the mitigation of undesired reflections from the UAV structure.

- A cost-effective, controllable, mobile, in-situ antenna characterization system for the calibration of polarimetric weather radars, which can be easily deployed in multiple test sites.
- A set of guidelines which includes instrumentation, procedures, best practices, and limitations of the proposed system.

## 1.6 Dissertation Overview

This dissertation is divided into seven chapters, which aim to cover in full detail the different aspects that are involved in the UAV-based antenna characterization and polarimetric weather radar calibration system. Chapter 2 discusses some fundamental concepts helpful in understanding the basics of FF antenna measurements, phased array antennas, and polarimetric weather radars.

Chapter 3 presents a formal compilation of FF antenna measurement guidelines for UAV-based operations in terms of design, instrumentation, and procedure considerations. Additionally presented in this chapter is a MATLAB simulation framework developed for the assessment of potential error sources, as well as a qualitative and quantitative error analysis for select cases.

Chapter 4 explores to what extent the antenna radiation pattern for different types of antenna is affected by the structure of the UAV. EM simulations of the probe antenna in free space and mounted on the UAV are studied for different probe antennas, in an attempt to qualitatively describe the effects of the UAV on the radiation characteristics. The use of a gimbal as a means to control the orientation of the probe antenna is also analyzed herein.

Chapter 5 presents the concept platform by describing each of its components, and also discusses its evolution and road map. The results of flight tests and field

experiments are also summarized and presented here, with an comparative analysis between conventional methods and the proposed solution.

Recalling the basic principles related to polarimetric calibration, Chapter 6 presents and analyzes the results of measuring a real polarimetric radar systems.

Finally, Chapter 7 closes this work with an overall summary of the contributions, the concluding remarks, and lays down the foundation for future work.

## Chapter 2

### Fundamentals

The context of the problem presented in Chapter 1 requires a description of the concepts involved in antenna measurements, and in particular, when associated with polarimetric weather radar applications, and phased array systems. This chapter synthesizes the fundamental concepts required to properly understand the problem. In the subsequent sections, the fundamentals of antenna measurement, phased array antennas, and polarimetric weather radars will be briefly summarized.

#### 2.1 Antenna Measurements

The acceleration of electric charges produces electromagnetic (EM) waves. The electric field due to an unaccelerated charge decreases quadratically as a function of the distance from the charge and is directed radially, while the acceleration of the charge results in a tangential component of the electric field which decreases linearly with distance. Additionally, a time varying electric field is associated with a time varying magnetic field, which together produce an EM field which decreases linearly with distance and it represents an outward radiation. In practice, one is concerned with the macroscopic effects that the aggregate of charges produce due to acceleration. In

this macroscopic scale, Maxwell's equations [15] mathematically describe the inter-relationship between electric and magnetic fields, and the constitutive relationships specify the characteristics of the medium in which the field exists.

An antenna is a device that serves as a transition between a guided EM wave and an EM wave propagating in free space. Under a given set of conditions, the radiation characteristics of an antenna can be completely characterized by the its relative amplitude and relative phase in two orthogonal polarizations, and the power gain on the surface of a sphere centered at the AUT [13]. A representation of any of these properties as a function of spatial coordinates is defined as a radiation pattern or antenna pattern of the AUT. In addition to the main parameters, others might be required to accurately describe the radiation characteristics, which include the antenna efficiency, impedance at its input terminals, operating frequency, element phase, feed position, steady state temperature, differential temperature over the antenna, angular acceleration, pressure, wind distortion effects, and others [14]. Usually, safety factors are incorporated into the design to reduce the probability of significant variations in the radiation characteristics for which data cannot be obtained, since measuring the set of characteristics which completely describe an antenna would be impractical or, in some cases, impossible. Nevertheless, it is desirable to measure the performance of the AUT over some region of interest and frequency range to ensure that the requirements of the system are met in areas where performance is critical and cannot be adequately predicted by calculations. Certain basic terms and relations related to antenna measurements are reviewed next.

### **2.1.1 Coordinate Systems**

Antenna radiation pattern measurements involve determination of signal levels as functions of position or direction in space, and its coordinate system is defined with respect to a mechanical reference on the AUT, which is typically the phase center or

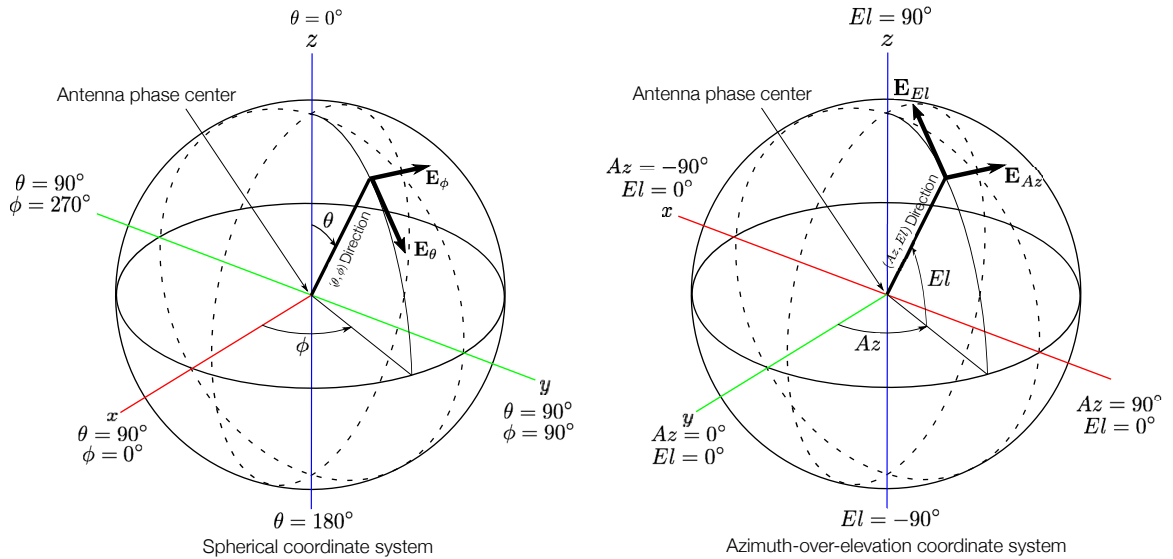


Figure 2.1: Typical coordinate systems used in antenna measurements and in weather radar.

the center of rotation of the antenna positioner. Because of the nature of radiation, the spherical coordinate system  $(R, \theta, \phi)$  is most often employed in antenna measurements (Figure 2.1, left), with the direction of propagation typically in the  $z$  direction, and the aperture of the antenna contained in the  $xy$  plane. Additionally, the most commonly used coordinate system in weather radars is the azimuth-over-elevation coordinate system (Figure 2.1, right), with the aperture of the radar contained in the  $xz$  plane, and with propagation in the  $y$  direction.

Since the line of sight  $R$  between the AUT and the probe antenna<sup>1</sup> is usually fixed, the radiation patterns are given instead as functions of two angular coordinates  $(\theta, \phi)$  by changing the orientation of the AUT to simulate movement of the line of sight over the spherical surface. Often, it is required to cover relatively large distances between the AUT and the probe antenna and it may be impractical or impossible to sample the antenna pattern over the entire sphere. Therefore, the directional sampling of the radiation pattern must be made with enough precision to adequately assess the performance of the AUT in the critical regions to ensure it meets the requirements of the operational system of which it is a part of.

<sup>1</sup>The AUT can be operating in either receiving or transmitting mode.

There is a variety of coordinate systems for antenna measurements and polarizations that can be more beneficial than the other depending on its application [67]. When discussing antenna pattern measurements in general, a  $\theta$ - $\phi$  reference is usually adopted, while for weather radars antenna patterns it is more common to employ a Az-El system.

### 2.1.2 Pattern Cuts

A direct method to measure the radiation pattern of an AUT is to employ a suitable scheme such that a relative movement between the AUT and the probe antenna along lines of constant  $\theta$  and  $\phi$  can be produced. The loci of constant  $\theta$  directions produce conical or  $\phi$  cuts, while constant  $\phi$  directions produce great circle or  $\theta$  cuts.

In practice, it is more common to measure principal plane cuts, which are  $\theta$  cuts through the AUT's boresight or axis of maximum gain. For a linearly polarized antenna, performance is often described in terms of the principal E-, and H-plane patterns, where the E-plane (H-plane) is defined as the plane containing the electric (magnetic) field vector and the direction of maximum radiation. For directive antennas, this is usually coincident with  $\phi = 0^\circ$  and  $90^\circ$  relative to the direction of polarization.

### 2.1.3 Field Regions

The space surrounding an antenna is divided into a reactive NF, radiating NF, and FF regions. The reactive NF region is defined as the portion of the NF region immediately surrounding the antenna wherein the reactive field predominates, and typically exists at a distance  $R < 0.62\sqrt{D^3/\lambda}$  from the surface of the AUT, where  $\lambda$  is the wavelength, and  $D$  is the aperture.

The radiating NF region is defined as the region where the radiation fields predominate and is between the reactive NF and the FF region, and where the angular field

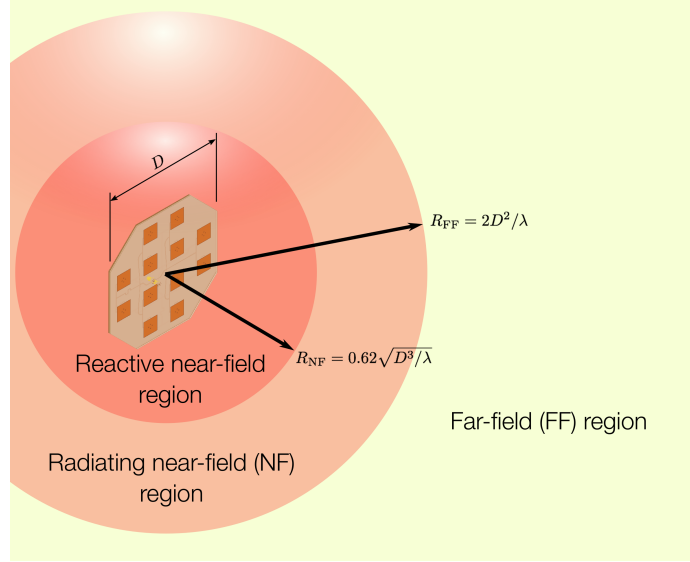


Figure 2.2: Radiating field regions of an antenna.

distribution depends on the distance from the AUT. If the antenna has an aperture that is comparable to the wavelength, this region may not exist.

The FF region is defined as the region of the field of an antenna where the angular field distribution is essentially independent of the distance from the antenna, with the field components essentially transverse, starting at a minimum FF distance of  $2D^2/\lambda$  from the antenna for a phase error of  $22.5^\circ$ , and with its outer bound at infinity. At any point in the far field of an antenna the radiated wave can be represented by a plane wave whose electric field intensity is the same as that of the wave and whose direction of propagation is in the radial direction from the antenna. As the radial distance approaches infinity, the radius of curvature of the radiated wave's phase front also approaches infinity and this in any specified direction the wave appears locally as a plane wave [15].

### 2.1.4 Polarization

The definition of the polarization of an antenna in a given direction is “the polarization of the wave transmitted by the antenna.” [15] Since the polarization varies with the

direction from the center of the antenna, different parts of the pattern may have different polarizations.

The polarization of a wave shall be defined depending on whether it is being transmitted or received by the antenna in a given direction. In FF, and in a specific direction and point in space, the polarization of a transmitted wave is defined as “the polarization of the (locally) plane wave which is used to represent the radiated wave at that point.” [15] Similarly, the polarization of a wave received by an antenna is defined as “the polarization of a plane wave incident from a given direction and power flux density, which results in maximum available power at the antenna’s terminals.” [15]

The polarization characteristics of an antenna can be represented as a spatial distribution of the polarizations transmitted by an antenna over its radiation sphere. To describe polarizations over the radiation sphere (or part of it), reference lines are specified over the sphere, to measure the direction of polarization for linear polarizations. A typical choice is a family of lines tangent to either the  $\theta$  or  $\phi$  directions (for a spherical coordinate system) at each point on the radiation sphere, then each point is resolved into a pair of orthogonal polarizations: the co-polarization and cross-polarization. Co-polarization represents the polarization the antenna is intended to transmit (receive), while the cross-polarization represents the polarization orthogonal to the co-polarization.

There is some ambiguity in the definition of cross-polarization in the weather radar community [68]. The Ludwig-3 definition is commonly used by antenna engineers, while for weather radars with azimuth-over-elevation coordinate systems, the Ludwig-2 definition of co- and cross-polarizations is more suitable. This is because the H/V polarization base matches the Ludwig-2 definition for co- and cross-polarizations, thus, the measurements in  $(Az, El)$  can directly correlate the polarimetric variables

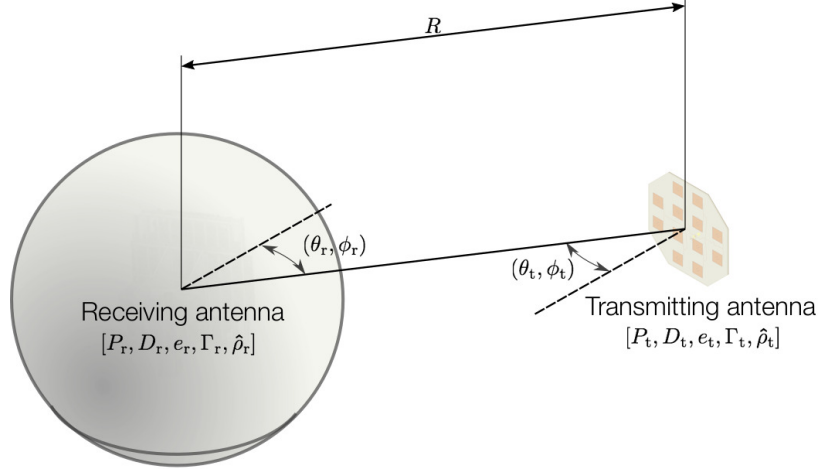


Figure 2.3: An illustration of the Friis transmission equation geometry.

to actual properties of weather scatterers (e.g., raindrop size, canting angle) appropriately.

### 2.1.5 Friis Transmission Equation

The Friis transmission equation [69] relates the power received to the power transmitted between antennas separated by a distance greater than the FF minimum of  $R > 2D^2/\lambda$ . A generalized form of the equation, in the form of the ratio between the received power to transmitted power, can be derived as [15]

$$\frac{P_r}{P_t} = e_t e_r (1 - |\Gamma_t|^2) (1 - |\Gamma_r|^2) \left( \frac{\lambda}{4\pi R} \right)^2 D_t(\theta_t, \phi_t) D_r(\theta_r, \phi_r) |\hat{\rho}_t \cdot \hat{\rho}_r|^2, \quad (2.1)$$

where  $e$  is the antenna's efficiency,  $\Gamma$  is the antenna's reflection coefficient,  $\lambda$  is the wavelength of operation of the antennas,  $R$  is the distance between the antennas,  $D(\theta, \phi)$  is the directivity in the  $(\theta, \phi)$  direction, and  $\hat{\rho}$  is the polarization vector, with the subscripts  $t, r$  indicating whether it is the transmitting or receiving antenna, respectively. Usually, the antenna and reflection efficiencies will be considered unity.

This equation relates the power  $P_r$  (delivered to the receiver load) to the input power of the transmitting antenna  $P_t$ . The term  $(\lambda/4\pi R)^2$  is called the free-space loss

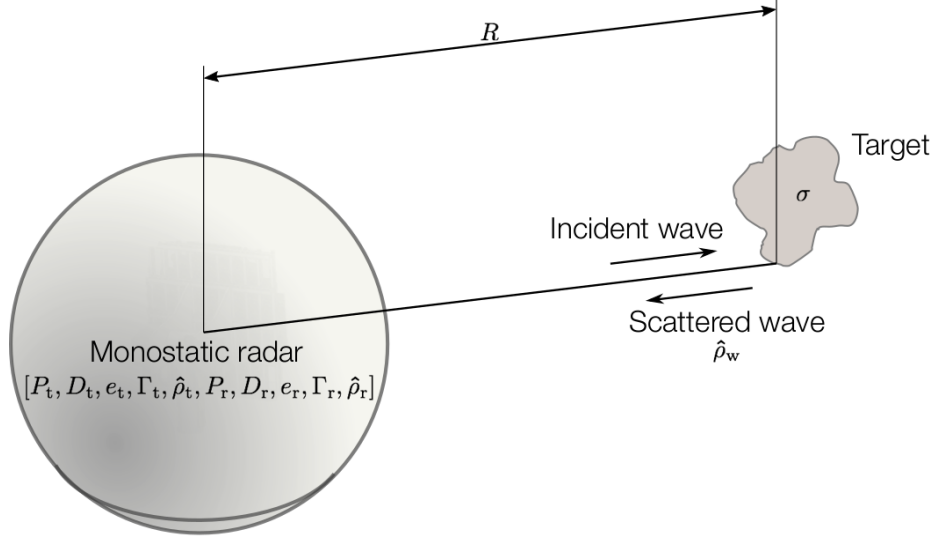


Figure 2.4: An illustration of the radar range equation geometry for a monostatic configuration.

factor or path loss, and it takes into account the losses due to the spherical spreading of the energy by the antenna. A detailed derivation of (2.1) can be found in [15].

### 2.1.6 Radar Range Equation

The radar cross section of a target is the area intercepting that amount of power which, when scattered isotropically, produces at the receiver a density which is equal to that scattered by the actual target. With this definition, it can be considered that the transmitted power incident upon the target is captured and reradiated isotropically as far as the receiver is concerned.

The expression known as the radar range equation relates the power  $P_r$  delivered to the receiver to the input power  $P_t$  transmitted by an antenna, after it has been scattered by a target with a radar cross section  $\sigma$ . The generalized form can be expressed as

$$\frac{P_r}{P_t} = e_t e_r (1 - |\Gamma_t|^2)(1 - |\Gamma_r|^2) \sigma \frac{D_t(\theta_t, \phi_t) D_r(\theta_r, \phi_r)}{4\pi} \left( \frac{\lambda}{4\pi R^2} \right)^2 |\hat{\rho}_w \cdot \hat{\rho}_r|^2, \quad (2.2)$$

for a monostatic radar. A detailed derivation of (2.2) can be found in [15].

## 2.2 Phased Array Antennas

The behavior of an array in a radar or communication system is far more complex than that of a mechanically steered antenna, because the performance characteristics vary with the scan angle. Array theory provides the tool to do most array synthesis and design without the need to derive exact electromagnetic models for each element [70].

### 2.2.1 The Array Pattern

The elements of an array can be generalized as a distribution of small radiating surfaces, each radiating a vector directional pattern with angular and radial dependence near the element (Figure 2.5). At distances very far from the element, this radiation has a  $e^{-jkR}/R$  dependence of a spherical wave multiplied by a vector function of angle  $f_i(\theta, \phi)$ , called the element pattern of the  $i$ th array element. For an arbitrary array, the pattern can be generally written by superposition as

$$\mathbf{E}(r, \theta, \phi) = \frac{e^{-jkR}}{R} \sum_i a_i f_i(\theta, \phi) e^{jk\mathbf{r}_i \cdot \hat{\mathbf{r}}}, \quad (2.3)$$

where  $k$  is the free space wave number,  $a_i$  is the excitation function of the element,  $f_i$  is the element pattern,  $\mathbf{r}_i$  is the position vector of the  $i$ th element relative to the center of the chosen coordinate system, and  $\hat{\mathbf{r}}$  is a unit vector in the direction of any point in space  $(R, \theta, \phi)$ . In antenna measurements, the array is typically contained in the  $xy$  plane with the  $z$  axis along the direction of propagation for the typical spherical coordinate system. However, in weather radars, the typical convention is to have the array contained in the  $xz$  plane with the direction of propagation in the  $y$  axis in an azimuth-over-elevation coordinate system. Nevertheless, Equation (2.3) uses generic position vectors in a Cartesian coordinate system, thus the array pattern will be matched to the orientation of the array accordingly.

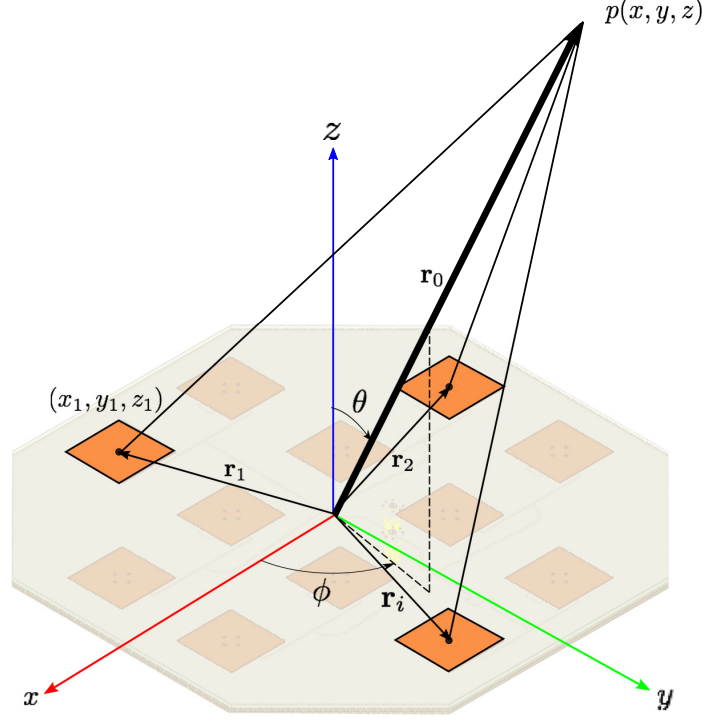


Figure 2.5: An illustration of the generalized array configuration.

Since the pattern is usually described or measured on a sphere of constant radius, the exponential factor outside of the sum can be disregarded, and if all element patterns are assumed to be identical, the array pattern can be thought of as the product of the element pattern and a scalar array factor  $AF(\theta, \phi)$ , where

$$AF(\theta, \phi) = \sum a_i e^{jk\mathbf{r}_i \cdot \hat{\mathbf{r}}}. \quad (2.4)$$

### 2.2.2 Array Scanning

Array scanning can be accomplished by applying the complex weights  $a_i$  in the form

$$a_i = |a_i| e^{-jk_0 \mathbf{r}_i \cdot \hat{\mathbf{r}}_0}, \quad (2.5)$$

where  $\hat{\mathbf{r}}_0 = u_0\hat{\mathbf{x}} + v_0\hat{\mathbf{y}} + \cos\theta_0\hat{\mathbf{z}}$  is the scanning direction, with  $u_0 = \sin\theta_0 \cos\phi_0$  and  $v_0 = \sin\theta_0 \sin\phi_0$ . These weights, which is more commonly controlled by phase shifters, steer the beam peak to an angular position  $(\theta_0, \phi_0)$ , for a frequency  $f_0$ .

The array factor for a planar array with elements in the  $xy$  plane at locations  $\mathbf{r}_{m,n} = md_x\hat{\mathbf{x}} + nd_y\hat{\mathbf{y}}$  and using phase steering to place the beam peak at  $\theta_0, \phi_0$  at frequency  $f_0$  is given by:

$$\text{AF}(\theta, \phi) = \sum_{m,n} |a_{m,n}| e^{jk_0[md_x(u-u_0)+nd_y(v-v_0)]}. \quad (2.6)$$

### 2.2.3 Beamwidth and Directivity

The beamwidth and sidelobe level (SLL) of an array antenna are dictated by the chosen aperture taper. Antenna sidelobes are reduced by tapering the array excitation so that elements at the array center are excited more strongly than those near the edge. In general, the half-power beamwidth of the radiation pattern in a linear array or in the principal planes of a rectangular array at broadside is

$$\theta_3 = 0.886B_b\lambda/D, \quad (2.7)$$

where  $B_b$  is the beam broadening factor, and  $D$  is the aperture of the array, i.e.,  $D = Md_x$ .

The directivity and beamwidths of a relatively large planar array are related by:

$$D_0 = 32400 \cos\theta_0/(\theta_{3x}\theta_{3y}), \quad (2.8)$$

where  $\theta_{3x}$  and  $\theta_{3y}$  are the 3-dB beamwidths of the pencil or elliptical beam at broadside, in degrees.

## 2.3 Polarimetric Weather Radar

As the radar emits a pulse of electromagnetic waves, energy is radiated to the scatterers along the path which reflect a portion of this energy back to the radar. A weather signal is composed of echoes from a large number of meteorological and non-meteorological scatterers in a small volume of the atmosphere [71]. Since the individual returns cannot be resolved, the weather signal is sampled at discrete range-time delays which define the approximate range of a resolution volume in space where the scatterers have the largest contribution to the weather signal sample. The resolution volume is determined by an angular weighting function related to the antenna's radiation pattern, and a range weighting function related to the radar filter's amplitude transfer function and the transmitted pulse envelope. The I/Q signal at the terminals of the receiver, for a given range resolution volume and for an observation dwell of  $M$  consecutive radar pulses as  $m = 0, \dots, M - 1$ , can be defined as the composite sum of the returns of each scatterer as:

$$V(m) = I(m) + jQ(m), \quad (2.9)$$

$$I(m) = \sum_{i=0}^{N-1} |A_i| \cos \gamma_i, \quad (2.10)$$

$$Q(m) = - \sum_{i=0}^{N-1} |A_i| \sin \gamma_i, \quad (2.11)$$

with the relationship of amplitude  $A_i$ , and phase  $\gamma_i$  of the  $i$ th scatterer with the radar parameters given by:

$$A_i = \sqrt{\frac{P_t \sigma G_t G_r f_t(\theta, \phi) f_r(\theta, \phi)}{(4\pi)^3}} \frac{\lambda}{R_i^2} w_r, \quad (2.12)$$

and

$$\gamma_i = \frac{4\pi R_i}{\lambda} + \frac{4\pi v_i T_s}{\lambda} - \psi_{si}, \quad (2.13)$$

where  $P_t$  is the peak transmitted power,  $\sigma_b$  is the backscattering cross section of the scatterer,  $G_{t,r}$  is the antenna gain on transmit or receive,  $f_{t,r}(\theta, \phi)$  is the antenna radiation pattern on transmit or receive,  $\lambda$  is the radar's operating wavelength,  $R_i$  is the range to the scatterer,  $w_r$  is the radar's range-weighting function,  $v_i$  is the radial velocity of the scatterer,  $T_s$  is the pulse repetition time,  $\psi_{si}$  is the phase shift imposed by the  $i$ th scatterer, and  $N$  is the total number of scatterers.

### 2.3.1 Polarimetric Radar Variables

A complete derivation of the weather radar and polarimetric weather radar variables can be found in [71] and [72]. Here, only a brief summary of the polarimetric weather radar variables will be presented.

Radar variables that are typically estimated from single polarization I/Q signals are: reflectivity factor ( $Z$ ), mean radial velocity ( $\bar{v}_r$ ), and spectrum width ( $\sigma_v$ ). Additional information about the scatterers in a radar resolution volume can be obtained with the transmission and reception of H- and V-polarized waves. These polarimetric radar variables are differential reflectivity ( $Z_{DR}$ ), cross-correlation coefficient ( $\rho_{HV}$ ), and differential phase ( $\phi_{DP}$ ). The polarimetric I/Q signals shall be denoted with the subscript H or V, depending on whether it corresponds to the horizontal or vertical polarization, respectively, and can be represented as

$$V_{H,V}(m) = I_{H,V}(m) + jQ_{H,V}(m). \quad (2.14)$$

Figure 2.6 shows a typical set of polarimetric weather radar products in a plan position indicator (PPI). An estimate of the average returned power can be obtained as

$$\hat{P}_{H,V} = \frac{1}{M} \sum_{m=0}^{M-1} V_{H,V}^*(m)V_{H,V}(m). \quad (2.15)$$

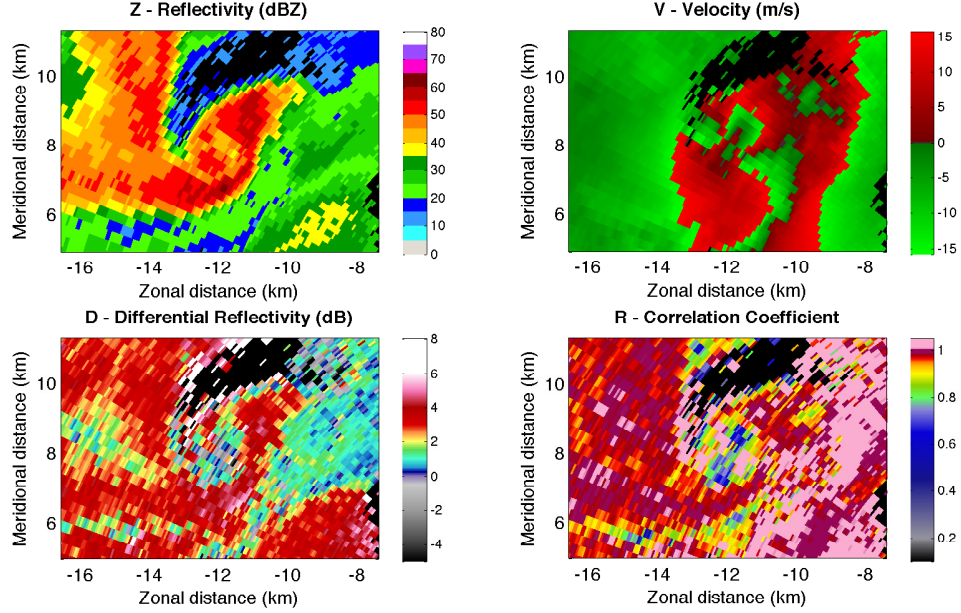


Figure 2.6: An example of a polarimetric weather radar PPI scan depicting the radar products:  $Z_H$  (top-left),  $\bar{v}_r$  (top-right),  $Z_{DR}$  (bottom-left), and  $\rho_{HV}$  (bottom-right). Extracted from [73] with permission.

By subtracting the noise power  $N$ , an estimate of the signal power can be obtained as

$$\hat{S}_{H,V} = \hat{P}_{H,V} - N_{H,V}. \quad (2.16)$$

The differential reflectivity  $Z_{DR}$  is the ratio of the power between the H- and V-polarizations, and it provides insight about the shape of the scatterers. It can be estimated as

$$\hat{Z}_{DR} = 10 \log \left( \frac{\hat{S}_H}{\hat{S}_V} \right). \quad (2.17)$$

Small raindrops typically have a spherical shape and a  $Z_{DR}$  of zero (in dB) due to the power returns in both channels being equal. Larger raindrops tend to become more oblate in shape, corresponding to the horizontal backscattered power being larger than the backscattered power in the vertical polarization, and result in a positive  $Z_{DR}$ . Other hydrometeors, such as ice crystals, can have a prolate shape, producing the opposite effect and thus having a negative  $Z_{DR}$  [72].

The correlation coefficient  $\rho_{\text{HV}}$  is a measure of how similar the H-polarization return is, in average, to the V-polarization return; it is a measure of the homogeneity of the returns from scatterers in the radar volume. To estimate the correlation coefficient, the cross-correlation function  $P_{\text{X}}$  between the H- and V-polarizations must be calculated, which can be obtained from (2.15) by exchanging the conjugate term with the opposite polarization (i.e.,  $V_{\text{H}}^*V_{\text{V}}$ ), then

$$\hat{\rho}_{\text{HV}} = \frac{|P_{\text{X}}|}{\sqrt{\hat{S}_{\text{H}}\hat{S}_{\text{V}}}}. \quad (2.18)$$

The returns in the H- and V-channels for any set of homogeneous scatterers will have a high  $\rho_{\text{HV}}$  (e.g., only raindrops). When the returns are a composite of different types of scatterers, the scattering can become less homogeneous, resulting in a lower  $\rho_{\text{HV}}$ .

The differential phase  $\phi_{\text{DP}}$  is defined as the backscattered differential phase between the returns from the scatterers in the resolution volume of the H- and V-polarizations and propagation differential phase (from the path the pulse travelled). It can be estimated using the cross-correlation function between the H- and V-polarizations as

$$\hat{\phi}_{\text{DP}} = \arg \left( \frac{P_{\text{X}}}{\sqrt{\hat{S}_{\text{H}}\hat{S}_{\text{V}}}} \right). \quad (2.19)$$

The differential phase is a measure of the resistance experienced by the electromagnetic waves as they travel through the atmosphere [74]. For example, waves traveling through a spherical scatterer would experience the same amount of resistance in both polarization channels ( $\phi_{\text{DP}} = 0^\circ$ ), while non-spherical scatterers would experience a positive difference if they are oblate ( $\phi_{\text{DP}} > 0^\circ$ ) and a negative difference if they are prolate ( $\phi_{\text{DP}} < 0^\circ$ ). It also provides an insight about the concentration of the scatterers, as higher concentrations will result in higher resistance in the wave propagation.

### 2.3.2 Polarimetric System Requirements

As previously mentioned, it is extremely challenging to obtain highly accurate polarimetric radar measurements with phased array technology [6]. The main culprit being the increasingly broader beams off broadside, which in turn degrades the cross-polarization characteristics significantly. This degrades the estimates of  $Z_{DR}$ ,  $\rho_{HV}$  and  $\phi_{DP}$ , and the ability discriminate between different types of hydrometeors and other scatterers, and also impacts rainfall rate estimation. Due to this, achieving a high level of accuracy in polarimetric measurements become very challenging, which include a  $Z_{DR}$  bias of 0.1 dB, a  $\rho_{HV}$  bias of 0.001, and a  $\phi_{DP}$  of  $3^\circ$ . In addition to these, other system level and polarimetric requirements are listed in Table 2.1. In terms of polarization purity, the H- and V-polarization antenna patterns must be precisely matched, and the cross polarization levels must be lower than -25 dB for ATSR (alternate transmission simultaneous reception), and -45 dB for STSR (simultaneous transmission simultaneous reception), that have been achieved with dish-based systems.

Antenna Metric	Specification	Remarks
Azimuth beamwidth	$1^\circ$	Large aperture, large FF distance
Elevation beamwidth	$1^\circ$	
Azimuth scan range	$\pm 45^\circ$	Adequate intrinsic polarization up to $20^\circ$ in elevation
Elevation scan range	-1 to $20^\circ$ (weather), to $60^\circ$ (other)	
Scan resolution	$0.5^\circ$	
Close-in SLL (2-way)	<-54 dB	Achieved with traditional phased array calibration techniques
Mid-range SLL (2-way)	Mask to -100 dB @ $\pm 10^\circ$	
Far-out SLL (2-way)	<-100 dB	
Bias in $Z_{DR}$ estimate	<0.1 dB @ $Z_{DR} = 0$ dB	Main driver of polarimetric requirements
Bias in $\rho_{HV}$ estimate	<0.001	Drives pattern shape requirements
Error in $\phi_{DP}$ estimate ( $\sigma$ )	< $3^\circ$	
H/V beam peak matching	<0.03 dB	Worst case scenario
H/V pattern shape matching	<0.5 dB @ -20 dB	For H/V correlation
Cross-polarization isolation (ATSR)	<-25 dB	At boresight, post correction
Cross-polarization isolation (STSR)	<-45 dB	

Table 2.1: Summary of polarimetric requirements. Adapted from [4].

It is imperative that the measurement system meets or exceeds the requirements to characterize such systems accurately. As was presented in previous chapters, both theoretically and practically, these measurement requirements can be met with the current UAV-based system. Further discussion will be made on how to implement a calibration strategy using the UAV-based measurements.

### 2.3.3 Basic Signal Model

A dual-polarized antenna has two ports, one for the H polarization and another one for the V polarization. The excitation in one port will produce radiation mainly in the corresponding polarization, but additional cross-contamination may occur in the orthogonal polarization. Let the array radiation pattern be denoted as  $F_{XY}(\theta, \phi, \theta_0, \phi_0)^2$ , with the subscript X indicating the polarization on reception, and Y indicating the polarization on transmission, as a function of the azimuth and elevation angles, and the corresponding scan angle given by  $\theta_0$  and  $\phi_0$ . In this sense, the co-polarization radiation patterns are  $F_{HH}$ ,  $F_{VV}$ , and their respective cross-polarization patterns are  $F_{HV}$ ,  $F_{VH}$ . With the use of the radar range equation and basic polarimetric scattering theory [72], it is possible a model for the relationship between the transmitted and the received signals from a single scatterer as

$$\begin{bmatrix} V_H \\ V_V \end{bmatrix} = E(r) \begin{bmatrix} F_{HH}(\theta, \phi, \theta_0, \phi_0) & F_{VH}(\theta, \phi, \theta_0, \phi_0) \\ F_{HV}(\theta, \phi, \theta_0, \phi_0) & F_{VV}(\theta, \phi, \theta_0, \phi_0) \end{bmatrix}_{\mathbf{R}} \begin{bmatrix} s_{HH} & s_{HV} \\ s_{VH} & s_{VV} \end{bmatrix} \begin{bmatrix} F_{HH}(\theta, \phi, \theta_0, \phi_0) & F_{HV}(\theta, \phi, \theta_0, \phi_0) \\ F_{VH}(\theta, \phi, \theta_0, \phi_0) & F_{VV}(\theta, \phi, \theta_0, \phi_0) \end{bmatrix}_{\mathbf{T}} \begin{bmatrix} A_H \\ A_V \end{bmatrix}, \quad (2.20)$$

or, in vector form

$$\mathbf{V} = E(r)[\mathbf{R}(\theta, \phi, \theta_0, \phi_0)]^T \mathbf{S} \mathbf{T}(\theta, \phi, \theta_0, \phi_0) \mathbf{A}, \quad (2.21)$$

---

<sup>2</sup>The uppercase notation is used for array patterns, and lowercase for element patterns.

where  $\mathbf{V} = [V_H \ V_V]^T$  is the vector of the received signal in the H and V ports,  $E(r)$  is an overall propagation term,  $\mathbf{F}_R = \mathbf{R}$  is the matrix of the antenna patterns on receive,  $\mathbf{F}_T = \mathbf{T}$  is the matrix of the antenna patterns on transmit,  $\mathbf{S}$  is the target's effective scattering matrix, and  $\mathbf{A} = [A_H \ A_V]^T$  is a vector of complex H and V pulse weights on transmission.

### 2.3.4 Basic Calibration Process

The radar operates by sending multiple pulses  $\mathbf{A}(m)$  ( $m = 0, \dots, M - 1$ ) and by processing the received signal  $\mathbf{V}(m)$ . The form of  $\mathbf{A}(m)$  will depend on the transmission mode: for STSR,  $A_H = 1$ ,  $A_V = A$  ( $\sim 1$ ), while for ATSR,  $A_H$  and  $A_V$  alternate between 1 and 0 between pulses. At boresight,  $\mathbf{R}$  and  $\mathbf{T}$  should ideally be proportional to the identity matrix. However, this is not generally the case due to polarization errors [4] and some form of correction is required.

The correction matrix method [8], [65], [75] is a simple method to mitigate cross-polarization biases. If the value of the antenna array patterns at the scan angle pair  $\theta_0, \phi_0$  are known, a pair of correction matrices can be calculated as

$$\mathbf{C}_R = \mathbf{R}^{-T}(\theta_0, \phi_0, \theta_0, \phi_0) = \begin{bmatrix} F_{HH}(\theta_0, \phi_0, \theta_0, \phi_0) & F_{VH}(\theta_0, \phi_0, \theta_0, \phi_0) \\ F_{HV}(\theta_0, \phi_0, \theta_0, \phi_0) & F_{VV}(\theta_0, \phi_0, \theta_0, \phi_0) \end{bmatrix}_R^{-1}, \quad (2.22)$$

$$\mathbf{C}_T = \mathbf{T}^{-1}(\theta_0, \phi_0, \theta_0, \phi_0) = \begin{bmatrix} F_{HH}(\theta_0, \phi_0, \theta_0, \phi_0) & F_{HV}(\theta_0, \phi_0, \theta_0, \phi_0) \\ F_{VH}(\theta_0, \phi_0, \theta_0, \phi_0) & F_{VV}(\theta_0, \phi_0, \theta_0, \phi_0) \end{bmatrix}_T^{-1}, \quad (2.23)$$

where  $\mathbf{C}_R$  is the correction matrix for receive errors, and  $\mathbf{C}_T$  is the correction matrix for transmit errors. When the correction is applied, these matrices effectively make

the products  $\mathbf{C}_R \mathbf{R}^T$  and  $\mathbf{T} \mathbf{C}_T$  proportional to the identity matrix at the scan center and cancel all cross-polarization effects, as

$$\begin{aligned} \mathbf{V} &= \mathbf{C}_R \mathbf{R}^T \mathbf{S} \mathbf{T} \mathbf{C}_T \mathbf{A} \\ &= \mathbf{R}^{-T} \mathbf{R}^T \mathbf{S} \mathbf{T} \mathbf{T}^{-1} \mathbf{A} \end{aligned} \tag{2.24}$$

$$\mathbf{V} = \mathbf{S} \mathbf{A} \tag{2.25}$$

A more detailed discussion on other polarimetric calibration methods have been presented in [4], [76]

## 2.4 Summary

Performing antenna measurements is, in itself, a very complex problem that spans very broad (and slightly different) aspects such as NF, FF, and radome measurements. As far as polarimetric weather radar systems go, the most relevant radiation characteristics are established in FF, and as such, the focus of the rest of the work is directed towards FF measurements. Additionally, with the proposal of replacing the current dish-based systems with phased array systems, it is convenient and necessary to include certain key aspects of these systems that relate directly to antenna measurements. Finally, a very brief summary of the polarimetric weather radar principle of operation and calibration has been presented to establish the link between antenna measurements and polarimetric radar products. Establishing these fundamental concepts should provide a better understanding of the aspects involving antenna measurements for polarimetric (phased array) weather radar systems, and will be useful for the subsequent chapters.

## Chapter 3

### Guidelines, Simulation and Error Analysis

It is understood that the intrinsic radiation characteristics and the overall performance of an antenna may not behave identically outdoors due to a number of factors of its working environment. Typically, specialized indoor or outdoor antenna range facilities are required to accurately characterize the radiation characteristics of antennas in FF, and the appropriate RF instrumentation, technical procedures, and physical space required for the measurements have been established in [13]. Moreover, design and implementation of such antenna measurement ranges may incur in prohibitive costs and spatial constraints surrounding the installation site. Because of the strict main polarimetric requirements discussed in Chapter 1, an in-situ antenna measurement method that complies with such demand will be necessary for accurate calibration of each radar in the large network to be possible. In this context, a UAV-based antenna range could provide a cost-effective method for in-situ antenna characterization since it does not require extensive modification of the antenna test site and is generally portable from one site to the other. However, the extent to which the environmental factors, flight strategies, and stability of the UAV may affect the measurements, especially in the case of polarimetric phased array weather radars (which typically operate in S band) which require a high degree of accuracy in the co- and cross-polarization antenna patterns remain unexplored. In this sense, performing a preliminary assessment of the field conditions can be useful in assessing the best

measurement configuration in terms of height, range, flight mode, wind conditions, and extraneous reflections mitigation by accounting for error sources in FF antenna measurements.

This chapter provides the guidelines for FF measurements using a UAV-based antenna measurement system, and a mathematical framework to adequately assess such potential effects prior to performing field tests. A summary of the guidelines for FF measurements applied to UAV-based antenna measurements in terms of design, instrumentation, and procedure considerations are presented first. The simulation framework for the UAV-based measurement method presented herein, and its error modeling, are then described, and the analysis and results for a particular set of case studies is assessed. Finally, a brief discussion and summary of this chapter is presented.

### **3.1 FF Guidelines for UAV-based Measurements**

With recent advances in commercially-off-the-shelf available technology for UAVs, it has become far more cost-effective to develop improved UAV-based antenna measurement solutions [20]–[35]. The main advantage UAVs provide is that they are not restricted in movement, and with the use of a gimbal, it is possible to have an airborne measurement system with multiple degrees of freedom. However, it becomes critical to suppress reflections and signals from undesired sources, and to compensate for misalignment between the probe antenna and the AUT, since these factors rely on the position and orientation of the UAV and gimbal. Naturally, this adds uncertainties in the measurements because the platform is generally subject to unfavorable environmental conditions. The measurements also depend on the precision of the on-board instrumentation, as well as the flight/scan procedure selected. Recent works [38], [41], [48], [49], [59], [60] have investigated the measurement of both magnitude and phase in near field (NF) to obtain the FF antenna pattern through NF-to-FF transformation for large aperture antennas using UAVs. However, this work is limited

to testing the FF amplitude of the of the co-, and cross-polarization antenna radiation pattern. This section focuses on the most relevant antenna range design criteria, instrumentation, and procedures applicable to UAV-based FF pattern measurements for polarimetric weather radar antennas.

### 3.1.1 Design Considerations

Much like in conventional outdoor FF antenna ranges, in UAV-based antenna measurements, the standard criteria [13], [14] must be adhered to, to ensure the measurement errors are minimal. From them, a set of criteria may be derived for UAV-based FF measurements by taking into account the mobility of the platform, and by not imposing any restriction on the type of probe antenna that can be used. Some of the effects that are considered herein for the design requirements are presented next.

#### 3.1.1.1 Effect of Phase Curvature

While the illuminating field is assumed to be a uniform plane wave for FF purposes, in reality, the phase variation is closer to that of a spherical wave emanating from the phase center of the probe antenna (see Figure 3.1).

A variation in the phase of the illuminating field will occur if the receiving antenna subtends less than a half-power beamwidth of the transmitting antenna's wave front. This phase error will produce an error in the measured amplitude at boresight, and a significant effect on the side-lobe level (SLL) and shape of the antenna radiation pattern [14]. An expression for the FF distance can be derived as

$$R \geq \frac{KD^2}{\lambda}, \quad (3.1)$$

where  $D$  is the aperture of the receiving antenna (or AUT),  $\lambda$  is the operating wavelength, and  $K$  is a constant related to the phase error. For example, for  $K = 2$ , which is typically accepted as the minimum FF distance, the error in measurement

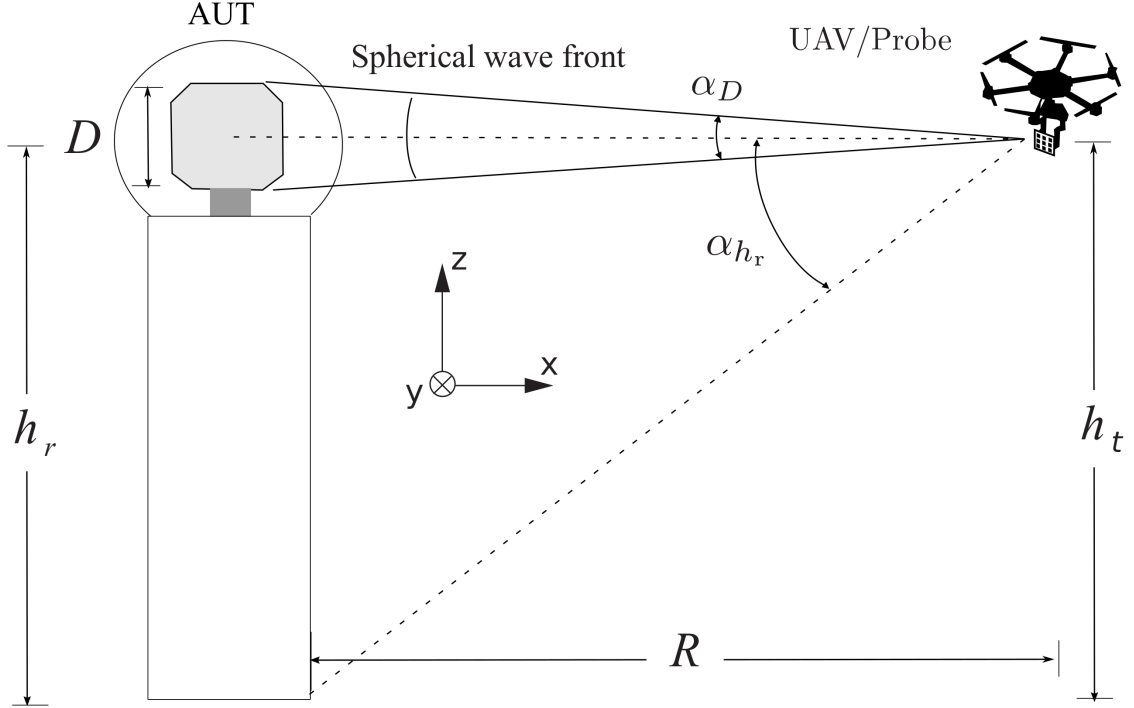


Figure 3.1: FF measurement configuration for the UAV, probe antenna, and AUT. The sketch depicts a spherical wave front leaving the probe antenna and impinging on the aperture of the AUT.

is approximately 0.1 dB [77]. For UAV-based measurements, this requirement can be easily met in virtue of the mobility of the UAV platform.

### 3.1.1.2 Effect of Transverse Amplitude Taper

A taper in the amplitude of the excitation function across the aperture of the AUT can produce errors in the measured radiation pattern, manifested as a reduction of the directivity, and variations in the SLL; i.e., this effect is closely related to the beamwidth of the probe antenna [13]. For UAV-based measurements with an arbitrary probe antenna, this amplitude taper criterion may be derived as

$$\theta_{\Delta} \geq \alpha_D, \quad (3.2)$$

where  $\theta_\Delta$  is the beamwidth of the probe antenna at the desired level  $\Delta$  of maximum amplitude taper, and  $\alpha_D$  is the angle subtended at the probe antenna by the AUT aperture width  $D$  (Figure 3.1), which is geometrically defined as

$$\alpha_D = 2 \tan^{-1} \left( \frac{D}{2R} \right). \quad (3.3)$$

Equations (3.2) and (3.3) establish a relationship between the probe antenna beamwidth, the AUT aperture width, and the range at which the measurement is being performed. As a rule of thumb, an amplitude taper of 0.25 dB at the edges of the aperture (i.e., a 0.25-dB beamwidth, or  $\theta_{0.25}$ ), yields errors in directivity no larger than 0.1 dB [14].

### 3.1.1.3 Effect of Ground Reflections

A basic design goal is to have the range surface in front of the AUT not intercept any energy contained in the main lobe of the antenna probe [13]. To achieve this in UAV-based measurements, the first null in the probe antenna radiation pattern should be directed toward the base of the AUT tower (Figure 3.1). This is equivalent to establishing that the plane angle subtended at the probe antenna by the AUT height and its phase center be equal to half of the first null beamwidth (FNBW) of the probe antenna (assuming a symmetrical radiation pattern), that is:

$$\frac{\text{FNBW}}{2} \leq \alpha_{h_r}, \quad (3.4)$$

$$\alpha_{h_r} = \tan^{-1} \left( \frac{h_r}{R} \right), \quad (3.5)$$

where  $h_r$  is the height of the AUT. Strategies to mitigate the effect of the reflections from the range surface (e.g., diffraction fences, longitudinal ramps) are not included in this work, since they require modifications of the test site and incur in additional costs.

### 3.1.1.4 Summary of Criteria

Table 3.1 summarizes the most important aspects to consider in the design and mitigation of errors for UAV-based measurements. Ideally, all three criteria should be met simultaneously, meaning that there will be restrictions on  $R$  for the UAV platform, and  $\theta_\Delta$  and FNBW for the probe antenna, depending on the tolerable measurement error levels  $\Delta$ , and the aperture  $D$  and height  $h_r$  of the AUT. It should be noted that these criteria for UAV-based measurements are only intended to be used as a guideline for selecting a suitable geographical location and probe antenna, and that they may not be simultaneously met at all times depending on the flight or scanning strategies. In such cases, a careful assessment would provide better insight of the error bounds.

Table 3.1: Summary of design considerations for UAV-base antenna measurements.

Parameter	Generalized criterion
Phase curvature	$R \geq \frac{KD^2}{\lambda}$
Transversal taper	$\theta_\Delta \geq \alpha_D$
Ground reflections	$\frac{\text{FNBW}}{2} \leq \alpha_{h_r}$

### 3.1.2 RF Instrumentation

The extent of the required instrumentation depends upon the functional requirements imposed by the measurements to be made. An antenna range is typically classified into five subsystems [15]: transmitting subsystem (including probe antenna), receiving subsystem, positioning subsystem, recording subsystem, and data-processing subsystem. Such a classification will be adopted here since, in general, one or more of these subsystems may be present in the ground hardware, the flight hardware, or both. Additionally, because the mechanical airborne and ground instrumentation may vary widely in performance and noting that the accuracy and precision requirements would

depend on the application, it is out of the scope of this work to present a discussion on each specific hardware. However, the basic RF instrumentation that allows FF magnitude measurements for co- and cross-polarization antenna patterns, for polarimetric weather radars, is discussed herein.

### 3.1.2.1 Transmitting and Receiving Subsystems

The UAV can be operating as the transmitter or receiver as long as the required equipment is installed. In either case, the payload and size constraints are the main limitations of the UAV that one must account for. The transmitting subsystem includes the probe antenna, signal source, and the signal source control, and it must be selected so that it has frequency control, frequency stability, spectral purity, required power level, and modulation. For antenna amplitude measurements, it is important that the output of the signal source remain relatively constant [13]. The receiving system will include an oscilloscope or spectrum analyzer, and the corresponding back end chain of components needed to capture the transmitted signals at an adequate sensitivity, frequency, bandwidth, and dynamic range<sup>1</sup>.

The antenna to be mounted on the UAV must be selected such that the gain, beamwidth, band of operation, and polarization is appropriate for the specific measurement requirement and the general design considerations listed in Table 3.1. As far as the power level is concerned, the required power output of the signal source for a particular measurement is dependent upon the probe antenna and AUT gains, the receiver sensitivity, the transmission loss between the two antennas, and the dynamic range required for the measurement. Regardless of whether it is operating as a transmitter or receiver, the endurance of the UAV should be such that it permits the safe operation of the aircraft and on-board equipment for as long as the measurement procedure lasts. An additional factor to consider is the operation of such

---

<sup>1</sup>A dynamic range of at least 60 dB would be necessary to accurately measure the cross-polarization pattern in weather radar systems.

instruments under different environmental conditions; as such, it is a good practice to have weather-resistant equipment or to weather-proof the UAV frame.

### **3.1.2.2 Positioning, Recording, and Data-processing Subsystems**

The positioning subsystem will consist of the UAV platform and any instrument related to position tracking and orientation adjustment of the antenna, e.g., global positioning system (GPS), inertial measurement unit (IMU), barometer, gimbal, and the link to the ground base station. Alternatively, tracking devices external to the UAV platform may be used; e.g., laser trackers, computer vision, or differential GPS (DGPS). The accuracy of each component should be taken into account when assessing the potential alignment error sources in the measurements. To achieve the principal plane cuts, accurate positioning of the UAV and proper flight strategy are required, which cover the full range of two orthogonal axes  $(\theta, \phi)$  depending on the operational mode of the AUT or radar system (e.g., mechanical or electronic scanning). It is desired that the operational coordinate system of the UAV matches that of the AUT to prevent misinterpretation of measured data and error evaluation.

As for the recording subsystem, a means to synchronize the ground station and UAV georeferencing data must be accounted for. A simple way to achieve this is by logging the position, orientation, and timestamp for each measurement taken, which is usually done automatically in the flight controller logs. Alternatively, this option may be provided by a DGPS with real-time kinematics (RTK), which further improves the position accuracy and precision.

### **3.1.3 Procedures**

Field probing by continuous movement of the UAV allows rapid and systematic experimental evaluation of those parameters which affect the level of energy coming to the AUT. In general, a distant probe is carried by an airborne vehicle, which is

maneuvered through the space surrounding the AUT to produce essentially plane waves illuminating the AUT from all directions of interest, and when the position and/or orientation of the antenna probe relative to the AUT changes, a variation in the received signal occurs. The direction to the probe with respect to a reference direction at the AUT is obtained from a tracking device which logs the position and orientation data in real time, or at post-processing. The error introduced because of the misalignment (position and orientation) between the AUT and the tracking device must be taken into account. Additionally, it may be necessary to determine the range to the probe to compute the correction, or to correct for the change in the incident power flux density caused when the aircraft does not fly perfectly along its intended route about the AUT. The amplitude of the signal received by the antenna provides the amplitude data to the recording device which is then processed to display the measurements as desired [13]. The probe must be in the FF region of the AUT, and if not possible, near- to far-field (NF-to-FF) transformation techniques and instrumentation must be used properly [38], [41], [48], [49], [59], [60].

The process of pattern measurement and recording may involve either a point-by-point or a continuous method. Various scanning strategies have been implemented for UAV-based measurements [16], [32], [53]. These include: hovering, planar (horizontal or vertical), cylindrical, and spherical (azimuth or elevation). The hovering strategy is identical, in principle, to an elevated range, with the exception that the probe antenna is now mobile, with the UAV hovering in place while the AUT is rotating. Planar scans are the simplest to implement as rectilinear flight paths in the flight controller, and can be horizontal, e.g., flying above the AUT, or vertical, e.g., a plane normal to the direction of propagation. Cylindrical scans consist of equiradial concentric circular patterns centered at the AUT with different heights. Spherical scans consist of concentric circles around the AUT either in horizontal planes or in vertical planes. A study of the time taken and the area covered for different systems is

presented as examples in [16]. Additionally, the endurance of the UAV and the length in time of the scan must be taken into consideration with regards to the measurement characteristics that are desired.

To verify the alignment between the antennas, the UAV can be operated and data gathered continuously along, and across radials, and for different altitudes around a certain region of interest to establish the relative levels of the major contributors of extraneous signals distorting the incident field and the angles of the sources from the line of sight. The probe antenna should be oriented so that the peak of the main beam is in the direction of the AUT, and the pattern should be sufficiently uniform to avoid excessive amplitude tapering across the test aperture. Careful selection of the probe antenna can further reduce the effects of extraneous reflections due to the aircraft structure and asymmetry. Additionally, to determine the polarization characteristics of the illuminating field at the AUT it is also necessary that the roll axis of the probe antenna be adjustable or that the antenna be dual-polarized. The latter is preferred since measurements for both polarizations can be obtained during a single test operation and is analogous to the STSR operation in weather radars.

## **3.2 Simulation Framework**

A simulation framework is developed which will be used in studying the feasibility of UAV-based FF measurements for weather radars, and to estimate the error levels to be expected in field experiments. This framework takes into account the design criteria presented in the previous section, as well as sources of error, and ideal models for the AUT and probe antenna (which can be replaced by any arbitrary model). This tool is important in establishing optimal scanning strategies and correction techniques when performing antenna measurements with UAVs. Additionally, the framework developed in this context shall be used to evaluate error sources in different outdoor antenna measurement configurations.

### 3.2.1 Basic Signal Model

#### 3.2.1.1 AUT and Probe Antennas

The general equations used for the complex electric field and antenna models, for dual-polarized phased array antennas, are [70], [78]:

$$E(\theta, \phi) = \frac{E_0}{r} f(\theta, \phi) \text{AF}(\theta, \phi) e^{-jkr}, \quad (3.6)$$

$$\begin{aligned} \text{AF}(\theta, \phi) = & \frac{1}{N_x N_y} \sum_m \sum_n |a_{mn}| \\ & \exp\{-jk[d_m(\sin \theta \cos \phi - \sin \theta_0 \cos \phi_0) + d_n(\sin \phi - \sin \phi_0)]\}, \end{aligned} \quad (3.7)$$

$$f(\theta, \phi) = \begin{bmatrix} f_{\text{HH}}(\theta, \phi) & f_{\text{VH}}(\theta, \phi) \\ f_{\text{HV}}(\theta, \phi) & f_{\text{VV}}(\theta, \phi) \end{bmatrix}, \quad (3.8)$$

$$f_{\text{HH}}(\theta, \phi) = [\cos(\theta) \cos(\phi)]^{n_{\text{HH}}}, \quad (3.9)$$

$$f_{\text{HV}}(\theta, \phi) = A_{\text{HV}} [\sin(\theta) \sin(\phi)]^{n_{\text{HV}}}, \quad (3.10)$$

$$f_{\text{VV}}(\theta, \phi) = [\cos(\theta) \cos(\phi)]^{n_{\text{VV}}}, \quad (3.11)$$

$$f_{\text{VH}}(\theta, \phi) = A_{\text{VH}} [\sin(\theta) \sin(\phi)]^{n_{\text{VH}}}, \quad (3.12)$$

where  $E_0$  is a constant which depends on the antenna characteristics,  $r$  is the range from the antenna,  $k$  is the wave number which is related to the operating wavelength  $\lambda$  by  $k = 2\pi/\lambda$ , AF is the antenna array factor for  $\theta$  in azimuth and  $\phi$  in elevation, with  $\theta_0$  and  $\phi_0$  the steered beam direction,  $a_{mn}$  is the excitation function of the array, and  $d_{m,n}$  is the offset of the element at the  $m$ -th and  $n$ -th positions, respectively. In addition, the element factor or antenna pattern  $f$  is a matrix defined by the co-polarized and cross-polarized antenna patterns in the horizontal or vertical polarizations denoted by:  $f_{\text{HH}}$  or H-receive/H-transmit,  $f_{\text{HV}}$  or H-receive/V-transmit  $f_{\text{VH}}$  or V-receive/H-transmit, and  $f_{\text{VV}}$  or V-receive/V-transmit. The coefficients are selected

to match typical ideal antenna pattern characteristics, where the co-polarized patterns are assumed to have a cosine variation with a coefficient  $n_{\text{HH}} = n_{\text{VV}} = 1.2$ , and the cross-polarized patterns are assumed to have a sine form with  $n_{\text{VH}} = n_{\text{HV}} = 0.4$ . The AUT is assumed, though it can be generalized, to be similar to a phased array antenna operating at a frequency of 3 GHz ( $\lambda = 10$  cm), which consists of  $N_x = N_y = 80$  elements, an aperture size of  $D_x = D_y = 4$  m, and an element spacing of  $d = \lambda/2$ . The AUT excitation function is assumed to be a uniform distribution across all elements of the array, although this may be slightly modified due to amplitude tapering effects (discussed in Section 3.1.1), which depend on the angle  $\alpha_D$  from (3.3) subtended by the AUT aperture at the probe. With said configuration, the beamwidth is equal to  $1.26^\circ$ , with a SLL of  $-13.25$  dB and a maximum cross-polarization level of approximately  $-30$  dB at  $\theta = \phi = 45^\circ$ . The probe antenna uses an equivalent model as the one described for the AUT model, with a different number of elements and aperture of the array, corresponding to a 4x4 probe ( $N_x = N_y = 4$ ) with an aperture of  $d_x = d_y = 20$  cm, a beamwidth of  $26.3^\circ$ , a SLL of  $-11.4$  dB, and a FNBW of  $60^\circ$ . The parameters selected here reflect those of the test bed that is part of this project [35], [79]. A more detailed discussion on probe beamwidth and size is presented in Chapter 4.

### 3.2.1.2 Transmission Model

Using Friis transmission equation, the amplitude of the transmitted signal can be estimated, and knowing that  $P \propto E^2$ —that is, the power delivered is proportional to the square-power of the voltage— and that the antenna directivity is related to its amplitude pattern, an expression for the signal can be obtained as

$$E_{\text{D}}(\theta, \phi) = \frac{E_0}{r_{\text{D}}} f^{\text{AUT}}(\theta, \phi) f^{\text{P}}(\theta, \phi) e^{-jkr_{\text{D}}}, \quad (3.13)$$

where the subscript D indicates direct-path ray. The probe and AUT antenna patterns are represented by

$$f^{\text{P}}(\theta, \phi) = \begin{bmatrix} f_{\text{HH}}^{\text{P}}(\theta, \phi) & f_{\text{VH}}^{\text{P}}(\theta, \phi) \\ f_{\text{HV}}^{\text{P}}(\theta, \phi) & f_{\text{VV}}^{\text{P}}(\theta, \phi) \end{bmatrix} \text{AF}^{\text{P}}(\theta, \phi), \quad (3.14)$$

$$f^{\text{AUT}}(\theta, \phi) = \begin{bmatrix} f_{\text{HH}}^{\text{AUT}}(\theta, \phi) & f_{\text{VH}}^{\text{AUT}}(\theta, \phi) \\ f_{\text{HV}}^{\text{AUT}}(\theta, \phi) & f_{\text{VV}}^{\text{AUT}}(\theta, \phi) \end{bmatrix} \text{AF}^{\text{AUT}}(\theta, \phi). \quad (3.15)$$

By combining (3.13)-(3.15) and performing the matrix multiplication, the co-polarized and cross-polarized components of the measured signal may be obtained as:

$$E_{\text{D,HH}} = \frac{E_0}{r_{\text{D}}} (f_{\text{HH}}^{\text{AUT}} f_{\text{HH}}^{\text{P}} + f_{\text{VH}}^{\text{AUT}} f_{\text{HV}}^{\text{P}}) e^{-jkr_{\text{D}}}, \quad (3.16)$$

$$E_{\text{D,VH}} = \frac{E_0}{r_{\text{D}}} (f_{\text{HH}}^{\text{AUT}} f_{\text{VH}}^{\text{P}} + f_{\text{VH}}^{\text{AUT}} f_{\text{VV}}^{\text{P}}) e^{-jkr_{\text{D}}}, \quad (3.17)$$

$$E_{\text{D,VV}} = \frac{E_0}{r_{\text{D}}} (f_{\text{VV}}^{\text{AUT}} f_{\text{VV}}^{\text{P}} + f_{\text{HV}}^{\text{AUT}} f_{\text{VH}}^{\text{P}}) e^{-jkr_{\text{D}}}, \quad (3.18)$$

$$E_{\text{D,HV}} = \frac{E_0}{r_{\text{D}}} (f_{\text{HV}}^{\text{AUT}} f_{\text{HH}}^{\text{P}} + f_{\text{VV}}^{\text{AUT}} f_{\text{HV}}^{\text{P}}) e^{-jkr_{\text{D}}}, \quad (3.19)$$

where the  $\theta$  and  $\phi$  dependency has been omitted for simplicity.

### 3.2.2 UAV Structure Influence

The signal of the probe antenna is slightly modified when it is mounted on the UAV, due to interactions (e.g., coupling and reflections) with the structure of the UAV. A few studies [54], [80]–[83] have analyzed the interaction of the UAV structure and its EM radiation properties in free space with a probe antenna; however, a way to predict such effects at S band for weather radar antenna measurement purposes has not yet been investigated. Since a model of such phenomenon would be extremely

difficult to accurately derive analytically, a simple radiating element model is chosen as

$$f_{\text{R,UAV}}^i = f^{\text{P}}(\theta_{\text{R}}^i, \phi_{\text{R}}^i) \frac{e^{-jkr_{\text{R}}^i}}{r_{\text{R}}^i} (A + B \cos(C\theta) \cos(C\phi)), \quad (3.20)$$

where  $f^{\text{P}}(\theta_{\text{R}}^i, \phi_{\text{R}}^i)$  is the value of the probe antenna pattern for the  $i$ th radiating element in the incidence direction relative to the phase center of the probe antenna,  $r_{\text{R}}^i$  is the distance to the  $i$ th radiating element, and a ripple and roll-off model is dictated by the constants  $A$ ,  $B$ , and  $C$ . Such constants are determined ad hoc to match measurements and simulations previously done for similar antennas in a controlled environment [34], [35]. The probe-only patterns, and the modified patterns with the UAV structure effects and geometries are presented in Figure 3.2b.

The hexacopter model is selected for this study, with  $L_g = 15$  cm,  $Z_g = 30$  cm,  $L_{\text{arm}} = 35$  cm, the angle between the arms  $60^\circ$ , and two radiating elements placed at the extremes of the front-facing arms with the model described by (3.20) (see Figure 3.2a). With this geometry, and the values of  $A = 0.05$ ,  $B = 0.15$ , and  $C = 30$ , a ripple of approximately  $\pm 0.16$  dB is obtained in the co-polarization pattern, with a cross-polarization level below  $-40$  dB. This effect is added linearly to the radiation pattern of the probe. By simulating an ideal probe antenna, the cross-polarization levels for the probe alone are very small, and hence, not noticeable in the plots.

### 3.2.3 Error Sources

#### 3.2.3.1 Coupling

The scattering and reradiation of energy between the probe antenna and AUT may produce a measurable error in the region of the main lobe peak if the probe antenna produces a significant illumination taper along the test aperture. This effect is usually negligible in the side lobes [14]. The following derivation is valid for AUT and probe antennas of arbitrary radiation patterns. Assuming a polarization-matched case and

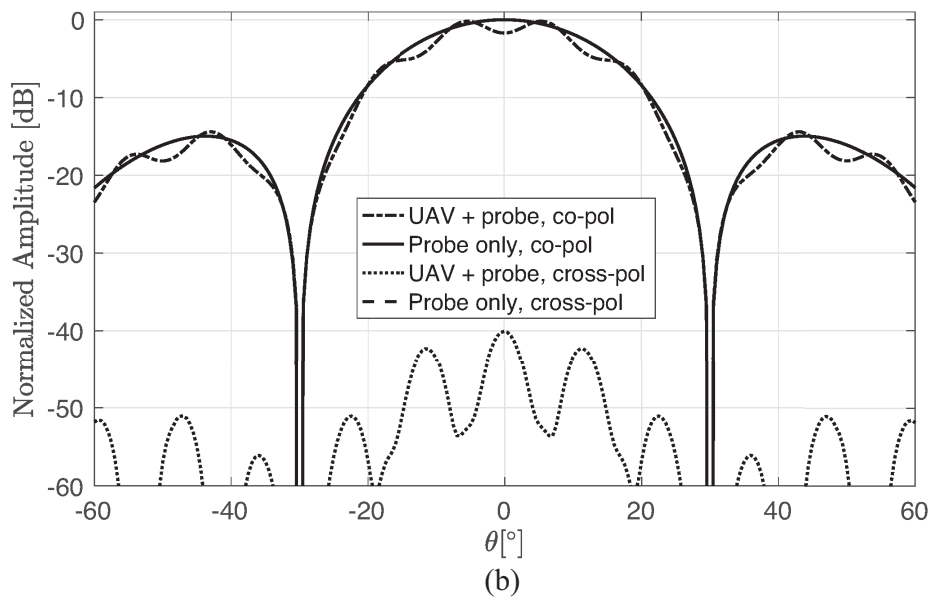
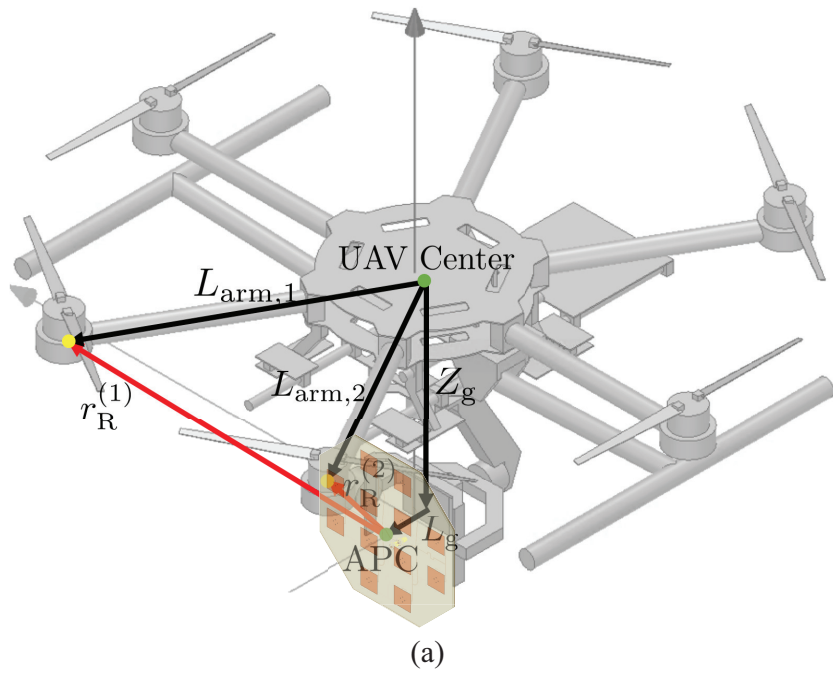


Figure 3.2: (a) Geometry for two radiating elements at the extremes of the arms of an hexacopter. (b) Antenna pattern for probe (co-polarization, solid; cross-polarization, dashed), and probe mounted on UAV (co-polarization, dash-dotted; cross-polarization, dotted).

reciprocity between AUT and probe antenna, when the load is not ideally matched, a fraction of the received signal will also be reradiated, resulting in a net combined effect of a back-scattered signal due to scattering and reradiation that may be only a few decibels below the received signal. Following the procedure from [14] in a more general sense and noting that  $P \propto E^2$ , the effect of the coupling between the AUT and probe may be estimated as:

$$E_C(\theta, \phi) = k_s k_r \frac{E_0}{r_D^2} f^{\text{AUT}}(\theta, \phi) f^{\text{P}}(\theta, \phi) e^{-j2kr_D}, \quad (3.21)$$

where  $E_C$  is the coupled illuminating field received at the AUT due to reradiation and  $k_s, k_r$  are the coefficients of the back-scattered and retransmitted signals, respectively. Typical values of  $k_s = k_r = 0.25$  as reported in [14] are used throughout the analyses. Then, the error contribution in the measurement due to coupling can be estimated as

$$\Delta E_C = 20 \log \left( 1 \pm \frac{E_C}{E_D} \right). \quad (3.22)$$

### 3.2.3.2 Extraneous Reflections

The coherent interference of an extraneous signal with the direct-path signal will produce a well-defined interference pattern at the AUT if the level of the composite reflected signals relative to the direct-path signal is significant [14]. For this work, it is assumed that a signal is being reflected off of the surface in front of the AUT; see Figure 3.3 for a diagram.

A simple ground reflection model is selected, and the signal is defined as:

$$E_R(\theta, \phi) = \frac{E_0 \Gamma(\alpha_R)}{r_R} f^{\text{AUT}}(\theta, \phi - \alpha_R) f^{\text{P}}(\theta, \phi - \alpha_R) e^{-jkr_R}, \quad (3.23)$$

with [84]

$$\Gamma(x) = \frac{\sin x - R}{\sin x + R} \quad (3.24)$$



for  $E_D > E_R$ , which can account for both in-phase and out-of-phase signals. In the unlikely event that  $E_D < E_R$ , the expression  $\Delta E_R = 20 \log(E_R/E_D \pm 1)$  is used instead.

### 3.2.3.3 Position and Orientation Misalignment

Measurement errors from a number of sources related to the alignment, i.e., position and orientation, of the AUT and probe antennas must be considered when determining the accuracy of the antenna range. For UAV-based measurements, these errors are related directly to the accuracy of the individual component, which have an impact on the position and orientation of the platform. Position and orientation drifts may occur due to the difference between their real value and the value that is measured, which is subject to inaccuracy of the instrument, environmental conditions (e.g., wind), and the flight controller control algorithm. Each instrument has its intrinsic errors (e.g., bias, drift, noise figure, etc.), which can be found in the datasheet, that affect the precision of the measurement of the radiation pattern.

In the simulation framework,  $x$ ,  $y$  and  $z$  denote the real position of the UAV in a cartesian coordinate system with the origin at the AUT phase center analogous to the east-north-up (ENU) coordinate system, and  $\Delta x$ ,  $\Delta y$  and  $\Delta z$  their uncertainties in the respective directions (which are predominantly affected by the GPS accuracy; the barometer accuracy affects the height measurement for the most part). The distances between the AUT and the center of the UAV are given by  $r_D = \sqrt{x^2 + y^2 + z^2}$  (real), and  $r'_D = \sqrt{(x + \Delta x)^2 + (y + \Delta y)^2 + (z + \Delta z)^2}$  (measured). Assuming there is no alignment error in orientation, the difference between real and measured positions would generate a difference in path loss of

$$\Delta L_o = 20 \log \frac{r_D}{r'_D}. \quad (3.27)$$

In addition to an offset in position, the uncertainties may propagate to the relative orientation between the AUT and the UAV. The real and measured  $\theta$  and  $\phi$  angles may be obtained as:  $\theta = \cos^{-1} \frac{z}{r}$ ,  $\theta' = \cos^{-1} \frac{z+\Delta z}{r'}$ ,  $\phi = \tan^{-1} \frac{y}{x}$ , and  $\phi' = \tan^{-1} \frac{y+\Delta y}{x+\Delta x}$ . This effect produces a change in the amplitude and phase of the radiation pattern being measured, in the sense that the relative direction between the probe antenna and AUT is different from boresight. Assuming the AUT is stationary at the time step where the measurement with the UAV is taken, and that there is no position error, then

$$\Delta L_o = 20 \log \frac{f^P(\theta', \phi')}{f^P(\theta, \phi)}, \quad (3.28)$$

represents the change in the radiation pattern due to the AUT and probe misalignment.

### 3.2.4 Total Measured Signal

The total measured signal is obtained as the sum of the transmitted direct-path signal, and the effects of perturbations considered herein, which can be summarized as:

$$E_T = E_{D_{dB}} + \Delta E_R + \Delta E_C, \quad (3.29)$$

from which the total error between the measured and real signals can then be computed. It is noted that, these effects are directly or indirectly related to the wave number  $k$ , and as such they scale accordingly with the operating frequency of the system.

## 3.3 Analysis

In the previous sections, the methodology and models used herein have been explained, in addition to how the errors are evaluated. Clearly, any variable that is

dependent on the position and orientation of the AUT and/or probe will be potentially affected by vibrations, instabilities, and misalignment, which would produce variations in the measured signal. As such, the misalignment errors are generally coupled with the coupling and reflection errors, and it would be very difficult to create an error budget for every error source. Thus, the analysis here will focus mainly on position and orientation errors in the measurements.

Two cases are discussed and compared: the elevated range model (i.e., similar to hovering but with little to no perturbations in position and orientation), and the hovering UAV-based model. A brief discussion shall be presented on the overall aspects that are critical to each setup and how to mitigate potential error sources.

### 3.3.1 Probe in Elevated Range

In this scenario, the AUT is mounted on top of a structure with  $h_r = 12.2$  m above the ground, and the probe is mounted on a pedestal separated by a distance of  $R = 425$  m, at a height of  $h_t = 40$  m above the ground, which attempts to replicate a test setup presented in [79]. With this configuration, the FF distance criterion is achieved with a factor  $K = 2.66$ , based on equation (3.1), and the phase curvature inductive coupling effects and can be safely disregarded. There is no significant longitudinal taper, and for the selected probe characteristics, the beamwidth is sufficiently larger than the angle subtended by the AUT at the probe, such that the mutual coupling and transversal taper effects are within the suggested design requirement limits. In other words, the beamwidth at the 0.25 dB level is  $\theta_{0.25} = 3.4^\circ$  for the probe antenna, and  $\alpha_D = 0.54^\circ$  in this scenario, such that the criterion  $\theta_{0.25} > \alpha_D$  is met. However, with a wide beamwidth, ground reflections are of concern in this setup, since the ground reflection criterion is not met, i.e.,  $\text{FNBW}/2 > \alpha_{h_r}$ , with  $\alpha_{h_r} = 1.63^\circ$  and  $\text{FNBW}/2 = 30^\circ$ . In addition to the effect of reflections, variations in the position of the probe (e.g., due to load changes, deflections, wind), and variations in the orientation of the

probe (e.g., due to vibration and accuracy of the positioner, and misalignment effects derived from variations in position) will also contribute to measurement errors.

The probe is assumed to be fixed atop the pedestal pointing directly towards the AUT, and the position errors are modeled independently for the three Cartesian axes  $(x, y, z)$  as a zero-mean Gaussian distribution with their respective standard deviations  $(\sigma_x, \sigma_y, \sigma_z)$ . The parameters for the Gaussian error model have been determined through actual experiments in the field: with the UAV stationary at different locations higher than the ground to avoid GPS multipath issues, with the UAV hovering above some height off the ground in calm winds, and with the UAV hovering in relatively strong winds. A statistical analysis of the positioning in each case was produced, and the standard deviations were derived for the error models. Since the positioning error can be manually adjusted in the simulated framework, the error analysis becomes decoupled from the specific type of hardware being used; thus, virtually any hardware from different vendors can be tested. The values selected here represent the platform used in this study; the results for a GPS, and a DGPS device have been presented in [34]. The AUT is assumed to be fixed atop a robust tower, such that there are no errors in position (i.e., the AUT is not rotating), and the scan is performed electronically by means of beam steering from  $-45$  to  $45^\circ$  in azimuth and at a fixed elevation of  $0^\circ$  relative to the AUT. The accuracy for typical indoor test range equipment, can be found in [14]. Here, an example is provided with  $\sigma_x = \sigma_y = 1$  cm, and  $\sigma_z = 3$  cm, corresponding to calm wind conditions and a relatively smooth terrain, such that there is no significant variability of the position in any direction. A number of samples ( $M = 20$ ) are taken for each direction, similar to standard measurement techniques. Figure 3.4 shows the simulated patterns with and without errors, averaged over 20 samples per direction in azimuth.

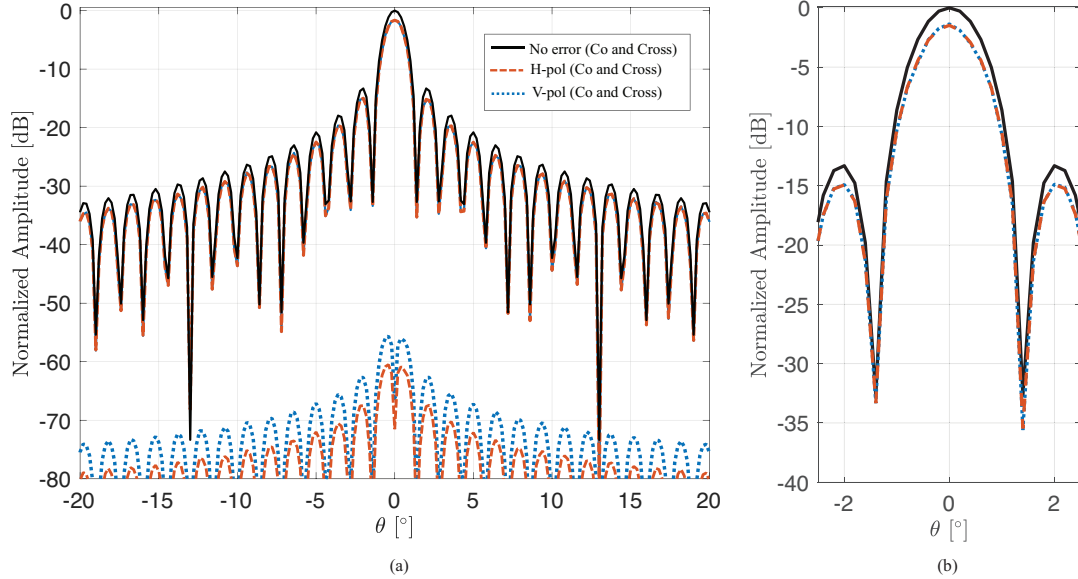


Figure 3.4: Case of the probe in an elevated range. (a) Simulated measurements with (blue, red) and without (black) errors for H-polarized (blue) and V-polarized (red) antenna patterns, with top lines corresponding to co-polarization patterns, and bottom lines corresponding to cross-polarization patterns. (b) Zoomed-in plot.

Both sets have been normalized with respect to the errorless pattern, and the reduction in directivity is apparent. Between the polarizations; however, the co-polarization bias is 0.02 dB, while the cross-polarization bias is in the order of 5 dB. This difference is explained by the fact that the ground-reflected signals can be adding either constructively or destructively depending on the difference of the direct-path and reflected-path lengths, which has different effects depending on the polarization. The higher cross-pol level remains below the required threshold at about  $-55$  dB.

### 3.3.2 Probe Mounted on a UAV

#### 3.3.2.1 Hover Mode

A scenario similar to Case I is studied next, where the UAV is hovering about the height of the pedestal of the elevated range configuration. The main differences between the two cases are that the position errors are much higher due to the lower accuracy of the instruments (e.g. DGPS, IMU, and baroaltimeter) on the UAV,

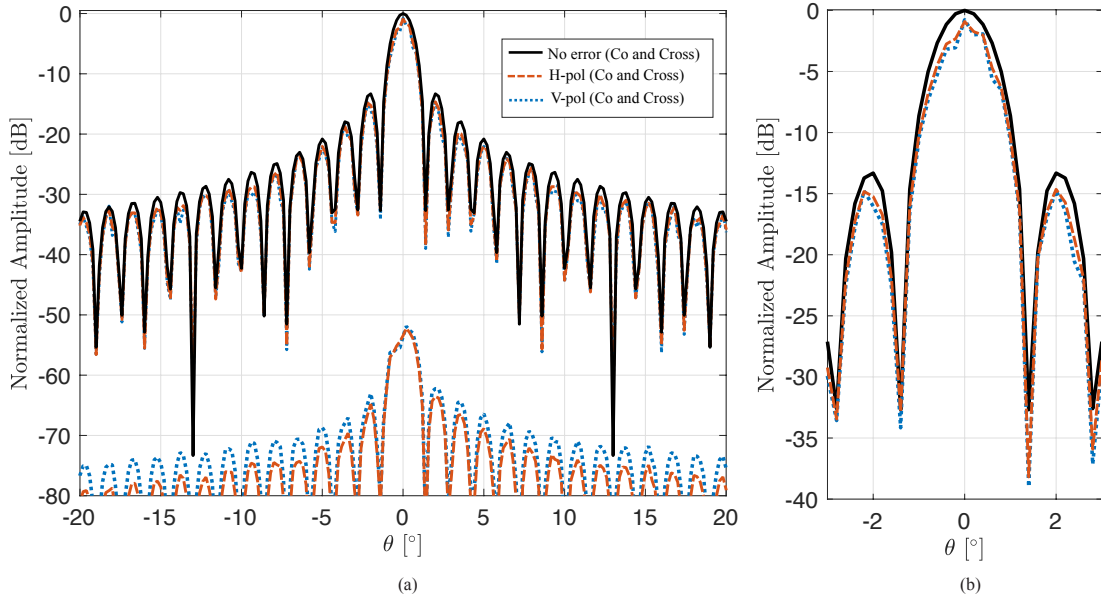


Figure 3.5: Case of the probe mounted on a UAV. (a) Simulated UAV-based measurements with (blue, red) and without (black) errors for H-polarized (blue) and V-polarized (red) antenna patterns, with top lines corresponding to co-polarization patterns, and bottom lines corresponding to cross-polarization patterns. (b) Zoomed-in plot.

and the orientation errors due to gimbal inaccuracy. For the sake of simplicity, the orientation accuracy for the roll, pitch, and yaw axes of the UAV relative to the gimbal are not taken into account, though it is noted that the propagation of such errors would ultimately induce an error in the pointing direction of the gimbal. Previous benchmark testing on the equipment used in this study provides the expected accuracy for the UAV system under calm winds, with  $\sigma_x = \sigma_y = 10$  cm,  $\sigma_z = 30$  cm, and the azimuth and elevation accuracy  $\sigma_\theta = \sigma_\phi = 0.02^\circ$  per vendor specifications. The simulation is run with the AUT scanning electronically, while the probe mounted on the UAV is hovering at an altitude of approximately 40 m above ground level, taking 20 samples for each direction in azimuth. The results are shown in Figure 3.5.

Although subject to the random nature of the iterations in the simulation, the features that are evident are the asymmetry and the higher cross-pol level introduced by the UAV structure itself, and the higher variability in the measured patterns,

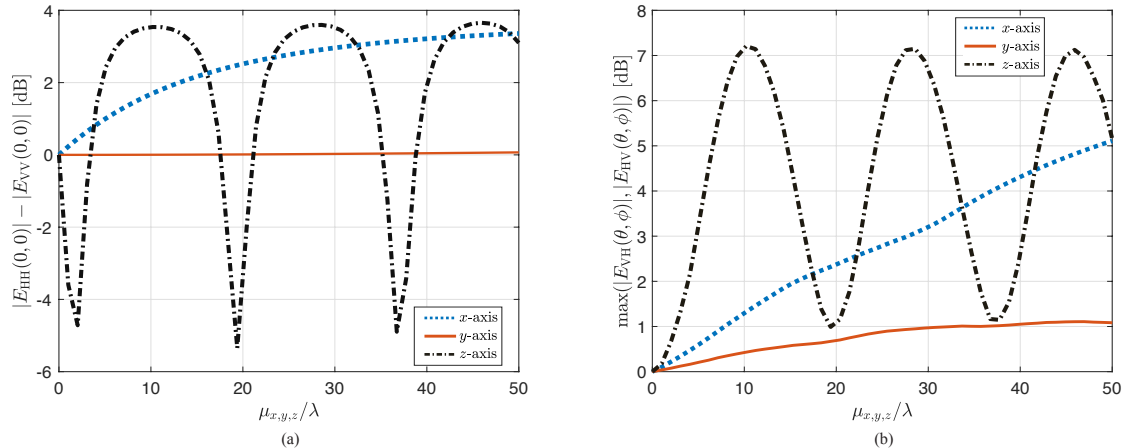


Figure 3.6: Normalized variations for the different directions in the  $x$ - (east),  $y$ - (north), and  $z$ - (north) axes as function of the bias in position for: (a) co-polarization mismatch levels, and (b) cross-polarization level increment.

still evident even for 20 averaged samples, due to higher position and orientation errors. Additionally, the null of the “real” cross-polarization pattern at boresight is obscured by signal contamination. In this particular case, the co-polarization bias is seen to increase to 0.15 dB, and the cross-polarization pattern level is approximately 3 dB higher than in the elevated range measurement. It is important to note that no probe correction techniques have been applied to these data sets, and as such, improvements on the estimates can be made but are out of the scope of this work. However, other works [16], [31], [34], [35] have dealt with mitigating the effects of reflection, diffraction, and scattering off the UAV.

### 3.3.2.2 Vertical Grid Mode

In weather radars, it is very important that there is little to no co-polar mismatch between the H-polarized and V-polarized signals, as this may lead to potential errors in weather radar polarimetric variables (e.g., differential reflectivity, co-polar correlation coefficient, differential phase) [12]. With the use of UAVs, it would be possible to measure the polarimetric mismatch over a particular spatial extent, and with the

use of this information produce a calibration scheme to produce more accurate polarimetric variables. This proposed method would be even more important when using phased array antennas as part of the transmission system in weather radars since by electronically steering the beam, squinting and projection issues will be present.

In this case study, the UAV is scanning in a planar  $yz$  grid with a separation of approximately 425 m in  $x$ ,  $-425 < y < 425$  m,  $40 < z < 220$  m, and the gimbal is assumed to be always pointing directly towards the direction of the electronically steered beam, subject to error sources as previously described. The selected spatial range roughly corresponds to an electronically scanned grid of approximately  $-45 < \theta < 45^\circ$  in azimuth, and  $0 < \phi < 20^\circ$  in elevation. It should be noted that covering such a large spatial extent in reality would be a cumbersome task, and the intended purpose here is to show the capabilities of the framework developed for this work as a potential tool for evaluating error sources in UAV-based antenna measurements and polarimetric calibration.

Figure 3.7 shows a sketch of the grid setup (top) and the corresponding co-polarization mismatch at each point of the grid, with (right) and without (left) measurement errors. As was shown in the previous cases, the main contributor to the mismatch is the error due to the physical position of the UAV which is dominated by extraneous reflections. The effect of misalignment is more important for the variation in cross-pol levels, which can also contribute to co-polar mismatch if said errors are sufficiently high. In this particular case, the range of the mismatch variation across the grid is mostly dictated by the reflection models that were assumed. The range of variability in the co-polarization mismatch is similar to those that result from the positioning bias (Figure 3.6, left). However, in a real measurement setup, the co-polar mismatch can be measured in a similar manner and proper calibration techniques may be implemented to correct polarimetric errors.

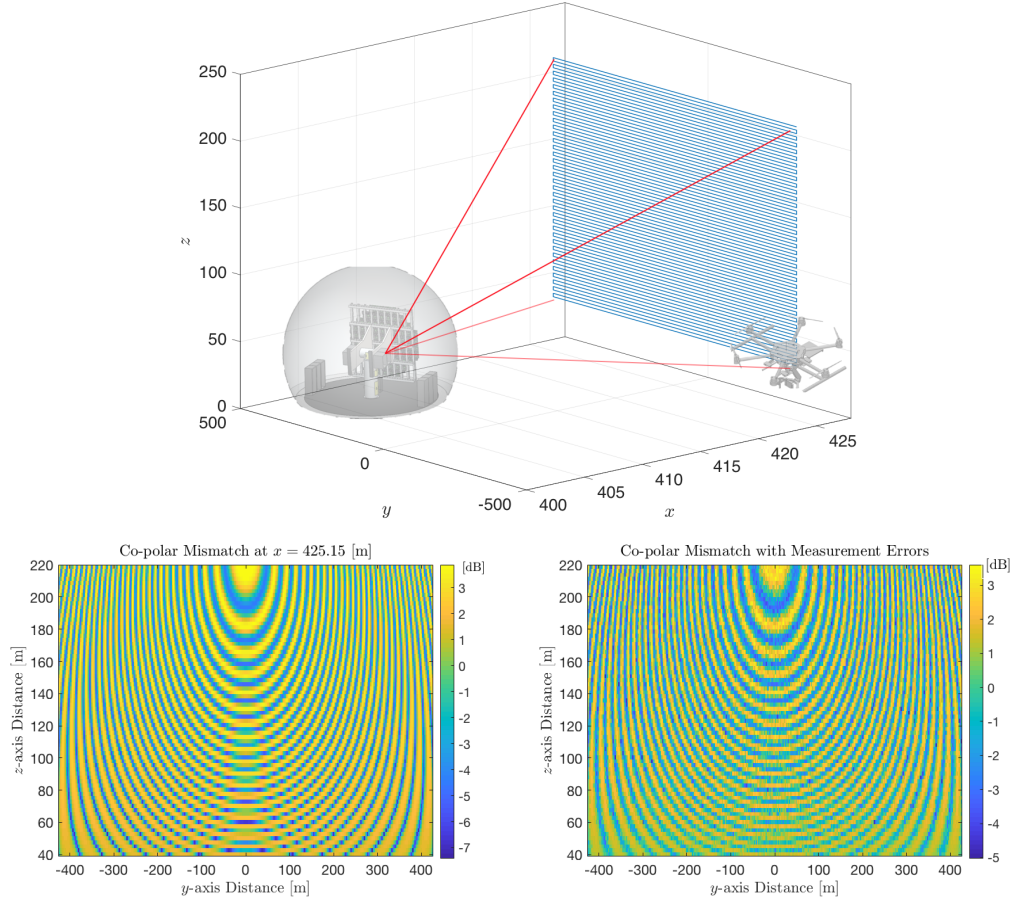


Figure 3.7: (Top) Sketch of the scanning grid, and the simulated co-polar mismatches at a distance of  $x = 425.15$  [m] without (left) and with (right) measurement errors.

### 3.3.3 Misalignment Error Analysis

In addition to analyzing the effect of flight precision with a UAV (represented herein as Gaussian models with a given mean and standard deviation), it is important to study the effect of inherent biases in positioning and targeting with the mobile system, i.e., when the mean is different from zero. Such biases may be introduced by means of gimbal drift, instrumentation biases, measurement noise, and probe misalignment, to name a few. The relative orientation between probe antenna mounted on the UAV's gimbal, and the AUT, can have a substantial effect in modifying the radiation pattern of the probe antenna, as was discussed in previous sections. As such, an estimation of the errors introduced by this misalignment is extremely important in attaining the

desired accuracy and precision for the weather radar system requirements. While [54] has dealt with a similar problem, this approach attempts to tackle the problem considering variations both in azimuth and elevation for different gimbal orientations. It should be noted that this analysis corresponds to a  $4 \times 4$  probe antenna, the AUT described previously, and for assumptions regarding coupling and extraneous signals that were derived for the purpose of this work. However, such analyses may be extended to a large number of different scenarios, provided that the relevant parameters can be sufficiently estimated.

Figure 3.6 shows the co-polarization pattern mismatch at boresight (i.e., the deviation between the H-polarized and V-polarized signals), and the normalized cross-polarization level variation for various displacements in the  $x$ -,  $y$ -, and  $z$ - axes as function of  $\lambda$ . The ordinates represent the increase or decrease in variable of interest, while the abscissa represents the position bias normalized by the wavelength. It can be seen that the  $y$ -axis position errors are the least affected, as expected, since the motion along this axis would be mostly transversal to the direction of propagation. In the direction of the  $x$ -axis, a longitudinal taper due to the path loss has a greater effect, while in the  $z$ -axis, though also a transversal motion, the ground reflections produce a ripple effect as explained in [14]. While the range of motion being analyzed is rather large (up to  $50 \lambda$  or 5 m), standard GPS modules can have uncertainties of a few meters. Moreover, this highlights the importance of having position accuracy and precision in the order of a few centimeters whenever possible such that these variations are kept to a minimum. Additionally, the altitude uncertainties are usually higher than those in the  $x$ - and  $y$ -axes, and the use of a lidar for altitude reading may aid in improving the antenna measurements.

Misalignment between the AUT and probe may also be a source of error as previously mentioned. For this, the biases of the signal for both co- and cross-polarization components is studied as a function of the gimbal elevation bias. Figure 3.8 shows

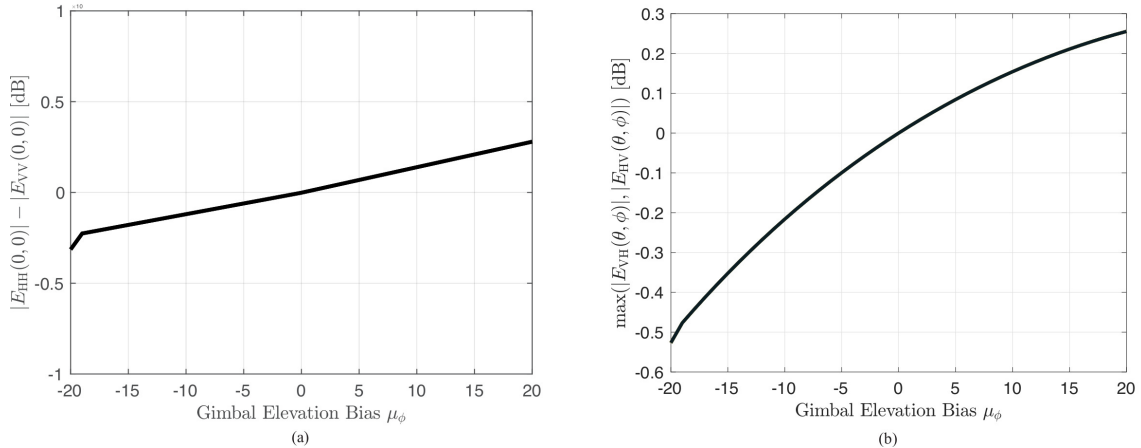


Figure 3.8: Normalized variations as function of the bias in gimbal elevation for: (a) co-polarization mismatch levels, and (b) cross-polarization level increment.

the co-polarization mismatch and the cross-polarization level variation as function of the bias in gimbal elevation angle. It is apparent that the cross-polarization signal is attenuated at lower elevation angles due to the fact that there are less reflections off the UAV structure. However, the actual values of the levels are dependent on the model being used, and one must be critical when interpreting results as they may be higher for different setups. Also note that the positioning accuracy must be sufficiently good, in addition to the gimbal accuracy, because misalignment is also affected by the relative position between the AUT and the UAV-probe system.

The biases in gimbal azimuth can also introduce measurement errors. Figure 3.9 shows plots similar to Figure 3.8, except that the abscissa is now the bias of the gimbal azimuth angles for different probe array antennas. The co-polarization components are seen to have a very small variation, suggesting that it is practically independent of the array antenna size. More importantly, it can be seen that the cross-polarization levels exhibit a relatively predictable behavior for arrays with wider beamwidths and at small azimuthal biases (i.e.,  $|\mu_\theta| < 2^\circ$ ) though in increasing nature, while for more directive beamwidths, it shows the opposite behavior—that is, the levels are lower but exhibit a pattern similar to that of the probe antenna’s array factor. In general, this is desired because the cross-polarization levels are actually lower than

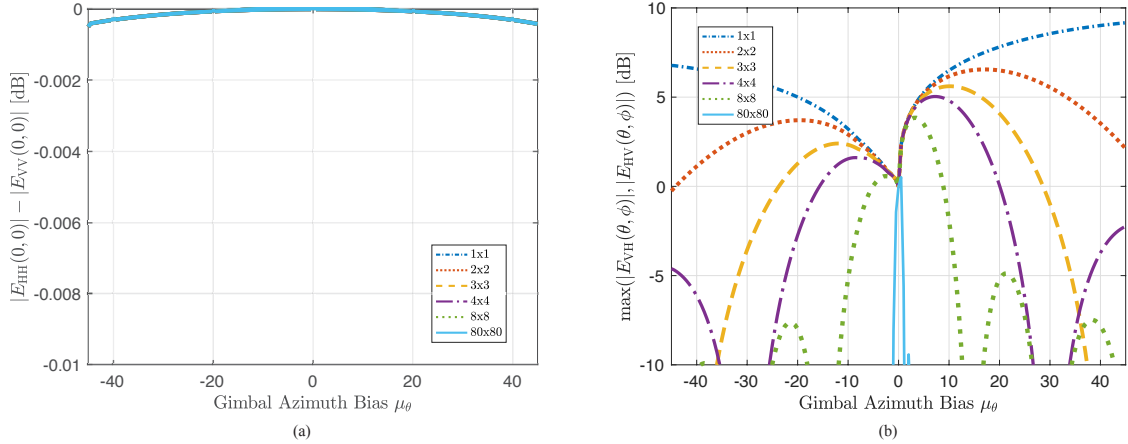


Figure 3.9: Normalized variations as function of the bias in gimbal azimuth, and for different probe array configurations of  $1 \times 1$ ,  $2 \times 2$ ,  $3 \times 3$ ,  $4 \times 4$ ,  $8 \times 8$ , and  $80 \times 80$  elements, for: (a) co-polarization mismatch levels, and (b) cross-polarization level increment.

that without azimuth bias; however, the main drawback here is that with increasing probe antenna size, it becomes harder to be physically feasible (UAV payload and size constraints). As such, it should be noted that larger probe antennas presented here are intended only for reference and not necessarily the “holy grail” for UAV-based antenna measurements for weather radars. Additionally, while the range of azimuth bias is set arbitrarily large (ideally, this measurement bias should not be larger than a few degrees off boresight), this exercise illustrates the wide range of variation for the cross-polarization component of the probe antenna. It should be understood that the dominating effects for this variability are reflections off of extraneous sources and from the structure of the UAV itself.

### 3.3.4 Discussion

It is shown that for the fixed probe (case I), the co-polarization mismatch is in the order of 0.02 dB, while the cross-polarization bias is in the order of 5 dB above the nominal level; while for the mobile probe (case II), the co-polarization mismatch

is 0.15 dB and the cross-polarization level is approximately 8 dB higher than expected. This is attributed to the errors in position, due to differences in the accuracy ( $\sigma_x, \sigma_y, \sigma_z$ ) between both cases. This suggests that as long as the positioning precision of the UAV is increased, the co- and cross-polarization requirements of 0.1 and  $< -50$  dB, respectively, for polarimetric weather radars can be achieved. Additionally, it is desired that the gimbal operation mode allows targeting the AUT within an acceptable range, such that the biases introduced due to gimbal azimuth and elevation misalignment are minimal. In other words, the relative orientation between the probe antenna and the UAV frame should be known and used as an advantage. For example, the least amount of error introduced in the measurement both for the co-polarization mismatch and the cross-polarization levels is when the gimbal is aligned with the nose of the UAV frame; and if the orientation of the gimbal varies within  $\pm 5^\circ$  in either azimuth or elevation, then a co-polarization mismatch of  $< 0.1$  dB and a cross-polarization bias of  $< 5$  dB can be guaranteed.

Based on the results provided here and under the assumptions made for these particular cases, it is recommended to use a probe antenna with as narrow a beamwidth as possible while still being physically realizable, and to prioritize the altitude accuracy over the  $x$ - $y$  accuracy to keep the error levels at a minimum. Additionally, it must be understood that the variance of the measurements (caused mostly by variations about the mean position and orientation) may be reduced by taking more samples for averaging, which would introduce an error level similar to that of the UAV hovering about a nominal position. However, actual biases in the position and orientation are stronger sources of errors, as was shown. Also worth mentioning is the fact that a larger probe antenna will impact negatively on the payload and endurance of the UAV system, thus limiting the scanning strategy possible with a particular system. The larger the aperture of the AUT, the greater the FF distance, and the selection

of a scanning strategy that maximizes the endurance (minimizes the time taken for a desired scan) becomes important.

### 3.4 Summary

Recommendations for UAV-based antenna characterization have been presented with an analysis of the errors for particular cases, and a framework which allows the evaluation of errors due to position, orientation, and extraneous error sources has been developed. The results are analyzed for different case studies which can provide the error bounds and limitations for various characterization schemes.

By assuming a static source (i.e., minimal position variation), the errors for an elevated range have been evaluated, which yielded a co-polarization mismatch of approximately 0.02 dB, and a cross-polarization level of approximately  $-55$  dB. A similar case study but for a UAV hovering about the same height as the pedestal for the elevated range case has been studied, which yielded a co-polarization mismatch of 0.15 dB and a cross-polarization level of approximately  $-52$  dB, which suggests that a UAV-based antenna characterization method can be as effective as an elevated range, provided that the accuracy of the navigation and tracking system are sufficient. Also note that in neither case probe correction techniques have been applied, which would further improve the error levels. In a similar manner, the dependency of the position biases indicated that a bias in the altitude measurements can produce large variations in the error levels of the co- and cross-polarization patterns. The dependency with regards to the  $x$ -axis position bias, which relates to the longitudinal distance from the AUT, was also of significant according to the results. The transversal motion along the  $y$ -axis yielded the smallest errors. The gimbal azimuth bias has a strong effect on the cross-polarization levels, which can be mitigated by the use of more directive probes; however, the trade-off is that it impacts the payload and endurance of the UAV negatively, and thus, this factor must be considered when selecting the probe for

a particular mission. In general, this azimuth bias should be kept to a minimum with gimbal subsystems that can provide better tracking accuracy, usually in the order of  $\pm 0.02^\circ$ . The variation in the co-polarization mismatch due to gimbal azimuth bias is shown to be less affected by misalignment. Additionally, in a similar manner, gimbal elevation biases can have an effect of varying the co-polarization mismatch and the cross-polarization levels, which is shown to be attenuated as the gimbal points away from the direction of UAV reflections.

This suggests and supports the feasibility of such a system for antenna characterization and polarimetric calibration of antennas.

## Chapter 4

### Frame, Gimbal and Probe Antenna Coupling

The probe antenna used for characterizing the AUT must also adhere to the strict requirements imposed by the characterization and calibration requirements of the weather radar system. Due to scattering and diffraction effects from the UAV structure (i.e., interaction of the probe antenna and UAV), the radiation characteristics of the probe antenna are degraded. Preliminary results from indoor measurements have shown that said interaction produces ripples in the pattern, which degrades the co-polarization matching between the H- and V-polarizations, and the cross-polarization levels. To adequately calibrate such systems, it is important that these effects are compensated or mitigated. This study attempts to determine to what extent the antenna radiation pattern for different types of antenna is affected by the structure of the UAV focusing on its application in FF (far field) measurements. Additionally, the use of a gimbal as a means to control the orientation of the probe antenna is also analyzed in this work.

For different antenna types, EM simulations of the probe antenna in free space and mounted on the UAV, which attempt to qualitatively describe the effects of the UAV on the radiation characteristics, are presented first. Next, the simulation performance of each antenna type with respect to the desired standards is discussed. Then, as a means to validate some of the results presented herein, anechoic chamber

measurements are presented. Finally, a brief discussion summarizing the findings of this work is presented in the summary.

## 4.1 Simulations

A probe antenna that is mounted on a UAV platform for EM field measurements will present radiation characteristics that will be adversely affected by the coupling and scattering effects due to the proximity to its surrounding structure. Moreover, antennas can have different radiation characteristics depending on their type; thus, as the EM fields produced by the antenna interact with the UAV and gimbal structure, they are expected to be correspondingly different. Because of the directional properties and the complex mechanics of this phenomenon, developing accurate analytical models to describe such effects still remain a challenge. In this context, EM simulation software can provide a means to describe such effects with relative accuracy.

A simple model of the UAV platform used for this project [35] is recreated in ANSYS HFSS, and simulated in finite element method (FEM) and hybrid method (finite element bounded integral, FE-BI), where the electrically large structure (i.e., UAV and gimbal) is treated with the integral equation method, while the radiating element (i.e., probe antenna) is treated with the FEM method. This decreases the computational complexity of the problem and improves the time taken to complete the simulation, while maintaining an acceptable level of precision. In the following simulated cases, the UAV frame and gimbal are assumed to be leveled with respect to the horizon, stationary, and with the landing gear raised. In other words, the roll, pitch, and yaw angles for both the frame and the gimbal will be  $0^\circ$ . The frequency of the analysis is 3 GHz ( $\lambda = 10$  cm) and the antenna types studied are: dipole, microstrip patch, horn, and patch array. All cases are presented with the antenna radiation patterns of the antenna in free space and mounted on the UAV, showing the co- and cross-polarized components for H-pol and V-pol in the principal planes

(E, D, and H). Additionally, a surface current plot in logarithmic scale is provided to show the region in the UAV and gimbal structure where the currents are more significant (see Figures 4.1-4.3). Each case is discussed in the following sections.

### 4.1.1 Dipole

For the case of a dipole [15], the radiating element is aligned along the  $x$ -axis for H-pol (Figure 4.1a, first column), and along the  $y$ -axis for V-pol.

The radiation patterns for the E-, H-, and D-planes are shown in Figure 4.1a second, third, and fourth columns respectively, where the patterns for the dipole in free space are shown in black lines, and for the UAV-mounted in blue, green, and red lines, for the co- (continuous), and cross-polarization (dashed) components. The surface current induced in the UAV structure is shown in Figure 4.2a.

Clearly, the effect of scattering from the structure can be seen in both co- and cross-polarization patterns in every cut. The co-polarization pattern exhibits ripples about the nominal pattern for the dipole without the UAV, and the cross-polarization pattern increases to approximately  $-20$  dB off boresight, from less than  $-50$  dB. Moreover, it is observed that the increase in the cross-polarization level is less affected in the H-plane. The degradation of the radiation pattern is quite significant in this case, and it can be hypothesized that the broader the radiation characteristic of the antenna element is, the higher it scatters back from the UAV structure and further contaminates the co- and cross-polarization patterns. Additionally, Figure 4.2a shows currents being induced more intensely on the gimbal surface than on the UAV frame properly. In this case, the back lobe radiation from the dipole may have a more significant effect in contaminating the antenna radiation patterns than the front lobe radiation.

For V-pol (Figure 4.3a), the effects are similar but occur at different planes. That is, the co-polarization ripples are higher in the E-plane rather than in the H-plane as

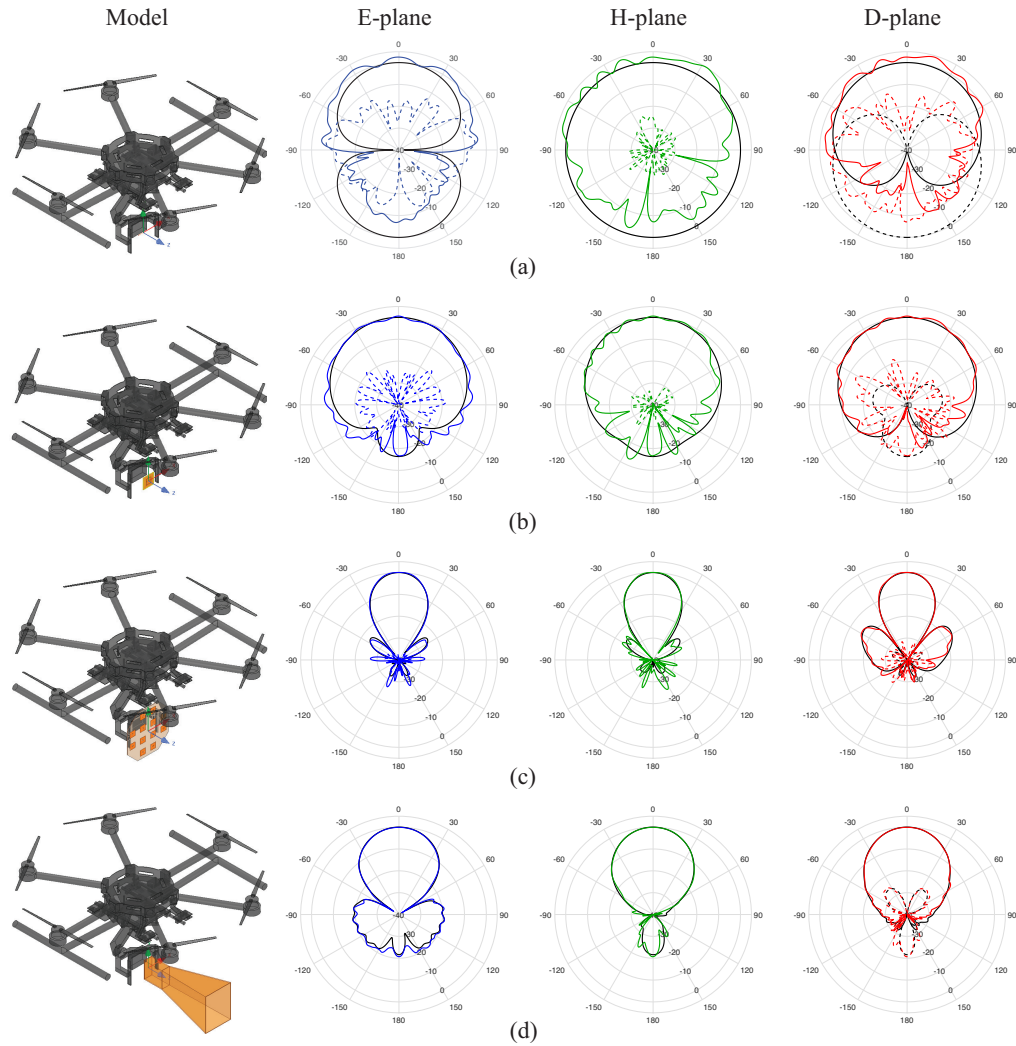


Figure 4.1: H-polarization model of the probe antenna and UAV (first column), and radiation patterns in the E- (second column), H- (third column), and D-planes (fourth column) for: (a) dipole, (b) patch, (c) 4x4 array, and (d) horn antenna. Colored lines correspond to the radiation patterns of the probe antenna mounted on the UAV, while black lines correspond to the probe antenna in free space.

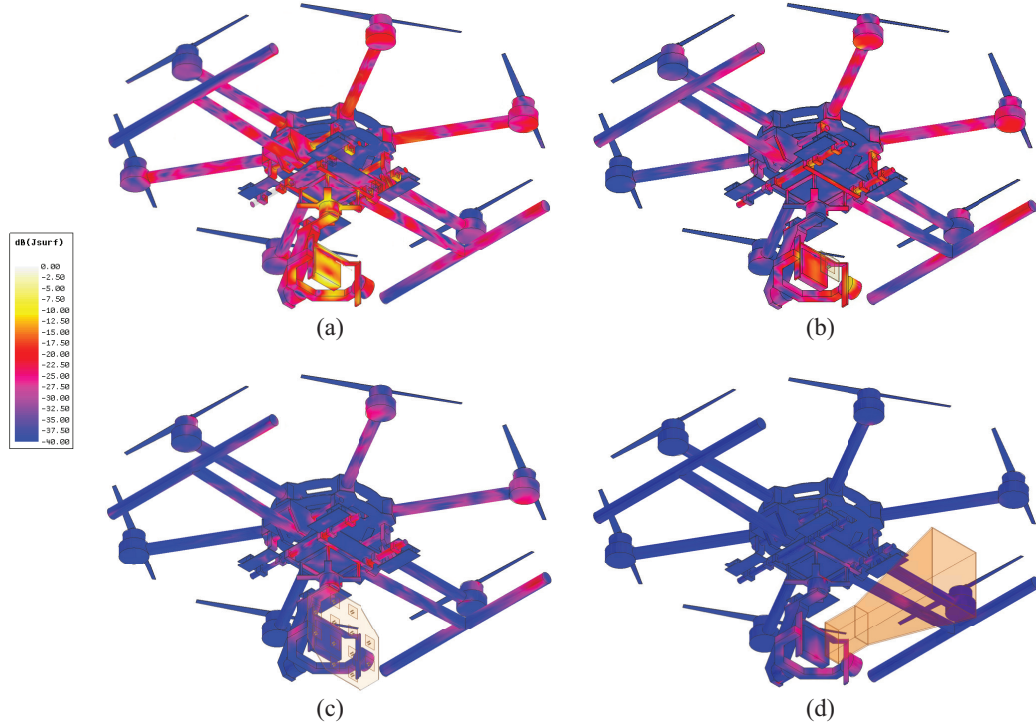


Figure 4.2: H-polarization surface currents induced in the UAV for: (a) dipole, (b) patch, (c) 4x4 patch array, and (d) horn antenna.

it was in the H-pol case; and, the cross-polarization levels are higher in the H-plane, rather than in the E-plane. The surface currents induced in the UAV in this case are more confined within the gimbal and landing gear region, and not as widespread throughout the frame as it was in the other case.

### 4.1.2 Microstrip Patch

The microstrip patch antenna [15] analyzed here is dual-polarized and differentially fed (Figure 4.1b). This differential feed patch in free space exhibits a cross-polarization level less than  $-45$  dB near boresight (Figure 4.1b). However, when the patch antenna is placed on the UAV and gimbal, the ripples on the co-polarization pattern are relatively weaker compared to the dipole overall, and the cross-polarization level increases near boresight on average by approximately 15 dB in the E-plane, 10 dB in the H-plane, and 20 dB in the D-plane, for H-pol. Notably, the cross-polarization

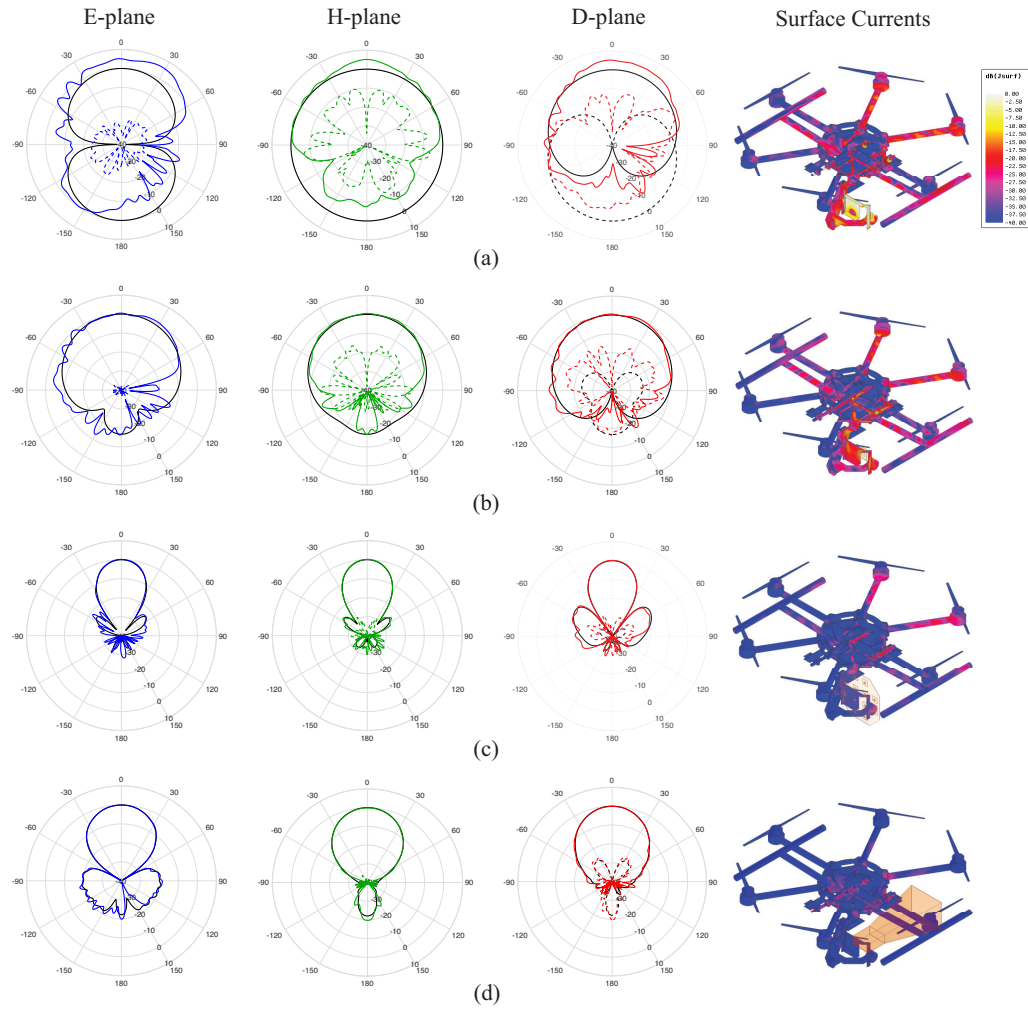


Figure 4.3: V-polarization radiation patterns in the E- (first column), H- (second column), and D-planes (third column), and surface currents on the UAV for: (a) dipole, (b) patch, (c) 4x4 patch array, and (d) horn antenna. Colored lines correspond to the radiation patterns of the probe antenna mounted on the UAV, while black lines correspond to the probe antenna in free space.

level in the H-plane exhibits a similar behavior as with the dipole case, where it seems less affected than in the other two cuts. This is arguably because the vertical plane is a plane of symmetry for the UAV structure, and therefore, the fields producing such an increment in the cross-polarization level are canceling out. Additionally, the more directive nature of the radiation characteristics in a patch antenna is shown to induce less surface currents in the UAV structure as compared to the case with the dipole, as shown in Figure 4.2b.

Similar observations made with the dipole in V-pol are made for the patch in V-pol (Figure 4.3b), where the E-plane co-polarization ripples are higher and cross-polarization levels are lower, and vice versa for the H-plane. This could be attributed to the vertical plane of symmetry as previously mentioned. Additionally, the surface currents show stronger induced currents in the arms and landing gear of the UAV than it is in H-pol.

### 4.1.3 Patch Array Antenna

Conducting a similar analysis for a 4x4 dual-polarized truncated array [15] (Figure 4.1c, first column), it can be observed that the radiation pattern of the probe antenna is less distorted by the UAV (Figure 4.1c, second, third, and fourth columns). However, the co-polarization sidelobe shape is more strongly affected by the ripple effect than near boresight. The higher directivity of this array antenna also shows evidence of less perturbations in the cross-polarization levels, as observed in every cut. For field measurement purposes, this is ideal because the array probe presents a relatively constant amplitude near boresight, and low cross-polarization levels (below  $-45$  dB) as desired. Moreover, the size and weight of the probe allows it to be mounted on a gimbal without having a backlash on the payload of the UAV. Figure 4.2c also shows less currents induced on the surface of the UAV and the gimbal body, which may

explain the better radiation characteristics of this type of probe antenna for UAV applications.

The V-pol E-plane co-polarization pattern (Figure 4.3c), much like in H-pol H-plane, is slightly asymmetrical compared to the free space radiation pattern. This is effect is less apparent in H-pol E-plane and V-pol H-plane. Aside from that, the cross-polarization levels exhibit similar behavior as with the previous two cases (dipole and patch).

#### 4.1.4 Horn

The single-polarized horn antenna [15] model used here resembles those commercially available for RF measurement applications. A caveat here is that this particular scenario has limited applicability in a practical situation due to the weight and size of the antenna. For example, the use of a S-band horn limits the UAV payload, and it is also difficult to balance the center of gravity of the horn on the gimbal. Nevertheless, if the horn is low-profile and lighter (e.g., 3D-printed horn antenna) then it becomes feasible for implementation. Referring to Figure 4.1d, the UAV-mounted horn shows very good radiation characteristics in terms of the ripples in the main lobe, and its cross-polarization levels are virtually unaffected in every plane. Additionally, the surface currents induced on the UAV are the smallest out of the four presented cases, albeit having a slightly wider beamwidth than the array antenna. It can be hypothesized that, in addition to the more directive radiation pattern, the flaring in the horn may provide better shielding from scattering off of the UAV, thus presenting less contamination.

V-pol radiation patterns (Figure 4.3d), like in H-pol, show little contamination due to the UAV. The most noticeable change between V-pol and H-pol for the horn is apparent in the surface currents; the gimbal is virtually not inducing any surface currents in V-pol but the lower parts of the frame is, while the opposite occurs in

H-pol. Nevertheless, the radiation characteristics for the UAV-mounted horn are optimal of all four studied cases.

## 4.2 Performance Analysis

In the context of antennas for polarimetric weather radar applications, two of the most important requirements are the matching between the co-polarization radiation patterns of the horizontally and vertically polarized (H-, and V-pol, hereafter) channels, and the cross-polarization levels in both H-pol and V-pol. However, it is no trivial task to evaluate the performance of a probe antenna mounted on a UAV, as the effects of their interaction can be difficult to predict. To facilitate this, analysis metrics that highlight certain aspects of these effects are used in this study, which include co-polarization mismatch, ripples in H- and V-pol, maximum cross-polarization level, and the ratio between the cross-polarized energy of the UAV-mounted antenna and in free-space; they are described next.

### 4.2.1 Description of Metrics

#### 4.2.1.1 Co-polarization Mismatch

The co-polarization mismatch between the H- and V-channels as a function of the direction is derived as:

$$M_{HV}(\theta, \phi) = F_H^{\text{co}}(\theta, \phi) - F_V^{\text{co}}(\theta, \phi) \quad (4.1)$$

expressed in dB<sup>1</sup>, where  $F_H^{\text{co}}$  is the co-polarized H-pol radiation pattern,  $F_V^{\text{co}}$  is the co-polarized V-pol radiation pattern in their corresponding planes of polarization given by  $\phi$ , respectively.<sup>2</sup> While equation (4.1) generalizes the co-polarization mismatch for

---

<sup>1</sup>Uppercase variable notation will generally be used to denote variables in dB, while lowercase will be used for linear units.

<sup>2</sup>The coordinate system is usually defined in Ludwig-3 [68]

all directions, the most important one for these analyses is in the scanning angle or boresight direction, which will be denoted by as  $\theta_0$  (e.g.,  $M_{\text{HV}}(\theta_0, \phi)$ ).

Additionally, it is assumed that during an actual in-situ measurement operation, the beam of the probe antenna will remain relatively aligned with the desired direction; thus, a region of interest can be defined to simplify the analysis. Here, the region within the 3-dB beamwidth  $\theta_3$  will be used to analyze the performance of the metrics under study. In other words, the range of  $\theta$  values for the analyses will usually be assumed to be

$$\theta_0 - \frac{\theta_3}{2} \leq \theta \leq \theta_0 + \frac{\theta_3}{2} \quad (4.2)$$

unless otherwise specified.

#### 4.2.1.2 Ripples

To calculate the ripple level due to coupling and scattering off of the UAV structure for each polarization channel, the mounted probe's radiation pattern needs to be compared to a comparable reference. For this, the pattern of the probe in free space is subtracted from the composite probe-and-UAV pattern as:

$$\Delta_x(\theta) = F_{x,u}^{\text{co}}(\theta, \phi)|_{\phi=\phi_0} - F_{x,a}^{\text{co}}(\theta, \phi)|_{\phi=\phi_0}, \quad (4.3)$$

where  $x$  can be H or V depending on the polarization and  $\phi_0$  is the desired cut.<sup>3</sup> From equation (4.3), the standard deviation (for logarithmic variables) is calculated across  $\theta$ , denoted by the  $\sigma[\cdot]$  operator; e.g.,  $\sigma[\Delta_{\text{H}}]$ , where the angular dependency has been ignored for simplicity.

This metric measures the variability in the H-pol and V-pol co-polarization radiation patterns added by undesired reflections from the UAV within the angular range

---

<sup>3</sup>The subscripts a and u will be used throughout the text to refer to the radiation pattern of the antenna without and with the UAV structure, respectively, where needed.

of interest. The principal planes (cuts) of polarization, E, D, and H will be studied here, which correspond to  $\phi_0$  values of  $0^\circ$ ,  $45^\circ$ , and  $90^\circ$ , respectively.

A similar definition can be made for the cross-polarization ripples, although owing to its somewhat unpredictable nature and very low levels (i.e., less than  $-30$  dB), an extremely high precision for the relative error in the simulations (and in measurements) would be required and thus not included in the analysis.

#### 4.2.1.3 Cross-polarization Metrics

For weather radar applications, one of the two key aspects is achieving a very low cross-polarization level. Cross-polarization radiation is predominantly affected by scattering and depolarizing mechanics due to the presence of the UAV. It is inherently difficult to quantify such effects, however, the maximum cross-polarization level and the ratio of the cross-polarized energy (between UAV-mounted and free-space probe cases) can provide a means to quantify them.

The maximum in the cross-polarization radiation pattern is normalized with respect to the co-polarization boresight as:

$$\text{MXL} = \max_{\theta} F_x^{\text{cx}}(\theta, \phi)|_{\phi=\phi_0} - F_x^{\text{co}}(\theta_0, \phi)|_{\phi=\phi_0}, \quad (4.4)$$

where the local maximum is computed for the range of interest  $\theta$  and for the given  $\phi_0$  cut.

The ratio of the cross-polarized energy that is scattered in the region of interest by the probe antenna with the UAV with respect to free space (XER) is calculated as:

$$\text{XER} = 10 \log_{10} \left( \frac{\int |f_{x,u}^{\text{cx}}(\theta, \phi)|^2 d\theta|_{\phi=\phi_0}}{\int |f_{x,a}^{\text{cx}}(\theta, \phi)|^2 d\theta|_{\phi=\phi_0}} \right), \quad (4.5)$$

and it represents the increase in cross-polarization energy of the probe antenna when in presence of the UAV, for the  $\theta$  range of interest.

## 4.2.2 Analysis

In this section, a performance analysis will be provided based on the radiation characteristics presented in Section 4.1 and the metrics [equation (4.1)-equation (4.5)] previously discussed. For the sake of brevity, the analysis will focus on the E-plane radiation patterns, although similar analysis can be made in any other cut of interest.

### 4.2.2.1 Dipole

The dipole radiation patterns in E-plane is a particular case due to the broad radiation characteristics that presents. The region where the radiated power is greater than 3-dB consists of a front lobe and a back lobe. As a result of this, it can be predicted that the fields scattered from the structure will have a stronger impact both in the co- and cross-polarization radiation patterns, as previously discussed. The region of interest in this case becomes anywhere where the radiated power is greater than 3 dB, and plots corresponding to the metrics of interest are shown in Figure 4.4. The co-polarization mismatch for the dipole is shown in Figure 4.4a, with the boresight values (marked) of  $-0.01$  dB and  $-2.59$  dB for the probe in free space and on the UAV, respectively. Outside of boresight, these values change rapidly on the UAV, so ideally it should be required that the probe orientation relative to the nose of the UAV be very small (or known and constant) such that appropriate corrections can be applied. Nevertheless, the standard deviation of the mismatch in this range is 0.006 dB in free space and 2.628 dB on the UAV, which does not meet the 0.1 dB requirement for weather radar applications.

By subtracting the free-space radiation pattern from the UAV-mounted pattern, it is possible to visualize the net effect of adding the UAV into the testing environment. The ripples in the co-polarization patterns added due to the presence of the UAV with respect to the free space pattern is plotted in Figure 4.4b for the H- (red) and V-pol (blue) cases. Obviously, the effect of the ripples is to add uncertainties in

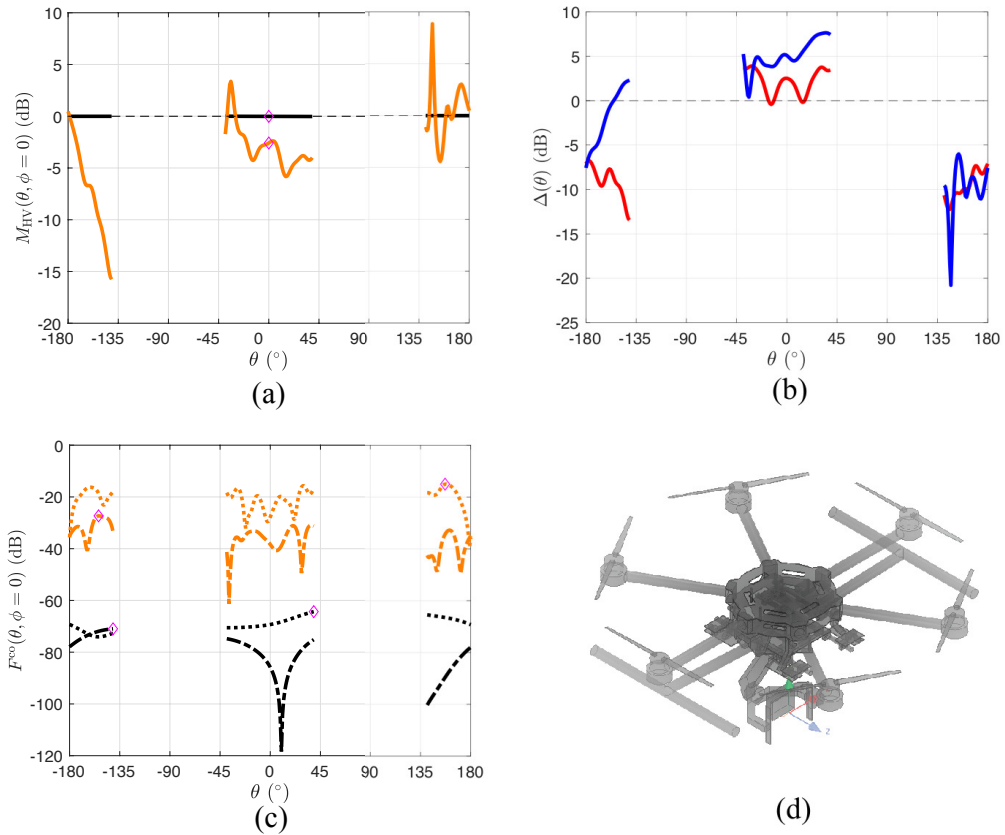


Figure 4.4: Performance of the simulated dipole in terms of: (a) co-polarization mismatch for free space (black) and mounted on the UAV (orange), (b) H- (red) and V-pol (blue) ripples in co-polarization pattern, (c) cross-polarization patterns of free space (black) and mounted on UAV (orange) for H- (dotted) and V-pol (dash-dotted), and (d) model of the UAV and dipole.

the mismatch between the co-polarization patterns. The standard deviation for the mismatch in H-pol is 3.51 dB and in 4.64 dB in V-pol. This illustrates the fact that a dipole used as a probe for UAV-based antenna measurements would be less than ideal for this application.

The cross-polarization patterns for the free space and UAV cases are shown in Figure 4.4c, where the maximum of each is marked. The maximum levels in free space are found to be  $-64.33$  dB and  $-70.98$  for the H- and V-pol, respectively, whereas on the UAV they increase to  $-15.06$  dB and  $-27.31$  dB. This yields an increase of approximately 50 dB in H-pol and 44 dB in V-pol, which is quite significant. As an additional measure, using equation (4.5) the ratio of the cross-polarized energy radiated with the UAV with respect to free space is found to be 51.53 dB for H-pol and 48.44 dB for V-pol.<sup>4</sup>

#### 4.2.2.2 Patch

A similar analysis is done for the patch antenna, which exhibits a more directive radiation pattern than the dipole, with a 3-dB beamwidth of approximately  $90^\circ$ . Figure 4.5 shows the metrics for the patch antenna. It can be predicted that, with the back lobe radiation being weaker for this case, the contamination from the UAV structure would be smaller.

The co-polarization mismatch (Figure 4.5a) shows boresight values of  $-0.01$  dB and  $0.07$  dB for the probe in free space and on the UAV, respectively. The variability of the mismatch is smaller, with the standard deviation being  $0.008$  dB in free space and  $0.878$  dB on the UAV. The radiation characteristics show an improvement of about 2 dB on the UAV when compared to the dipole case, though still above the desired level. The ripples in the co-polarization patterns are plotted in Figure 4.5b for H- (red) and V-pol (blue). The standard deviation for the mismatch in H-pol is

---

<sup>4</sup>In other words, the cross-polarization power is approximately 100,000 times higher when mounted on the UAV!

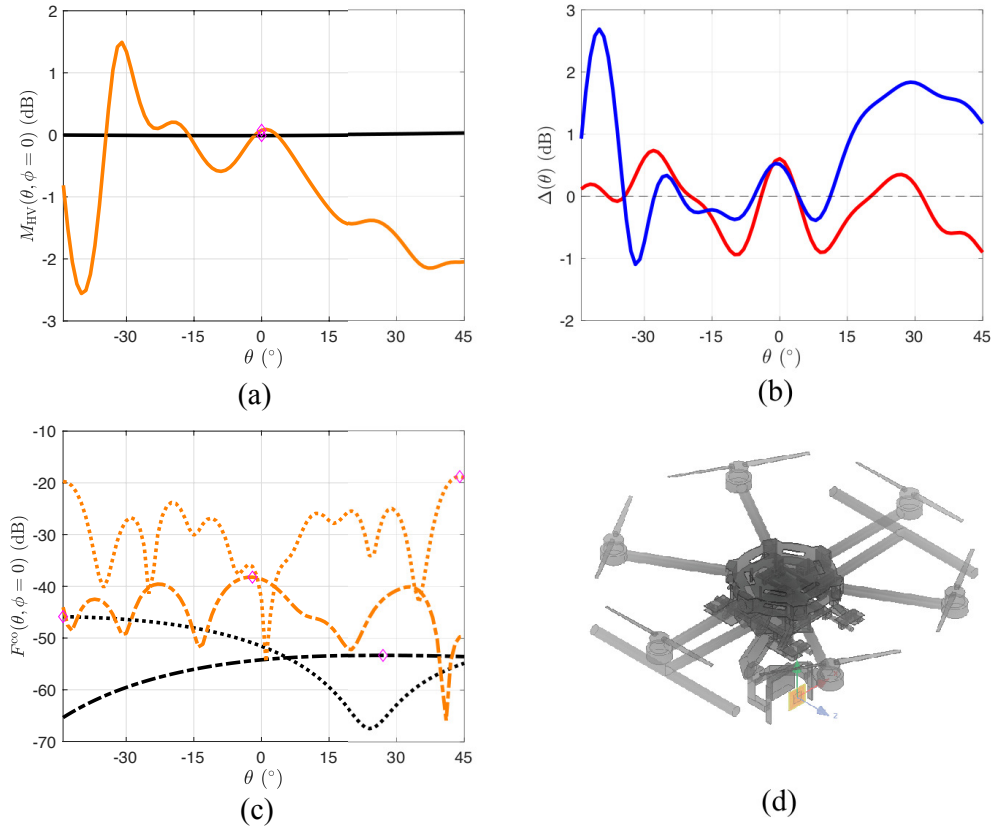


Figure 4.5: Performance of the simulated patch in terms of: (a) co-polarization mismatch for free space (black) and mounted on the UAV (orange), (b) H- (red) and V-pol (blue) ripples in co-polarization pattern, (c) cross-polarization patterns of free space (black) and mounted on UAV (orange) for H- (dotted) and V-pol (dash-dotted), and (d) model of the UAV and patch.

0.45 dB and 0.97 dB in V-pol. The patch antenna exhibits less ripples in the main beam in both H- and V-pol cases, and a better performance overall than the dipole.

The maximum levels in the cross-polarization patterns (Figure 4.5c) in free space are found to be  $-45.86$  dB and  $-53.32$  for the H- and V-pol, respectively, whereas on the UAV they increase to  $-18.83$  dB and  $-38.23$  dB; yielding an increase of approximately 27 dB in H-pol and 15 dB in V-pol, showing an improvement over the dipole case. The ratio of the cross-polarized energy radiated with the UAV with respect to free space is 23.99 dB for H-pol and 12.73 dB for V-pol.

#### 4.2.2.3 Array

The array design used in this study has a 3-dB beamwidth of approximately  $28^\circ$ , as shown in Figure 4.1c for H-pol and Figure 4.3c for V-pol. An improvement in the metrics with respect to the previous cases is immediately apparent; although, it should be noted that a narrower beamwidth probe antenna is more vulnerable to errors due to stability of the UAV and relative alignment between the probe and the UAV. The mismatch at boresight is shown in Figure 4.6a to be  $-0.03$  dB in free space and  $-0.15$  dB on the UAV, with a standard deviation of 0.01 dB and 0.13 dB respectively, which approximately meets the requirement of 0.1 dB. Such performance can be improved if the variation of the relative alignment between the UAV and the probe is maintained very small (i.e., within a few degrees off boresight).

The amplitude of the ripples in both polarizations (Figure 4.6b) is also notably smaller than in the previous cases, showing how an array probe would be less vulnerable to variations in co-polarization mismatch due to probe-UAV misalignment. The standard deviation of the ripples are 0.14 dB in H-pol and 0.08 dB in V-pol.

Figure 4.6c shows the maximum cross-polarization levels in free space to be  $-59.17$  dB and  $-59.76$  dB for H- and V-pol, respectively; and, analogously  $-37.29$  dB and  $-46.26$  dB on the UAV, for a total increase of approximately 22 dB in the H-pol and 14

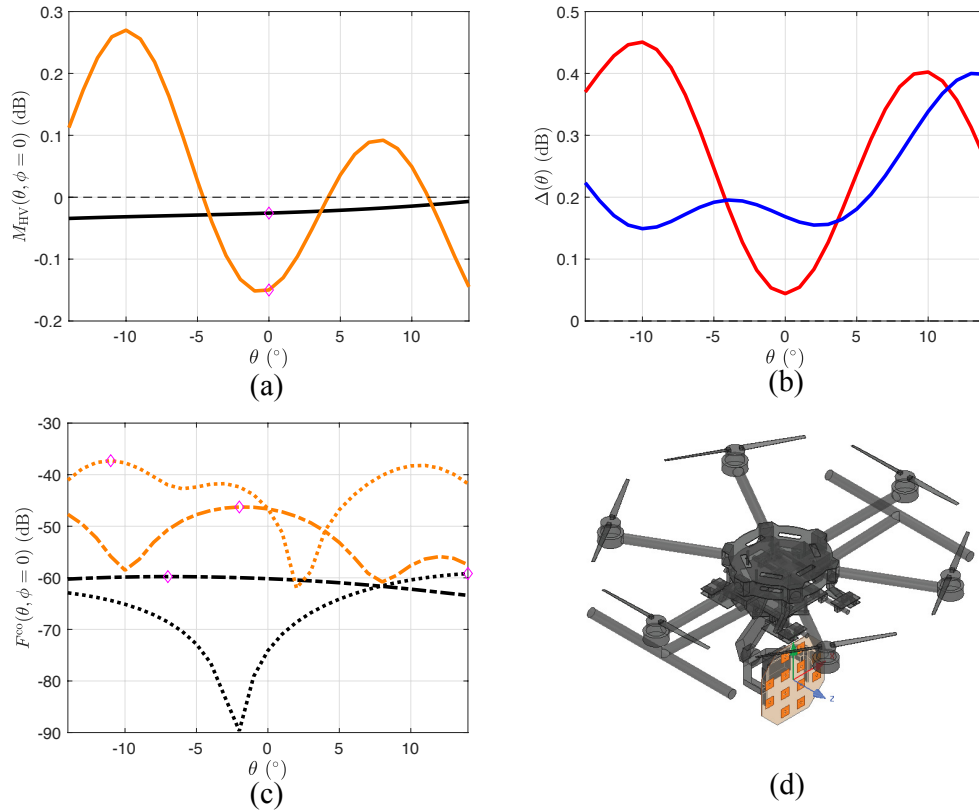


Figure 4.6: Performance of the simulated 4x4 patch array in terms of: (a) co-polarization mismatch for free space (black) and mounted on the UAV (orange), (b) H- (red) and V-pol (blue) ripples in co-polarization pattern, (c) cross-polarization patterns of free space (black) and mounted on UAV (orange) for H- (dotted) and V-pol (dash-dotted), and (d) model of the UAV and patch array.

dB in the V-pol cross-polarization levels. As previously mentioned, this performance can be improved by constraining the relative alignment between the probe and UAV to within a few degrees from boresight. While the ability to measure normalized cross-polarization levels down to  $-50$  dB is sought after ideally,  $-35$  to  $-40$  dB is usually sufficient for the application. The XER in the H-pol is 23.19 dB and 10.47 dB in V-pol.

#### 4.2.2.4 Horn

The horn analyzed here presents a special case because the radiation pattern shows a 3-dB beamwidth of approximately  $41^\circ$  which is wider than the array, and also shows a slightly higher back lobe radiation than the array. Nevertheless, the metrics show a comparable or even better performance than the array in some cases. It is hypothesized that the flaring of the horn antenna allows a degree of shielding from the backscattered radiation off of the UAV structure, and thus, the mismatch, ripples, and cross-polarization levels have better performances overall. Figure 4.7a shows the co-polarization mismatch for the horn in free space and with the UAV, with the values in boresight of  $-0.02$  dB and  $0.05$  dB respectively; and the standard deviations are calculated as  $0.03$  dB and  $0.05$  dB.

The ripples in H- and V-pol for the horn are the smallest yet, with standard deviations of the amplitudes of  $0.03$  dB and  $0.05$  dB respectively, showing the best performance over a wider range of angles.

Although in free space, the maximum cross-polarization levels of the horn radiation patterns in H- and V-pol are not lower than the array's, at  $-44.91$  dB for H-pol and  $-48.91$  dB for V-pol, when mounted on the UAV, these levels remain virtually the same. On the UAV, the maximum levels are found to be  $-46.34$  dB for H-pol and  $-48.22$  dB for V-pol, with a relative difference of approximately  $1.4$  dB and  $0.07$  dB respectively. The XER for the H-pol case yields  $-4.52$  dB for H-pol and  $-5.07$  dB

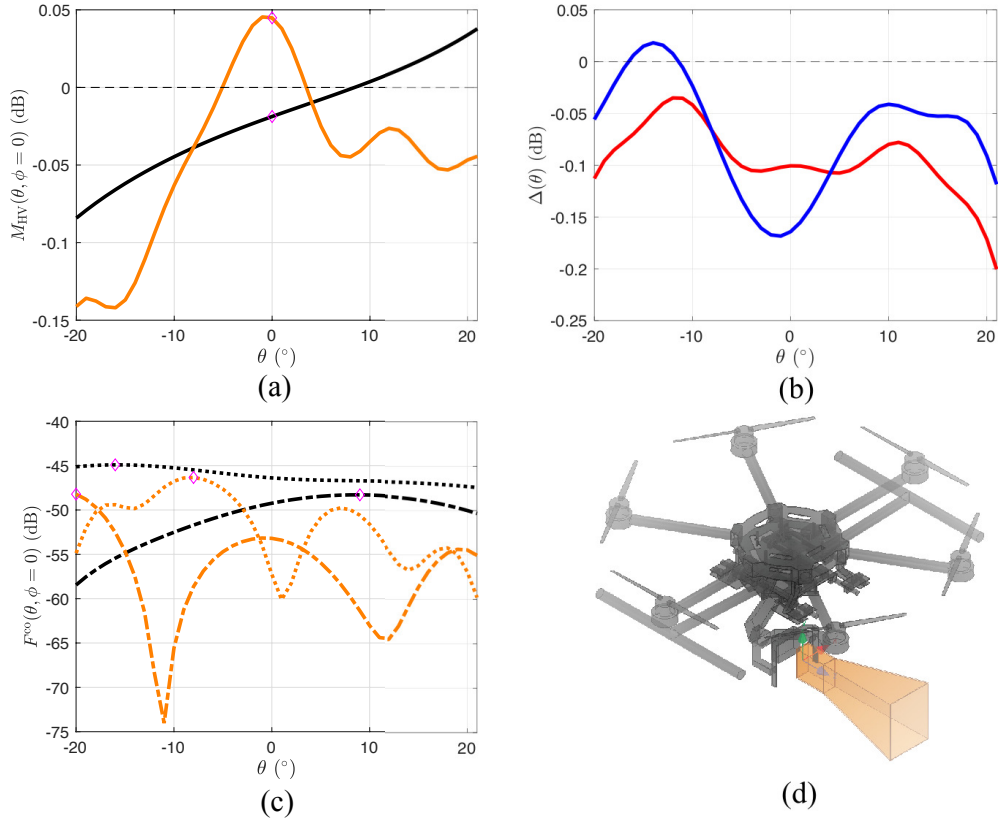


Figure 4.7: Performance of the simulated horn in terms of: (a) co-polarization mismatch for free space (black) and mounted on the UAV (orange), (b) H- (red) and V-pol (blue) ripples in co-polarization pattern, (c) cross-polarization patterns of free space (black) and mounted on UAV (orange) for H- (dotted) and V-pol (dash-dotted), and (d) model of the UAV and horn.

for V-pol, indicating that the cross-polarization energy being radiated is the smallest for the horn than the rest of the cases.

### 4.2.3 Probe Selection

The best probe antenna for the application should ideally meet the RF performance criteria while being able to sustain flight endurance long enough to complete an operation uninterrupted. Typical values for the weights of the studied antennas and the UAV endurance with the antennas mounted on are presented in Table 4.1, based on the platform that has been used for testing [35]. Additionally, the metrics that are most relevant to the RF performance of the probe and UAV set are listed in Table 4.1 for each case in the E-plane.

Table 4.1: Summary of relevant performance metrics.

	Dipole	Patch	Array	Horn
Weight (kg)	< 0.1	0.2	0.9	3.0
Endurance (min)	30	29	25	18
$\sigma[M_{\text{HV,u}}]$ (dB)	2.63	0.88	0.13	0.05
$\sigma[\Delta_{\text{H}}]$ (dB)	3.51	0.45	0.14	0.03
$\sigma[\Delta_{\text{V}}]$ (dB)	4.63	0.97	0.08	0.05
$\text{MXL}_{\text{H,u}}$ (dB)	-15.06	-18.83	-37.29	-46.34
$\text{MXL}_{\text{V,u}}$ (dB)	-27.31	-38.23	-46.26	-48.22
$\text{XER}_{\text{H}}$ (dB)	51.53	23.99	23.19	-4.52
$\text{XER}_{\text{V}}$ (dB)	48.44	12.73	10.57	-5.07

The endurance is directly related to flight performance, i.e., longer endurance is better, and the factors that affect it are the takeoff and payload weight, payload placement within the UAV frame, the flight strategy to be conducted, etc. The co-polarization mismatch is inherently related to the radiation characteristics for each polarization channel (H or V), and is additionally affected by the ripples in the respective channel. Ideally, the mismatch should be zero; thus, lower mismatch and

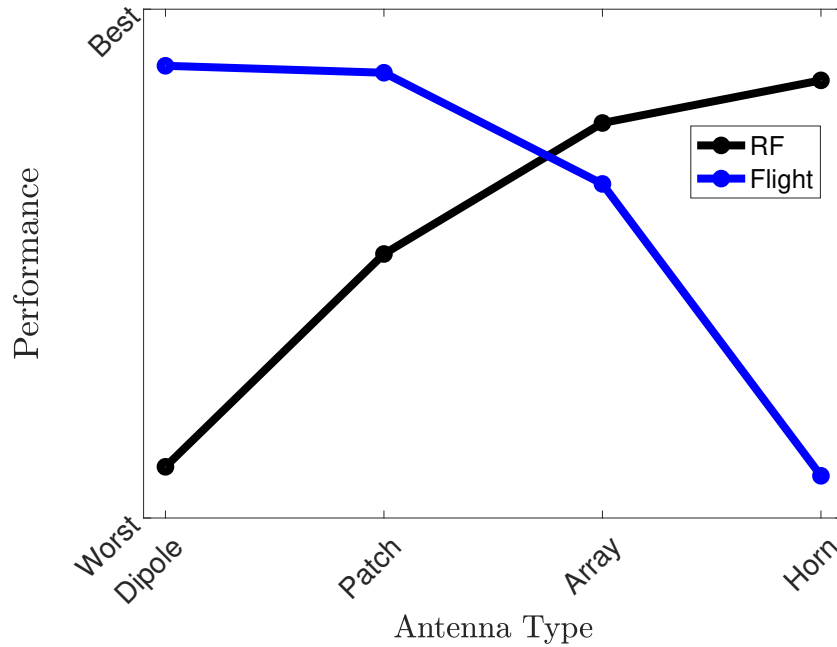


Figure 4.8: Qualitative flight and RF performances for different antenna types.

ripples result in better RF measurement performance. On the other hand, the energy radiated in the cross-polarization should ideally be zero or smaller (in dB) producing less distortion in the cross-polarization patterns when mounted on the UAV; i.e., less is better. As such, a maximum cross-polarization level of approximately  $-50$  or better is sought after ideally.

Based on Table 4.1 and by assigning weights to these parameters, it is possible to qualitatively determine their performance according to the best and worst cases between the four antenna types analyzed. Such depiction is shown in Figure 4.8, where the RF performance (black) is overlaid with the flight performance (blue). This representation shows the trade-off between the UAV endurance and payload versus the desired RF measurement performance criteria. The analysis presented in this section shows the dipole and horn having the worst and best RF performance respectively, while simultaneously having the best and worst flight performance. There is a marginal improvement in going from an array to a horn in terms of RF performance, while the loss in flight performance is quite significant. Similarly, while there

is a slight improvement in endurance going from an array to a patch, the loss in RF performance is such that the minimum requirements are harder to achieve. Therefore, the array is selected as the probe antenna to be mounted on the UAV, since it has the best performance overall, when RF and flight performances are taken into account.

## 4.3 Measurements

In this section, indoor characterization of the array antenna mounted on the UAV is presented, and the variability of the radiation patterns due to the relative alignment of the probe and the UAV frame is also studied. The measurements were performed at the University of Oklahoma's Advanced Radar Research Center (ARRC) facilities (Figure 4.9).

### 4.3.1 Follow Mode

When the UAV is hovering about a point in space while the AUT is being measured, it is desirable that the probe antenna has no relative orientation difference with respect to the nose of the UAV to keep the variance in measurement to a minimum. In the gimbal's follow operating mode, the probe antenna follows the nose of the UAV and there is no relative movement between the UAV and the probe antenna, which is similar to the configurations used in the simulations from previous sections.

To validate the simulations of Section 4.1.3, indoor measurements of the array antenna in free space and mounted on the UAV are taken in H- and V-polarizations, for E- and H-planes (Figure 4.10).

For the most part, the simulations and measurements are in good agreement, with inherent discrepancies that can be attributed to the uncertainty in the measurement process, as well as tolerances and faults in the fabrication process. More importantly, the distortion in the radiation patterns due to the presence of the UAV is congruent,

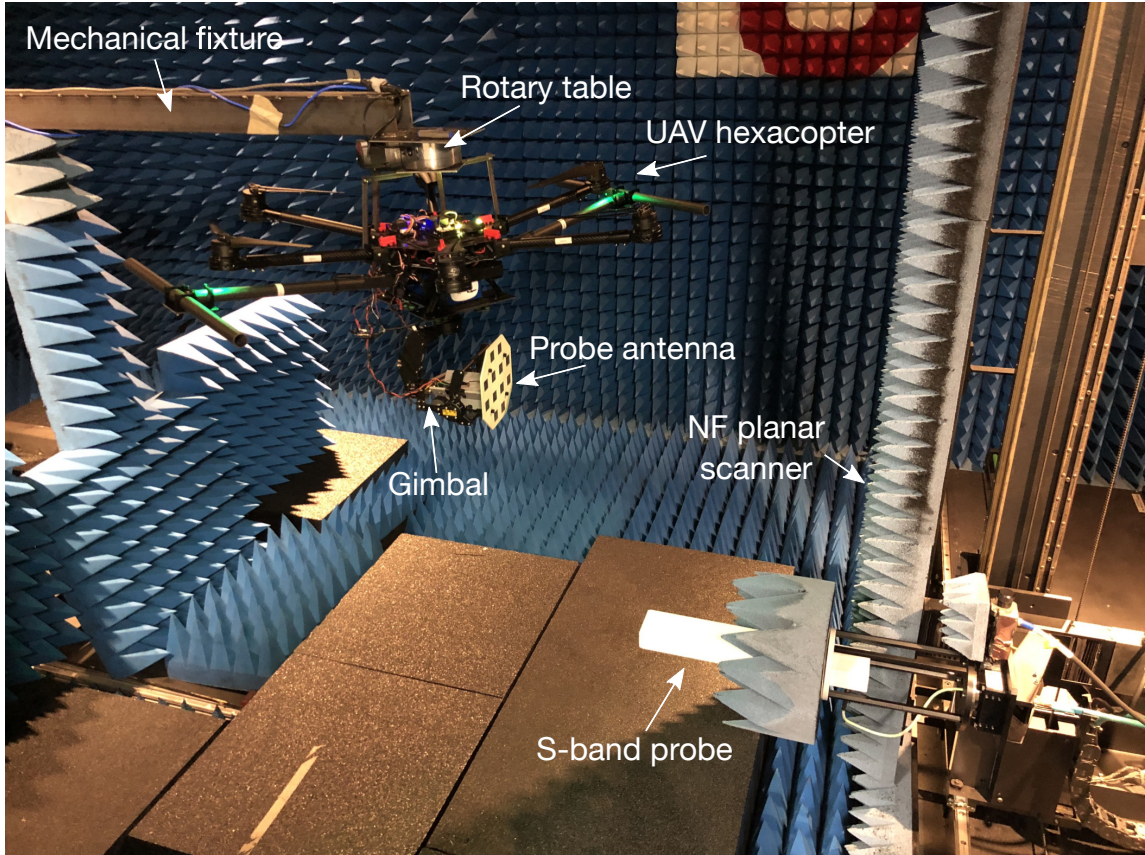


Figure 4.9: Measurement setup in planar near-field anechoic chamber: UAV with landing gear in engaged position with probe antenna (4x4 patch array) mounted on gimbal. The measurements were performed in the NF (pictured above) and FF anechoic chamber facilities of the University of Oklahoma’s (OU) Advanced Radar Research Center (ARRC).

as it is noticeable in the V-pol E-plane, and in the H-planes for both polarizations. On the other hand, the increase in the cross-polarization level is also apparent in the measurements, albeit a couple of dB higher than in the simulations.

The metrics calculated for the measurements are shown in Figure 4.11. From Figure 4.11a and b, the effect of the ripples due to the UAV frame is evident, as it was in the simulations. The mismatch at boresight (Figure 4.11a) is measured at 0.04 dB for free space and  $-0.05$  dB on the UAV, which meets the requirement of 0.1 dB. The standard deviation for the mismatch in the 3-dB beamwidth range is 0.20 dB in free space and 0.43 dB on the UAV, which can be improved as long as the gimbal and the UAV are stable enough within a few degrees off boresight when pointing towards

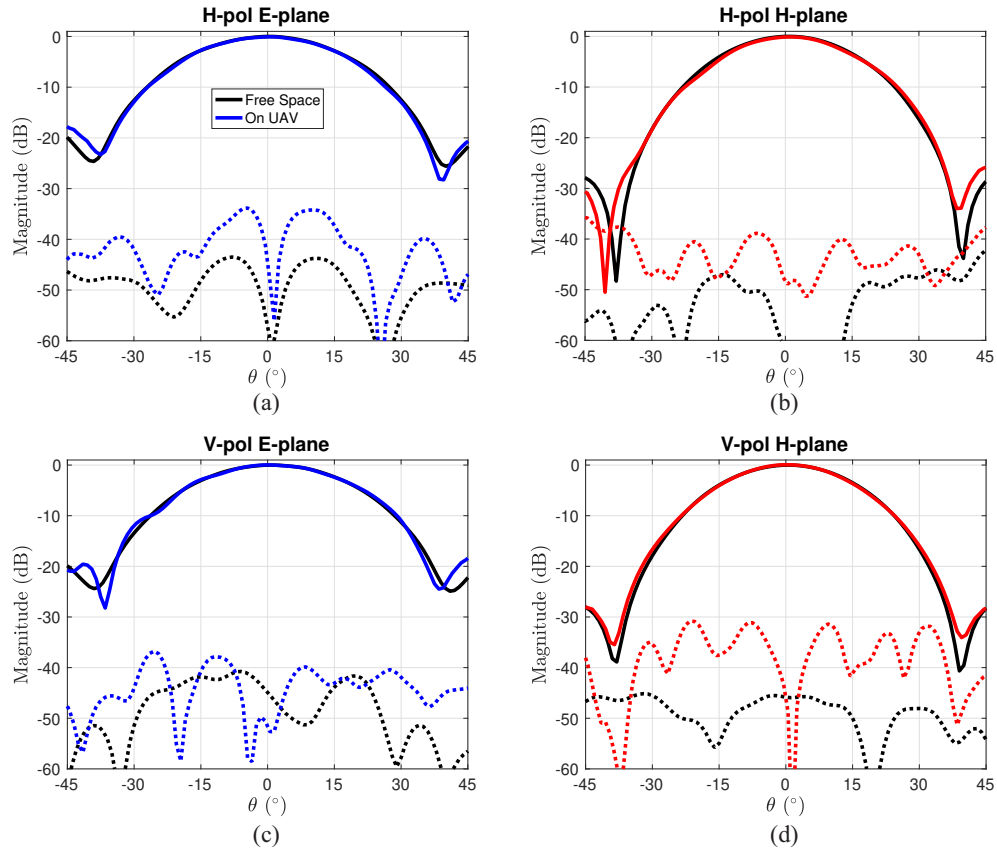


Figure 4.10: Normalized measured antenna radiation patterns of the truncated 4x4 patch array antenna used as a probe in free space (black) and mounted on the UAV (blue/red) for: (a) H-pol, E-plane, (b) H-pol, H-plane, (c) V-pol, E-plane, and (d) V-pol, H-plane.

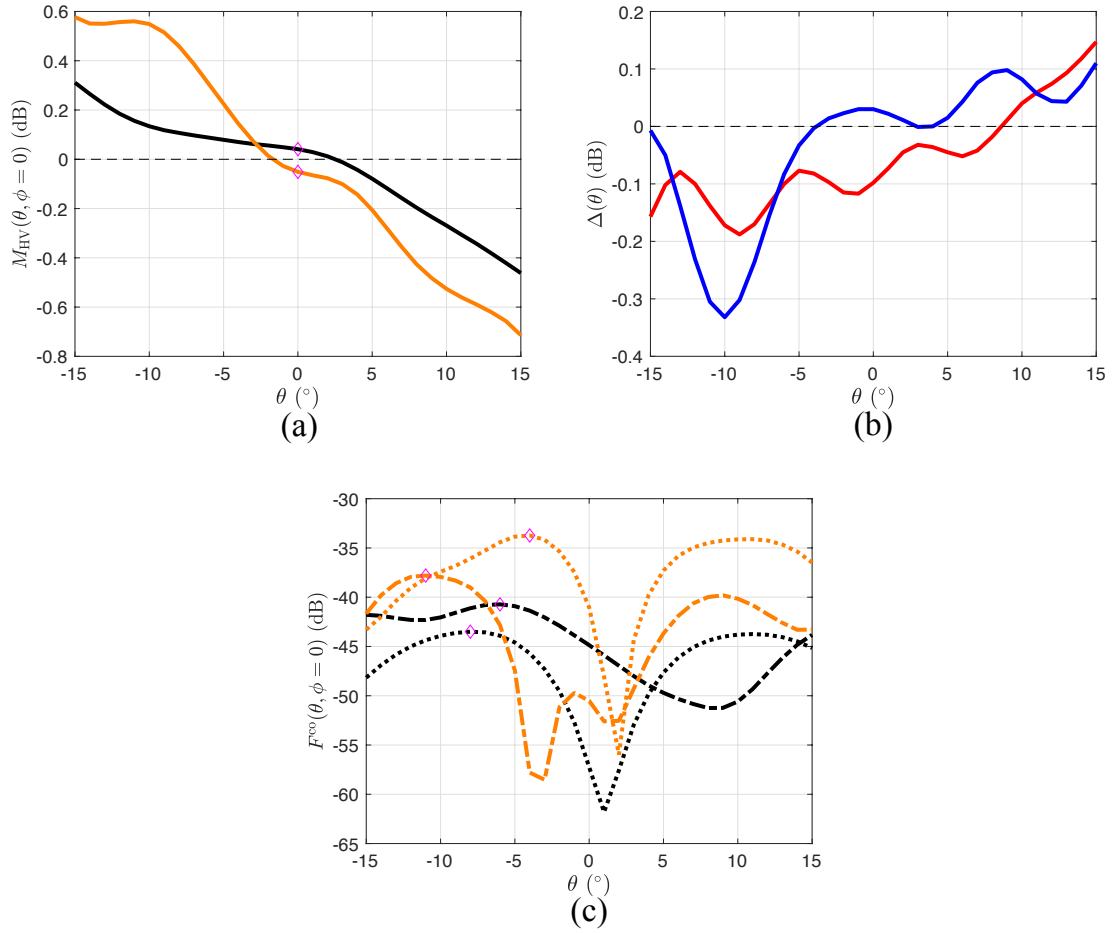


Figure 4.11: Performance of the measured array in terms of: (a) co-polarization mismatch for free space (black) and mounted on the UAV (orange), (b) H- (red) and V-pol (blue) ripples in co-polarization pattern, and (c) cross-polarization patterns of free space (black) and mounted on UAV (orange) for H- (dotted) and V-pol (dash-dotted). The gimbal orientation angles are  $\alpha_r, \alpha_p, \alpha_y = 0^\circ$  relative to the UAV frame.

the AUT. The H- and V-pol ripples (Figure 4.11b) are measured with a standard deviation of 0.08 dB and 0.12 dB respectively.

The maximum cross-polarization levels (Figure 4.11c) in H-pol are measured at  $-43.50$  dB and  $-33.74$  dB in free space and on the UAV, respectively; while in V-pol, they are  $-40.72$  dB and  $-37.80$  dB. From these numbers, the increase in the cross-polarization level due to the presence of the UAV is approximately 10 dB in H-pol and 3 dB in V-pol. Although the cross-polarization measurements are expected to be higher than the simulations, the higher increase in H-pol than in V-pol is in agreement with the simulations. Additionally, the maxima in the cross-polarization levels are located far from boresight, so the performance can be increased if the range of operation is limited, as discussed previously.

### 4.3.2 Tracking Mode

When the flight strategy is not hovering mode, the use of a gimbal adds additional degrees of freedom for the probe antenna to be aligned with the phase center of the AUT. For this study, only the yaw angle of the gimbal is varied and characterized indoors; however, it should be noted that the roll and pitch angles may vary as well, and as such, it is desired to keep them stable about zero degrees to avoid displacement of boresight and measurement planes.

The probe antenna is then characterized in chamber (Figure 4.12) by maintaining the gimbal and probe antenna aligned while varying the yaw angle of the UAV frame between  $-15^\circ$  and  $15^\circ$ .<sup>5</sup>

At the angles of  $\pm 10^\circ$  and  $\pm 15^\circ$ , the mismatch and cross-polarization levels vary significantly from those at  $0^\circ$  gimbal yaw, while between  $-5^\circ$  and  $5^\circ$  the variance is tolerable. This supports the idea that by limiting the operating range of gimbal yaw

---

<sup>5</sup>This set of measurements is different from the ones in the previous section, and due to alignment and other factors, the V-pol pattern is somewhat different at a gimbal yaw angle of zero, though other characteristics remain unchanged.

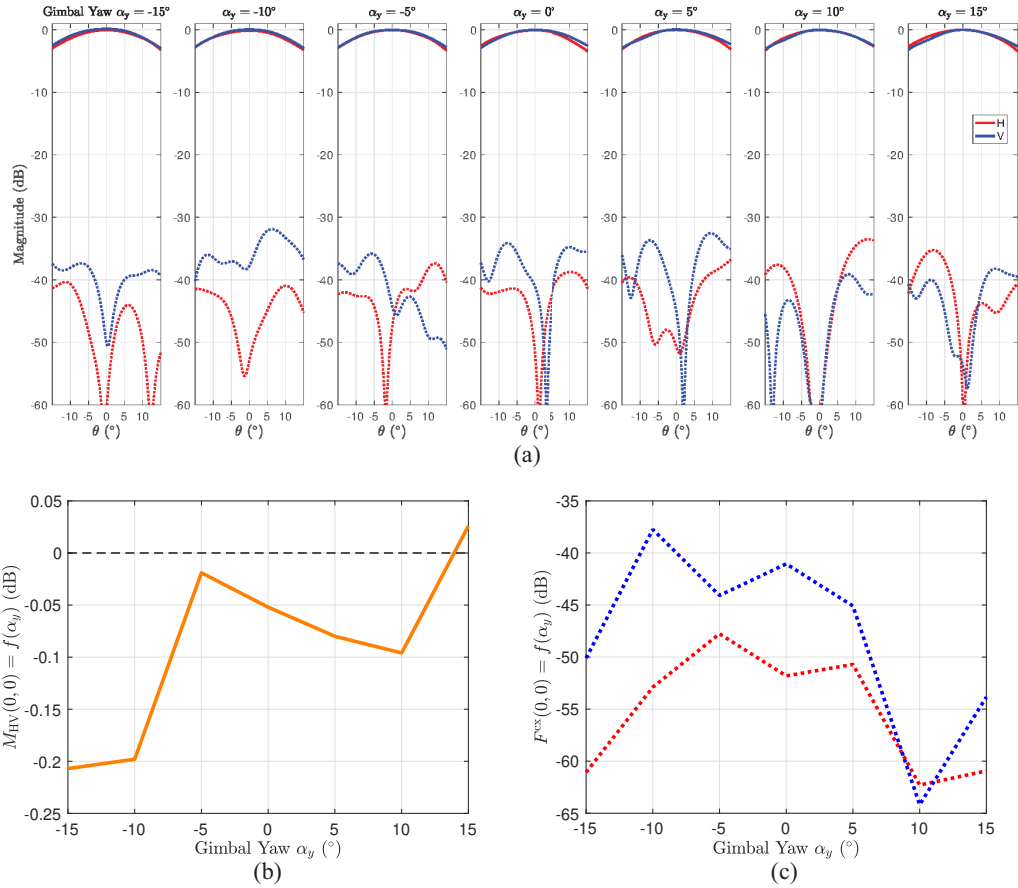


Figure 4.12: Radiation characteristics of the probe antenna mounted on the UAV and gimbal: (a) radiation patterns in co- (solid) and cross-polarization (dashed), for H- (red) and V-pol (blue), for different gimbal yaw angles relative to the nose of the UAV, (b) mismatch at boresight ( $0^\circ$  for each pattern in (a)) between H- and V-pol, and (c) cross-polarization levels at boresight (same as (b)) for H- (red) and V-pol (blue).

angles, the effects of the UAV on the radiation characteristics of the probe antenna can be mitigated to some extent, and also provides an insight on how the probe antenna behaves as a function of its orientation relative to the UAV frame.

## 4.4 Summary

In the selection of an optimal probe antenna for polarimetric weather radar characterization using UAVs, some factors have to be considered. One of the most important one is the degradation of the radiation characteristics of the probe antenna due to being in proximity of the UAV frame. Different types of antennas will present different behavior due to their inherent radiation characteristics, and therefore the scattering from the UAV will be different; thus, it is important to understand this behavior such that the probe antenna can be adequately selected. It is emphasized that this application imposes strict requirements in terms of co-polarization mismatch levels and maximum cross-polarization levels, in the order of 0.1 dB and approximately  $-45$  dB, respectively. These restrictions may be relaxed depending on the operational mode, but it is the standard that guarantees low biases in the polarimetric weather radar products.

The effects of scattering due to the proximity of the UAV frame to the probe antenna have been investigated in this work through simulations and validated with measurements in the appropriate scenarios. The simulated radiation patterns have shown the effect of the ripples being added on the co-polarization radiation patterns and an increase in the cross-polarization levels. According to the metrics presented in Section 4.2, the dipole has shown the worst RF performance, and the horn the best performance. Conversely, the horn has shown the worst flight performance, whereas the dipole is the lightest of antenna types, thus having the best flight performance. However, when taking into account both RF and flight performances, the array is

found to be the best candidate for this application owing to its light weight, low-profile, and acceptable RF performance. Nevertheless, the horn-type of antennas would be ideally preferred, as the surface current plots show minimal scattering off the UAV frame, and less contamination in the radiation patterns. The downside of a high-precision horn is their weight and the profile which would imbalance the weight distribution on the gimbal and degrade the endurance of the UAV; an alternative that could be further explored is a horn antenna made of light-weight materials that would overcome the limitations.

Additionally, the simulated array case has been validated with anechoic chamber measurements, where the effect of scattering from the UAV has been shown to be in qualitative agreement. The ripples and the increment in the cross-polarization levels have shown a similar behavior both in measurements as in simulations, with an increase in the cross-polarization level of approximately 3 to 10 dB in the UAV with respect to the probe antenna in free space. Furthermore, the variance of the radiation patterns as the yaw angle of the gimbal is varying (i.e., change in the relative alignment between the probe antenna and the UAV nose) has been studied. Based on the results, it is recommended that the range of operation of the gimbal yaw should be limited to within a few degrees off from the nominal zero degree (no misalignment with respect to the UAV) to have an RF performance that is still within the required limits. In this case, the variance is not significant as long as the gimbal is operating within  $-5^\circ$  and  $5^\circ$ . It is important to note that the variance due to the roll and pitch angles have not been included in this study, and it could be a considerable source of error and should not be disregarded.

In summary, the simulations and measurements have shown a good agreement with regards to the effect of scattering due to the proximity and relative orientation of the UAV and the probe antenna; and the EM simulation can be an useful tool to determine the performance of the system before final implementation. The array

antenna studied for this project, as a baseline, is found to be in agreement with the requirements for polarimetric weather radar characterization. Further strategies to improve the quality of the measurements can be based in the design of the antenna itself, or by implementing signal processing techniques either during flight or in post-processing.

## Chapter 5

### System Description and Operations

The guidelines and the feasibility of producing accurate antenna pattern measurements using UAVs from a theoretical standpoint have been presented in Chapter 3, wherein the analysis framework allowed for the selection of test and probe antennas, as well as modeling of the positioning accuracy of the UAV system. In Chapter 4, the interaction of the UAV frame with the probe antenna mounted on the gimbal has been studied, which provides certain criteria to account for in order to achieve the best measurement performance for a given UAV system and probe antenna pairs.

In this chapter, the main topic of discussion will be the selection of an appropriate UAV system, with the end goal of presenting results of the system's performance in an outdoor in-situ measurement scenario. A brief history of the evolution of the platform will be presented, highlighting the shortcomings of each platform and the reasons why a better platform was considered to replace the previous one. The positioning accuracy is studied on the ground, and airborne, with a discussion on potential flight strategies depending on the AUT. Finally, the results of performing in-situ outdoor measurements with the system will be presented as a conclusion to this chapter.

## 5.1 Platform History

Since the proof of concept for this project was introduced in 2015, various challenges have been faced and some valuable lessons learned. The characteristics of each platform and the takeaways will be briefly presented next.

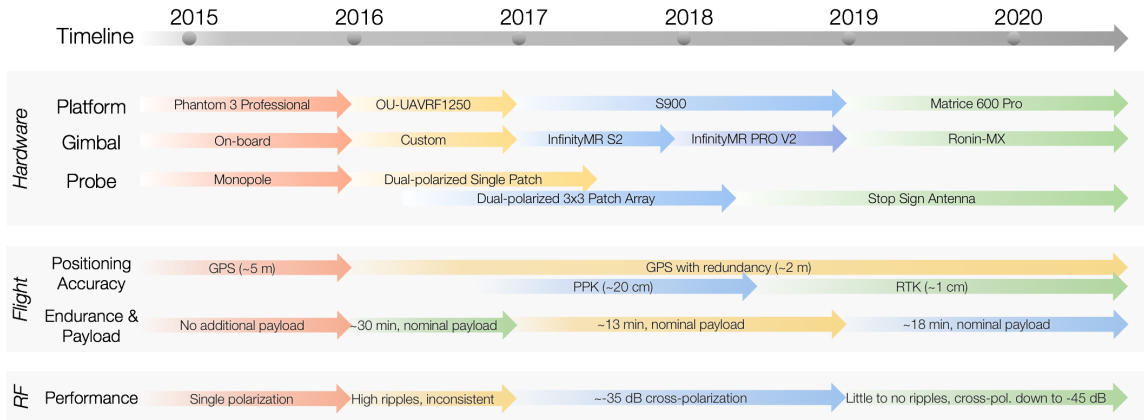


Figure 5.1: Timeline of the changes in the platform in terms of hardware, flight, and RF performance.

### 5.1.1 DJI Phantom 3 Professional (2015-2016)

The DJI Phantom 3 Professional (hereafter, P3P) was the platform of choice for the period of 2015 through 2016, where preliminary studies on the feasibility of antenna measurement, radome inspection, and weather radar calibration have been presented as proof of concept for X-band antennas [31]. The description of the UAV platform will be limited only to those parameters relevant to UAV-based antenna measurements. The P3P is a quadcopter with a weight of 1280 g, with a diagonal size of 350 mm, a maximum flight time of approximately 23 mins, with nominal hover accuracy of  $\pm 0.1$  m (vertical, with vision positioning),  $\pm 0.5$  m (vertical, with GPS positioning), and  $\pm 0.3$  m (horizontal, with vision positioning),  $\pm 1.5$  m (horizontal, with GPS positioning).



Figure 5.2: The DJI Phantom 3 Professional platform.

Among the most important experiments carried out with this platform were the testing done in both indoor and outdoor antenna ranges, and for mobile weather radar calibration studies. The antenna measurements were carried out using an X-band AUT [86], and a small monopole as the probe antenna mounted on the P3P, mainly limited by the fact that the P3P gimbal cannot support payloads other than its own camera. An RF synthesizer was mounted on the UAV to transmit a 20 dBm continuous-wave (CW) signal at 9.8 GHz.

The indoor measurements for this set of tests showed that, in X band, there was minimal interaction between the UAV frame and the probe antenna's radiation pattern, and that the discrepancies between the measurements were mostly due to the flight stability of the UAV itself, even in a windless indoor setting [31]. The outdoor measurements tested the same setup but in an outdoor setting, where extraneous reflections and other environmental factors (e.g., wind gusts, temperature) would be more prevalent. Two flight patterns in particular were of interest: hovering while the AUT is rotating, and a circular flight path around the AUT with the AUT stationary. The comparison between the co-polarization reference antenna pattern and the ones measured in-situ were approximately 2.7-3 dB off in the main beam and side lobe regions [31]. Although the circular flight path showed a more stable radiation

pattern and in better agreement with the reference pattern, it was concluded that the stability, the positioning accuracy, and targeting accuracy (no roll control on the probe antenna) were insufficient to carry out antenna pattern measurements to that met the requirements for weather radar systems. No cross-polarization measurements were conducted during these experiments.

The mobile radar calibration experiment was able to measure the  $Z_{DR}$  of a foil-wrapped foam sphere with a standard deviation of 0.35 dB using the RaXPol X-band mobile radar system [31]. In addition to proposing an in-situ  $Z_{DR}$  calibration method for mobile radars, ground reflection characterization methods were also proposed under the same framework. This led to the understanding of challenges and limitations, as well as the potential of using a UAV system for in-situ characterization of radar systems.

### **5.1.2 OU-UAVRF1250 (2016-2017)**

With the idea of conceiving a multi-band (S, C, and X bands) platform that enables three important radar characterization missions, such as antenna measurements, radome inspection, and radar calibration, a custom-made platform was proposed. The OU-UAVRF1250 octocopter, built with custom parts and open source software, has a weight of approximately 17 kg, a diagonal size of 1250 mm, a maximum flight time between 30 and 45 mins depending on the battery configuration, a payload of 5 kg, and standard GPS positioning accuracy in the order of 3-5 m, which can be improved with the use of DGPS, and a 3-axes custom-made gimbal.

The initial characterization of the performance of the octocopter platform was performed indoors, with S-, and X-band horn antennas as AUTs, while single layer patch antennas were used as probes in the same bands. The objective of this initial testing was to determine if the system met the requirements with respect to gimbal

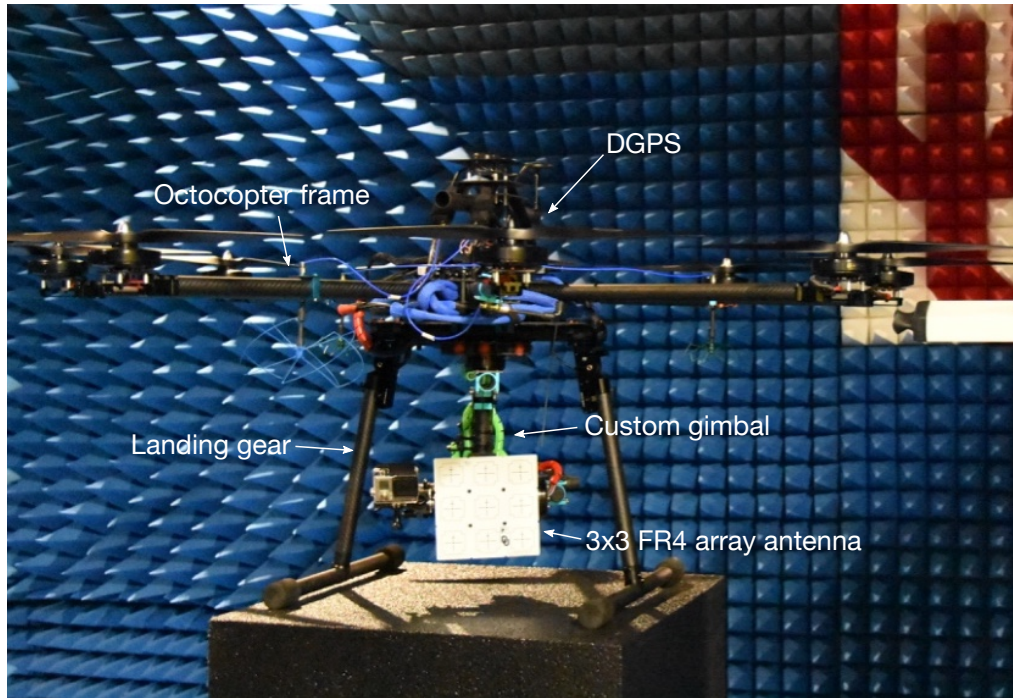


Figure 5.3: The OU-UAVRF1250 platform with the custom made gimbal and the 3x3 FR4 array probe antenna. The frame is an octocopter, with the differential GPS mounted on top, and a retractable landing gear.

drift, position drift, and other UAV structural effects without factoring in outdoor environmental factors.

The key findings from this characterization task were:

- The UAV structure does not significantly alter the co-polarization antenna patterns, in the main beam and sidelobe region, where performance is critical. However, the cross-polarization levels were significantly higher ( $>10$  dB) which could be attributed to the UAV structure itself, the gimbal vibration, and other factors.
- The relative orientation of the gimbal with respect to the UAV frame was significantly affecting the radiation pattern at the antenna's boresight. It is important that the amplitude (or power) of the radiation pattern stay relatively constant throughout the range of operation of the gimbal, or conversely, to be able to predict such behavior and correct as required (see tracking mode, Chapter 4).

It was concluded that the interaction of the UAV frame and gimbal were negatively impacting the performance of the system, by increasing the cross-polarization levels to an unacceptable amount, and by introducing an unpredictable behavior of the probe antenna's radiation pattern near broadside. These findings showed that a more rigorous study of the interaction between the probe antenna and the UAV frame, taking into account the gimbal's relative orientation, was required to appropriately assess the performance of the measurement system.

### **5.1.3 DJI S900 (2017-2019)**

Keeping some of the hardware used in the previous iteration, it was opted to migrate to a smaller yet more stable platform. The DJI S900 hexacopter has a total weight of approximately 4 kg, diagonal size of 900 mm, with a maximum flight time of 15-18 mins. The frame was used in combination with a Pixhawk 2 open-source flight controller, a Here+ RTK system for centimeter accuracy in positioning, and an InfinityMR PRO V2 gimbal.

This platform has seen quite a few modifications along the years, being thus far the one that has been tested most extensively and with the most recorded flight time. As far as the probe antenna interaction with the UAV frame and gimbal is concerned, different types of probe antennas have been thoroughly characterized in free space and on the UAV, both in simulations and in anechoic chamber measurements (see Chapter 4) prior to any outdoor testing. The key lessons from this UAV and probe characterization efforts were:

- Microstrip patch array antennas of 3x3 elements and smaller at S band (3.0 GHz) were still introducing ripples in the co-polarization and cross-polarization patterns large enough to be a significant source of uncertainties in the measurements [16], [34].

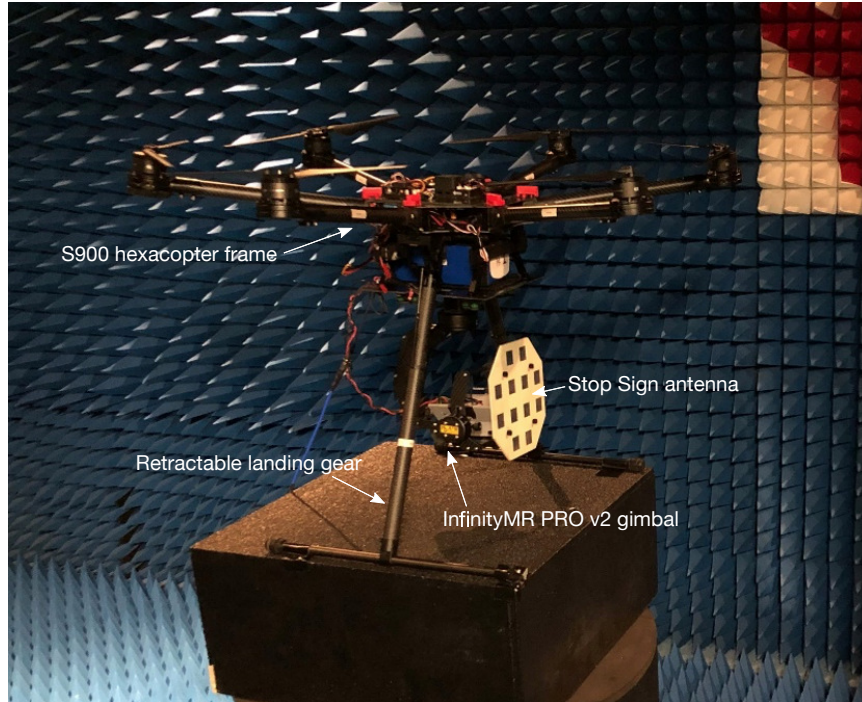


Figure 5.4: The DJI S900 platform with the InfinityMR PRO v2 gimbal and the SS probe antenna.

- The cross-polarization levels of the tested probes were not meeting the minimum requirements for AUTs with low cross-polarization. Gimbal steering would help mitigate this issue to some extent, but it is not the ideal solution.

It was opted to design and fabricate another antenna called the “Stop Sign” (SS) antenna [35], which is a dual-polarized truncated 4x4 microstrip patch array consisting of 12 elements (more details in upcoming section), which was satisfactory in exceeding the minimum requirements.

Other performance improvements were made possible in virtue of advances in the DGPS technology, which allowed obtaining positioning accuracy of less than 10 cm in the  $x$ ,  $y$ , and  $z$  axes [34]. Also, the 3-axis gimbal with an accuracy of  $0.02^\circ$  allowed for a precise and virtually drift-free operation during the characterization process. Many outdoor measurement efforts took part using this platform, with promising preliminary results suggesting that co-polarization measurements were possible with

high degree of accuracy, but cross-polarization measurements below -45 dB were still challenging as the positioning and targeting accuracy were very critical.

Although substantial progress has been achieved with this platform, other issues led to the migration from this platform to a better one, namely the discontinuation of spare parts of the UAV frame, and incompatibility between the gimbal controller and flight controller firmware. Additionally, with future operations and backwards compatibility in mind, it has been opted to migrate to a fully proprietary solution such that continuous support can be obtained (if needed) directly from the manufacturer.

#### **5.1.4 DJI Matrice 600 Pro (2019-present)**

The Matrice 600 Pro (M600P) is the manufacturer-suggested upgrade from the S900. This upgrade comes with substantial improvements in terms of flight performance, while the geometry of the frame remains similar enough such that the RF performance of the SS antenna as a probe does not vary significantly in comparison to the previous platform. A formal and detailed description of the system, its components, and field campaigns will be presented in the subsequent sections.

## **5.2 System Description**

In this section, a complete description and some performance indicators of the current platform's subsystems will be presented. The discussion will be divided into the mechanical subsystem (i.e., the aircraft (UAV) and the peripheral (gimbal)), and the RF subsystem (i.e., probe antenna, transmitter, receiver, and other components in the chain).

## 5.2.1 Mechanical Subsystem

### 5.2.1.1 UAV and Gimbal

As previously mentioned, the M600P is the manufacturer-suggested upgrade from the previous platform, and it comes with substantial improvements in terms of flight performance, with a relatively similar frame geometry and RF performance of the SS probe antenna when mounted on the gimbal. The M600P hexacopter platform has a diagonal size of 1133 mm, total weight (gimbal and RF equipment included) of 16 kg, and a maximum flight time of 16-18 mins, and with the DJI D-RTK system, sub-centimeter accuracy on all axes can be achieved. The DJI Ronin-MX gimbal



Figure 5.5: The DJI Matrice 600 Pro platform with the Ronin-MX gimbal and the SS probe antenna, with triple GPS sensors for redundancy during flight, and dual RTK antennas for increased positioning accuracy.

fully supports integration with the M600P, controlled manually or by point-of-interest (POI) through the mission planner application, with an accuracy of  $0.02^\circ$ . The nominal specifications are listed in Table 5.1 for the M600P, and in Table 5.2 for the Ronin-MX.

Aircraft (Matrice 600 Pro)	
Type	Hexacopter
Diagonal Size	1133 mm
Dimensions	1668 mm x 1518 mm x 727 mm
Weight (no payload)	10 kg
Max Takeoff Weight Recommended	15.5 kg
Hovering Accuracy	GPS: horizontal $\pm 1.5$ m, vertical $\pm 0.5$ m RTK: horizontal $\pm 1$ cm, vertical $\pm 2$ cm
Max Angular Velocity	Pitch: $300^\circ/\text{s}$ , Yaw: $100^\circ/\text{s}$
Max Pitch Angle	$25^\circ$
Max Wind Resistance	8 m/s
Max Ascent Speed	5 m/s
Max Descent Speed	3 m/s
Max Service Ceiling Above Sea Level	2500 m
Max Speed	40 mph
Hovering Time	No payload: 38 min, 5.5 kg payload: 18 min
Max Speed	40 mph
Flight Control System	A3 Pro
Propulsion System	Motors: DJI 6010, Propellers: DJI 2170R
Retractable Landing Gear	Standard
Operating Temperature	$-10^\circ\text{C}$ to $40^\circ\text{C}$

Remote Controller	
Operating Frequency	2.400 GHz to 2.483 GHz, 5.725 GHz to 5.825 GHz
Max Transmission Distance	FCC compliant: 5 km CE compliant: 3.5 km (unobstructed, free of interference)
Transmitter Power (EIRP)	20 dBm @ 2.4 GHz, 13 dBm @ 5.8 GHz
Video Output Port	HDMI, SDI, USB
Operating Temperature	$-10^\circ$ to $40^\circ$
Battery	6000 mAh LiPo 2S

Battery		
	TB47S	TB48S
Capacity	4500 mAh	5700 mAh
Voltage	22.2 V	22.8 V
Battery Type	LiPo 6S	LiPo 6S
Energy	99.9 Wh	129.96 Wh
Net Weight	595 g	680 g
Operating Temperature	$-10^\circ\text{C}$ to $40^\circ\text{C}$	$-10^\circ\text{C}$ to $40^\circ\text{C}$
Max Charging Power	180 W	180 W

Charger (MC6S600)	
Voltage Output	26.1 V
Rated Power	600 W
Single Battery Port Output Power	100 W

Table 5.1: M600P platform specifications.

Gimbal (Ronin-MX)	
Operation Modes (Ground) Operation Modes (Airborne)	Underslung, Upright, Briefcase, Jib or Wirecam Free, Follow, FPV Independent IMU module DJI specialized gimbal drive motors with encoders
Built-in Modules	Bluetooth USB connection 2.4 GHz receiver Temperature sensor DJI advanced 32-bit DSP D-bus receiver
Peripheral	
Bay Dimensions	Maximum depth from base plate CG: 120 mm Maximum height from top of base plate: 130 mm Maximum width: 160 mm
Accessory Power Connections GCU Input Power Connections	2x 12 V regulated P-Tap, 1x USB 500 mW, 1x DJI Lightbridge 4S Ronin-M battery 2.4 GHz remote controller, Bluetooth 4.0, USB 2.0
Mechanical and Electrical Characteristics	
Working Current	Static current: 300 mA (@ 16 V) Dynamic current: 600 mA (@ 16 V) Locked motor current: max 10 A (@ 16 V)
Run Time	3 hrs
Operating Temperature	-15°C to 50°C
Weight	2.15 kg
Gimbal Dimensions	280 mm (W) x 370 mm (D) x 340 mm (H)
Performance	
Payload Weight	4.5 kg
Angular Vibration Range	$\pm 0.02^\circ$
Maximum Controlled Rotation Speed	Yaw: 200°/s Pitch: 100°/s Roll: 30°/s
Mechanical Endpoint Range	Yaw: 360° Pitch: -150° to +270° Roll: $\pm 110^\circ$
Controlled Rotation Range	Yaw: 360° Pitch: -135° to +45° Roll: $\pm 25^\circ$

Table 5.2: Ronin-MX gimbal specifications.

Currently, in addition to the basic UAV platform setup, three additional sets of six TB48S batteries and an additional charger complement the operations in the field, which allow continuous flight missions with approximately 10 to 15 mins of flight time depending on the wind conditions while the remaining sets of batteries are recharging. For the gimbal, two additional batteries allow for minimal to no downtime in the RF operations.

### 5.2.1.2 Positioning Performance

The precision of the standard on-board GPS and the add-on D-RTK modules has been analyzed both on the ground and in the air under strong wind conditions. For the ground tests, the UAV was placed on the ground with the landing gear extended, in three different locations, with a recording time of approximately 5 minutes, or 12000 sample points at each location (Figure 5.6a), while the data is captured simultaneously for both the GPS and the RTK. The reference point is the mean of the RTK point-cloud for the first position. Figure 5.6b, c, and d show a closer look at the footprint generated by the UAV at positions 1, 2, and 3, respectively, with the blue track representing the standard GPS data, and the red tracks the RTK data. The superior precision of the RTK can be immediately seen as the cloud of red points have such a small variability that they appear as a single point on this scale, while the GPS track seems to drift over time within a few meters. Additionally, the standard GPS is likely more susceptible to bias due to this drift. The standard deviations of the positions are listed in Table 5.3. The precision of the GPS is roughly  $\pm 0.5$  m in

	Position 1			Position 2			Position 3		
	$\sigma_x$ (cm)	$\sigma_y$ (cm)	$\sigma_z$ (cm)	$\sigma_x$ (cm)	$\sigma_y$ (cm)	$\sigma_z$ (cm)	$\sigma_x$ (cm)	$\sigma_y$ (cm)	$\sigma_z$ (cm)
GPS	11.96	45.70	70.25	7.58	31.87	41.96	20.69	39.39	55.86
RTK	0.28	0.31	0.70	0.23	0.40	0.63	0.25	0.45	0.69

Table 5.3: Standard deviations of the UAV positions for different ground locations.

the horizontal axes, while in the vertical axis it is at least  $\pm 0.75$  m, as measured, which is within the expected range of the nominal specifications. The RTK precision

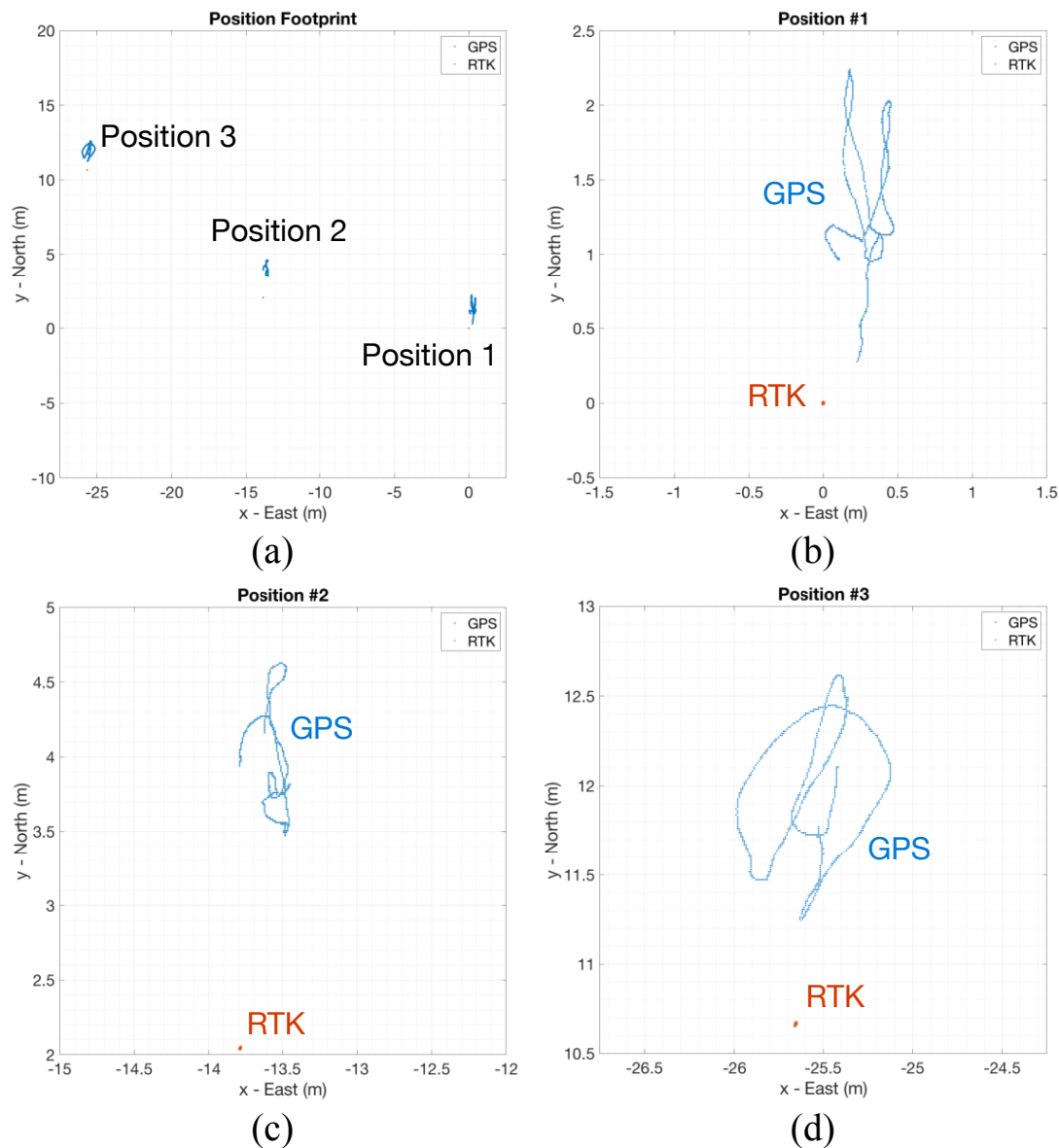


Figure 5.6: Footprint of the UAV in ENU coordinate system for different ground locations with standard GPS data shown in blue tracks, and RTK data in red: (a) Zoomed out showing all the different positions. (b) Zoomed in on position 1 for clarity. (c) Zoomed in on position 2. (d) Zoomed in on for position 3.

is consistently less than  $\pm 1$  cm in both horizontal and vertical axes, which in fact exceeds the nominal specifications. Overall, the difference in precision is roughly in the order of  $10^2$ , and this clearly illustrates the performance gain in positioning of the RTK over the standard GPS when the UAV is static.

With the positioning precision analyzed on the ground, a baseline has been established for the best case scenario, or when there is no wind resistance during flight. It is also important to perform a similar analysis for the positioning mid-air, to assess how much the precision degrades during a mission. For this case, the UAV was flown in hover mode at a nominal height of 30 m AGL, with the flight controller using the GPS sensor data only, and again with the flight controller using the RTK data only. The wind direction and speed were S 21 mph at the time of testing. The tracks for both flights are shown in Figure 5.7. The standard GPS shows a bias in altitude

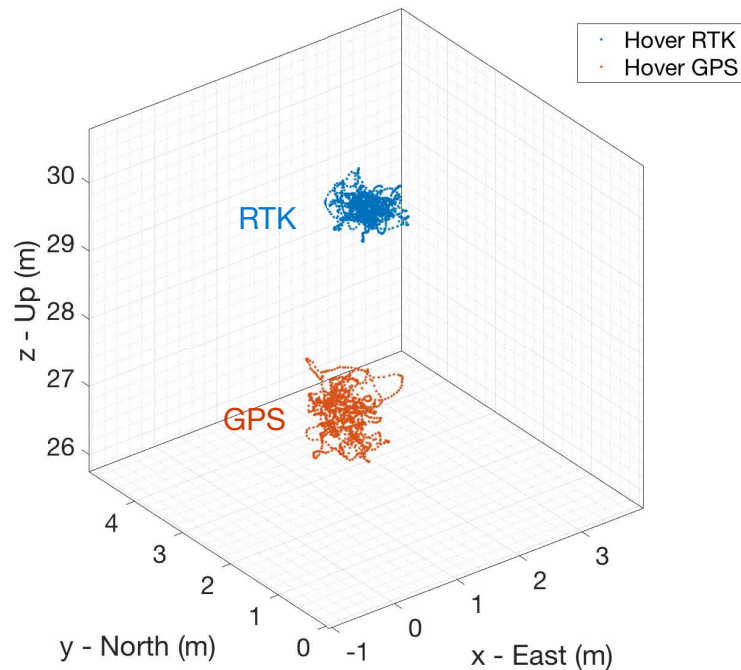


Figure 5.7: UAV tracks in ENU coordinate system relative to home (takeoff) position during hover mode in RTK (blue), and GPS (red) operation.

of approximately 5 m with respect to the RTK data set, and this has been visually

confirmed on site, although the height set points were 30 m for both flights. The mean height of the RTK data during the hover operation is 30.43 m, while for the GPS it is 26.43 m. The standard deviations for both flights are relatively comparable in the horizontal axes in the order of 20 cm, although in the vertical axis there is an approximately threefold difference, with the RTK being more precise at around 10 cm, whereas the GPS stands at 30 cm. These values are summarized in Table 5.4.

	$\mu_z$ (m)	$\sigma_x$ (cm)	$\sigma_y$ (cm)	$\sigma_z$ (cm)
GPS	26.43	28.53	24.31	28.23
RTK	30.43	20.17	22.07	10.54

Table 5.4: Flight performance for hover mode under S 21 mph winds for GPS and RTK.

The bias from the desired altitude set point is less than 0.5 m for the RTK, and less than 4 m for the GPS. With the ground precision as a baseline, it can be concluded that the lower precision in flight is very likely due to the platform instability under strong winds. Nevertheless, depending on the measurement range from the AUT, the achieved precision should suffice for the intended purpose.

### 5.2.1.3 Orientation Performance

The most relevant way to assess the performance and establish a baseline of the gimbal’s targeting precision is indirectly by measuring the the RF signal strength in a controlled environment over an appropriate period of time with the gimbal operational. In this sense, the gimbal drift, if any, should directly correlate into variations of the probe antenna’s signal strength upon transmission (or reception). The setup consists in the UAV being placed inside the anechoic chamber with the gimbal operating in free or follow mode, with the probe antenna transmitting while the chamber’s VNA is receiving and recording data continuously over a period of approximately 16 minutes, which corresponds to a maximum flight time of the platform under ideal conditions. With the gimbal in free mode, it can be set to follow any desired orientation, while in follow mode it will adjust its yaw angle accordingly to follow the

nose of the UAV frame. The set point values may be different depending on the operational mode of the gimbal but they remain constant over time, thus the drift can be characterized regardless of the mode.

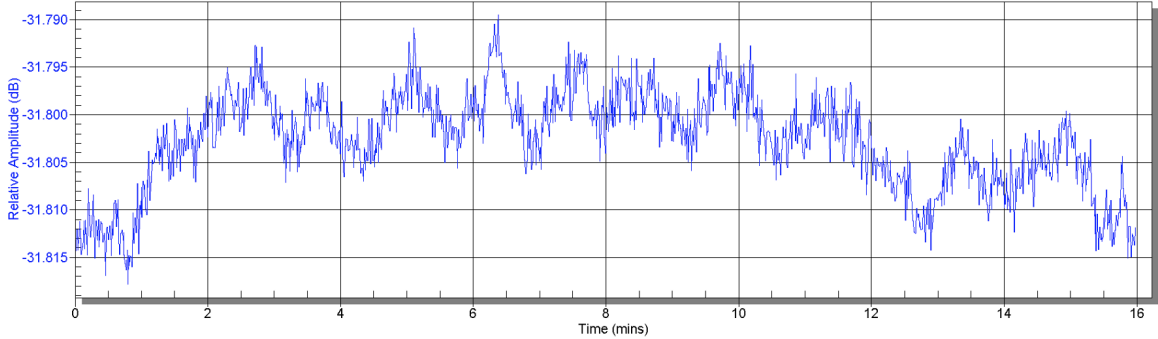


Figure 5.8: Orientation performance measured in terms of RF variability through gimbal drift.

A plot of the receiver amplitude as a function of time is shown in Figure 5.8. The peak-to-peak excursion of the amplitude over a period of time of 16 mins is 0.03 dB, with a drift of less than a hundredth of a dB in amplitude, and less than a degree in phase. While this experiment does not rule out the possibility of the gimbal having a mechanical drift over time of any of its three axes, it shows that even if there was a drift, it does not significantly affect the RF performance of the probe antenna.

## 5.2.2 RF Subsystem

### 5.2.2.1 Probe Antenna: “Stop Sign”

As a replacement for the previously used FR4 3x3 array dual-polarized probe antenna [16] which was found to be unreliable due to the ripples introduced in the co-polarization patterns, as well as the high cross-polarization contamination from the UAV frame, an improved probe antenna has been designed and fabricated specifically for this application.

The “Stop Sign” antenna (hereafter, SS) is an S-band dual-polarized corner-truncated 4x4 patch array with corporate feed networks for each polarization on

a basic Rogers 4350B stackup, which is more mechanically stable and lighter than the previous 3x3 FR4 array. The corporate feed network is designed using several power splitters based on transmission line theory to obtain an equal magnitude and constant phase distribution at the output ports, and it is selected in virtue of its design flexibility and ease of integration to form two-dimensional microstrip arrays. The SS has been optimized for 3.02 GHz, which is the notional operational frequency of MPAR, with a bandwidth of approximately 70 MHz, a simulated cross-polarization isolation of 55 dB at broadside (an improvement of roughly 25 dB over the previous probe), an overall beamwidth of around  $28^\circ$ , and an aperture of 20 cm. The 12-element ( $0.5\lambda$  spacing) SS array's stackup allows for isolated power division 12 ways for each of H and V polarizations, and the matching between the polarizations has been optimized from an impedance and pattern perspective near broadside and over the antenna bandwidth.

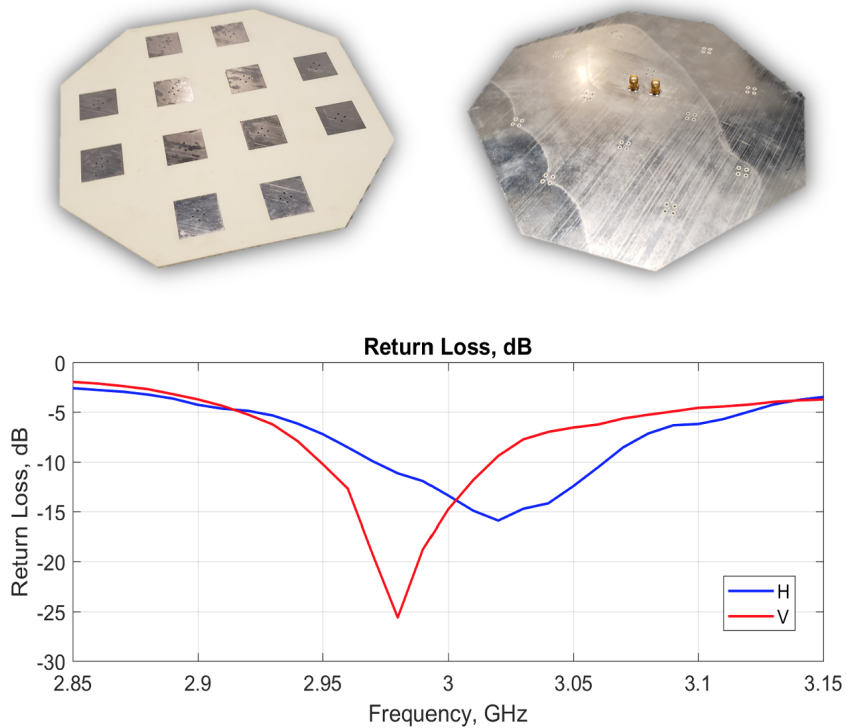


Figure 5.9: The Stop Sign (SS) antenna front and back (top), and the return losses in H and V (bottom).

The SS has been thoroughly characterized in free space and mounted on the UAV in the anechoic chambers, and the performance and limitations have been discussed in Chapter 4.

### 5.2.2.2 Signal Generator

The Windfreak Technologies SynthHD is a 10 MHz to 15 GHz dual channel software tunable RF signal generator and frequency sweeper. The dual independent channels

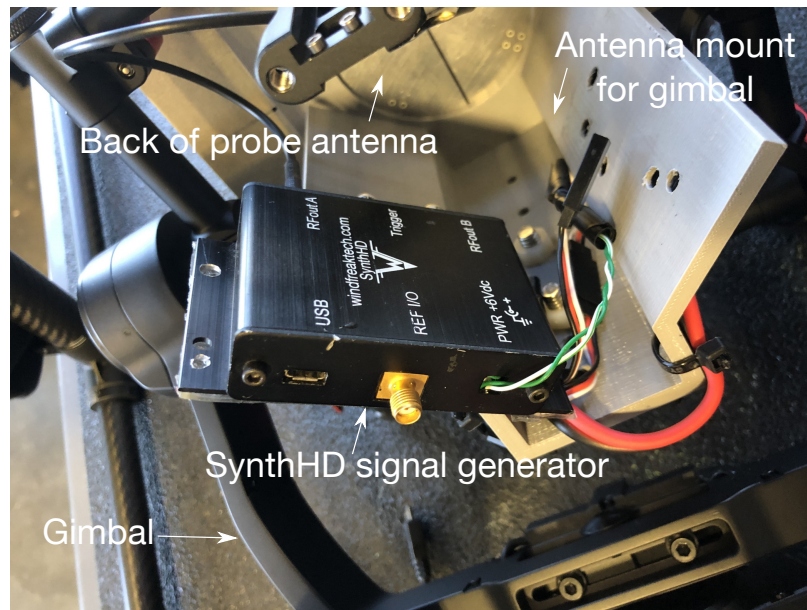


Figure 5.10: Windfreak Technologies SynthHD signal generator mounted on the gimbal.

can be configured to run as two different frequencies, or the same frequency with different phases, allowing its use in antenna beam steering applications or quadrature signal generation. The SynthHD also has a nonvolatile on-board flash memory that allows operation in the field with its stored configurations, making it a highly mobile, low power and light weight solution for RF signal generation. It can output up to +20 dBm in each channel, with a 50 dB dynamic range, 0.1 Hz frequency resolution, 0.01 dB amplitude resolution, and  $0.01^\circ$  phase resolution. Although currently the synthesizer is only configured for generating a CW signal at the desired frequency, for future applications, it is also capable of generating pulsed signals and FMCW chirps.

A complete description of the hardware characteristics and performance can be found in the manufacturer’s datasheet.

### 5.2.2.3 Polarization Switch: “Twitchy”

The Twitching Eye of Horus, or Twitchy, for short, is a circuit consisting of capacitors, a 555 timer, and an RF switch, which controls the input signal to generate H- and V-polarized signals alternately in the order of a fraction of a millisecond (i.e., toggle rate of a few kHz), with an isolation better than 40 dB. The H and V pulses from

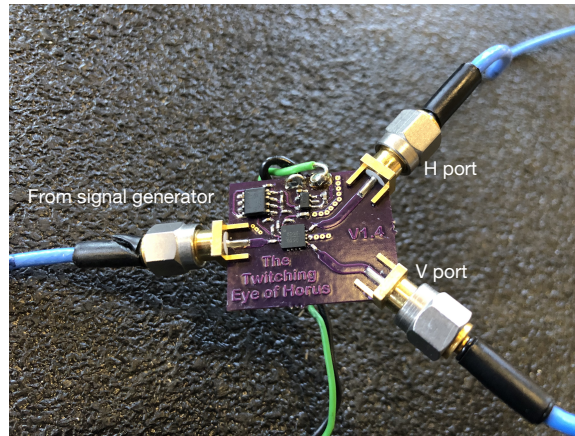


Figure 5.11: Twitchy circuit used for polarization switching between H and V.

Twitchy can be recorded with a spectrum analyzer in zero span, an oscilloscope, or the radar’s receiving subsystem, where additional signal processing is required [87]. With this circuitry, it is possible to transmit in both orthogonal polarizations during the same mission, thus allowing at the minimum a twofold improvement in measurement time and with collocated transmitter locations, at the expense of the additional signal post-processing that is required.

### 5.2.2.4 Receivers

On the receiving end, a handheld microwave analyzer FieldFox N9917A is used alongside an amplifier board. The amplifier board consists of four different amplifiers: Minicircuits V63 (50 MHz to 6 GHz), Minicircuits V83 (20 MHz to 4.7 GHz), Avantek

AWT-18057 (8 to 18 GHz), and Miteq AFS3 (2 to 4 GHz); and a low-noise amplifier (LNA) Pasternack PE1524 (2 to 18 GHz). The wide range of frequencies ensures that most of the bands of interest (S, C, and X) are covered. A proper characterization of the devices was presented in [16].

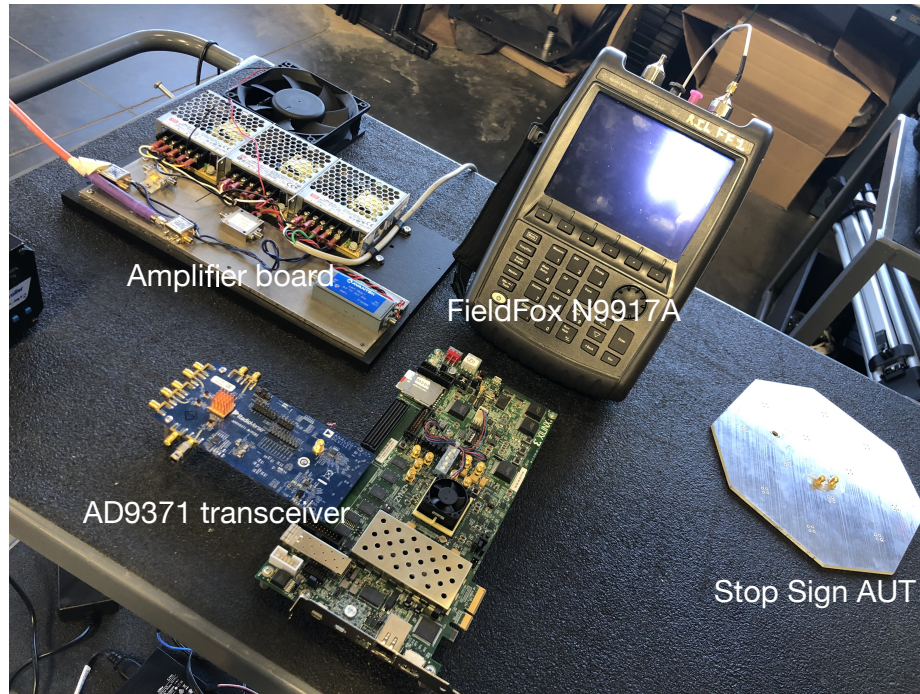


Figure 5.12: Some of the instrumentation for the receiver subsystem: amplifier board, FieldFox N9917A, an AD9371 transceiver board, and the SS AUT.

The FieldFox N9917A is a portable high performance RF and microwave analyzer with the precision of a benchtop system. It can be configured as a cable and antenna analyzer, 2-port vector network analyzer, spectrum analyzer, built-in power meter, with some of its key features listed next.

1. Cable and Antenna Analyzer (CAT), Vector Network Analyzer (VNA)

- Frequency range: 30 KHz to 18 GHz
- Dynamic range: 91 dB
- CAT: Distance-to-fault, return loss, cable loss
- VNA: S11, S21, S22, S12, magnitude and phase

- Output power: -4 dBm
- Number of ports: 2
- Displayed average noise level @ 1 GHz: -155 dBm
- Overall amplitude accuracy:  $\pm 0.5$  dB

## 2. Spectrum Analyzer (SA)

- Frequency range: 5 KHz to 18 GHz
- Amplitude accuracy:  $\pm 0.5$  dB, full band, over full temperature range of -10 to 55°
- Dynamic range: 105 dB @ 1 Hz RBW

Complete details can be found on the manufacturer's datasheet.

Other portable transceivers such as the Analog Devices AD9361 and AD9371 have been studied as strong candidates as the receiving hardware in the case where the UAV would be receiving instead of transmitting, and it has been tested to be capable of receiving and demodulating the direct pulses from real radar systems with sufficient phase coherency. However, the main focus for the scope of this study is using the UAV and probe antenna as the transmitting source in FF.

Additionally, data recording is mostly done in the receiver end as well, where in addition to the RF measurements, the timestamps are also stored such that any synchronization or corrections needed based on the flight track can be done accurately in post-processing.

## 5.3 Outdoor Operations

A summary of the currently applicable regulations regarding UAV operations is presented in the appendix. From an engineering perspective, the main limitations due to said regulations are that the aircraft is restricted to less than 55 lbs (25 kg), with

a maximum ground speed of 100 mph, a maximum altitude cap of 400 feet above ground level, and may generally not take place within 400 feet of a building, structure, or vehicles. With this in consideration, the different flight strategies that are theoretically possible or have been tested will be discussed as part of the methodology. And finally, the results from different field campaigns using the M600P UAV and the SS probe antenna will be presented and discussed.

### **5.3.1 Methodology**

The flight track of the UAV with respect to the AUT determines what plane and cut of the antenna pattern is measured. Some flight strategies have been presented in [16] with a more comprehensive theoretical analysis in terms of distance covered, flight time, UAV speed, for different radar systems. In this section, the flight strategies that have been tested in the field will be discussed, which include hover mode, circular mode, and vertical grid mode, along with a discussion on the feasibility other possible modes.

#### **5.3.1.1 Hover Mode**

In hover mode, the UAV attempts to remain quasi-stationary about a point in space that meets the requirements for FF measurements in terms of the range and relative height from the AUT according to the design parameters derived in Chapter 3. This measurement setup is identical to many FF anechoic chamber and elevated outdoor range setups, where the AUT is mounted on a mechanical device that allows rotation in orthogonal axes to obtain different cuts of the principal planes to be measured while the probe antenna remains stationary, with the exception that in the case of the UAV, the probe antenna is not stationary but mobile. In this sense, the positioning subsystem of the AUT/SUT will define the extent of the characterization capabilities. In other words, the plane cuts that are achievable in this setup will be exclusively

defined by the rotation of the AUT, since the UAV remains mostly quasi-stationary at one point in space. Conversely, if the AUT is a fixed, electronically steered phased array antenna, this mode is not ideal since only the radiation in one direction will be captured. Nevertheless, if there are any physical restrictions in place that prevent other types of missions (see Section A), the hover mode is the preferred mode of flight. A sketch of a typical configuration is shown in 5.13.

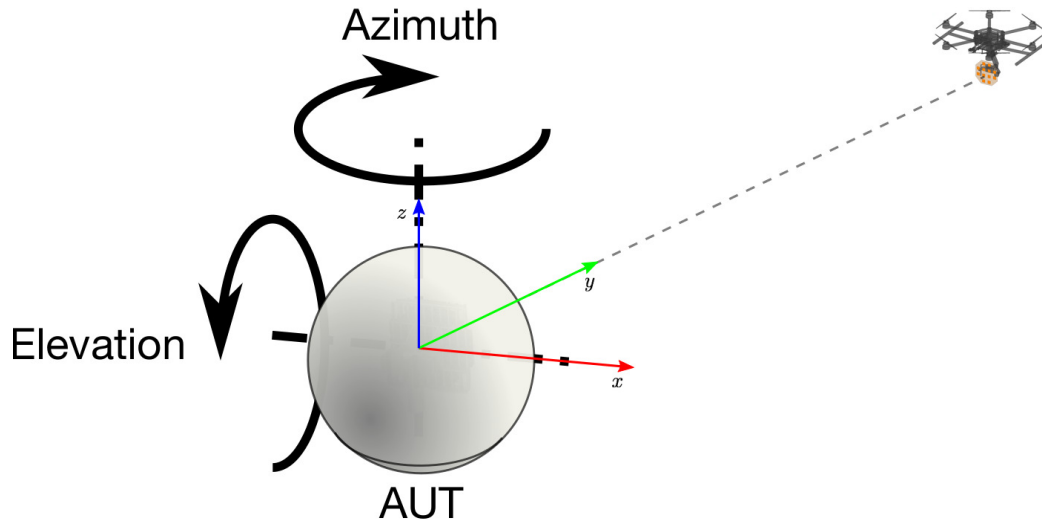


Figure 5.13: Illustration of a hover mode method for UAV-based antenna measurement. The UAV hovers in a point in space while the AUT scans mechanically in azimuth and/or elevation.

A flight track from one of the field measurements is also depicted in Figure 5.14.

As one would expect, the wind conditions are extremely critical for the hover mode operation. The positioning performance in hover mode under relatively strong winds has been presented in Section 5.2.1.2. In general, the receiver data will be an average over a number of samples that are collected throughout the mission for each direction of interest, thus, it can be more challenging to establish a one-to-one relationship between the exact measured position of the UAV and the corresponding RF measurable. Therefore, it is preferred to record all the raw data in real time with no averaging before any post processing is performed.

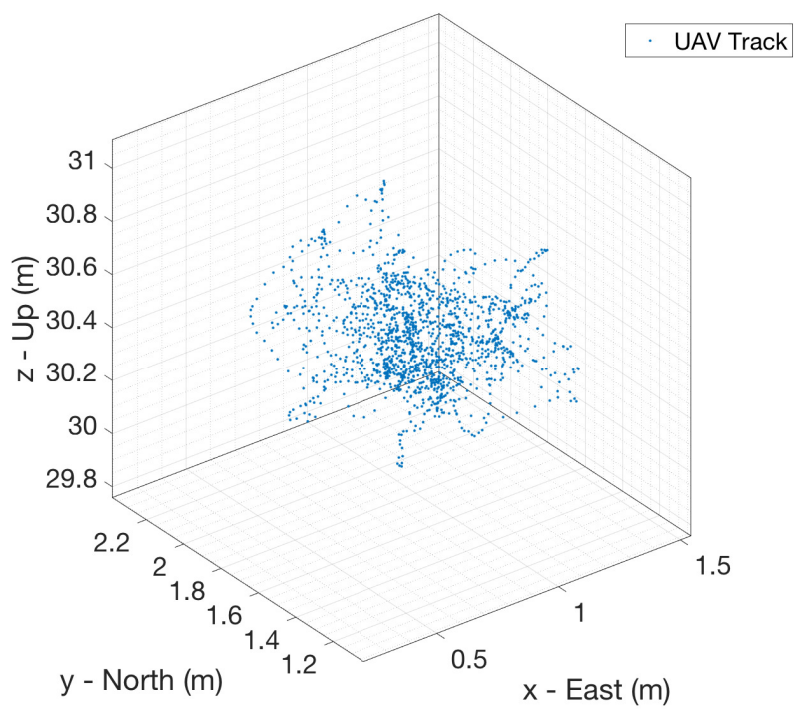


Figure 5.14: Hover flight pattern extracted from the flight log. The UAV is hovering at a nominal altitude of 30 m AGL.

The typical procedure with the M600P for a hover flight is to, after takeoff, set the point of interest (POI) as close as possible to the AUT phase center. This allows the UAV nose to be pointing in the direction of the AUT at all times. After the POI has been established, the relative distance and height from the POI can be set through the flight controller ground station, with the speed of the UAV set to zero, such that the UAV remains suspended about this point. This method allows for accurate range and height control from the AUT, and also allows for the gimbal controls to align the probe antenna with the AUT phase center at all times (i.e., targeting mode) always keeping the roll axis leveled (i.e.,  $0^\circ$ ) and allowing for compensation of the pitch and yaw axes.

An alternative method to perform hover mode is by directly setting a waypoint on the UAV mission planner with the desired range and altitude, however, due to GPS bias, it was found to be more difficult to obtain accurate control of the exact position of the UAV with this method. Nevertheless, if the GPS bias in the map application is corrected, this method would be the preferred choice since it also allows for automated missions from takeoff to landing.

#### **5.3.1.2 Circular Mode**

If the AUT positioning mechanism does not allow for rotation, a circle flight path allows the extraction of the antenna pattern in circular cuts. For the sake of simplicity, circular mode will refer to a horizontal cut of the AUT's radiation pattern, which can either be a principal plane cut (great circle) or a conical cut depending on the relative orientation of the AUT beam and the UAV probe beam. When measuring a principal plane in this mode, the typically achievable antenna pattern cuts are H-polarization E-plane, and V-polarization H-plane. A sketch of a typical configuration is shown in 5.15.

A flight track from one of the field measurements is also depicted in Figure 5.16.

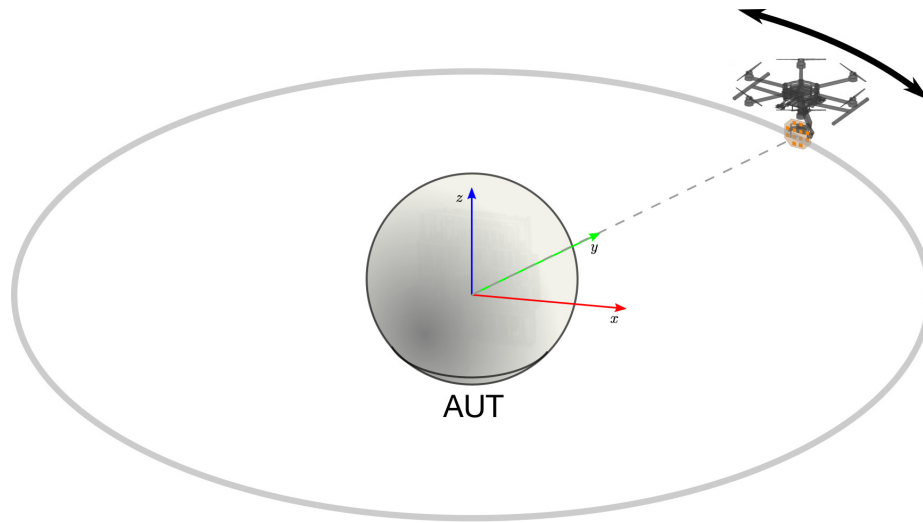


Figure 5.15: Illustration of a circular mode method for UAV-based antenna measurement. The AUT is stationary, while the UAV scans around the nominal AUT phase center.

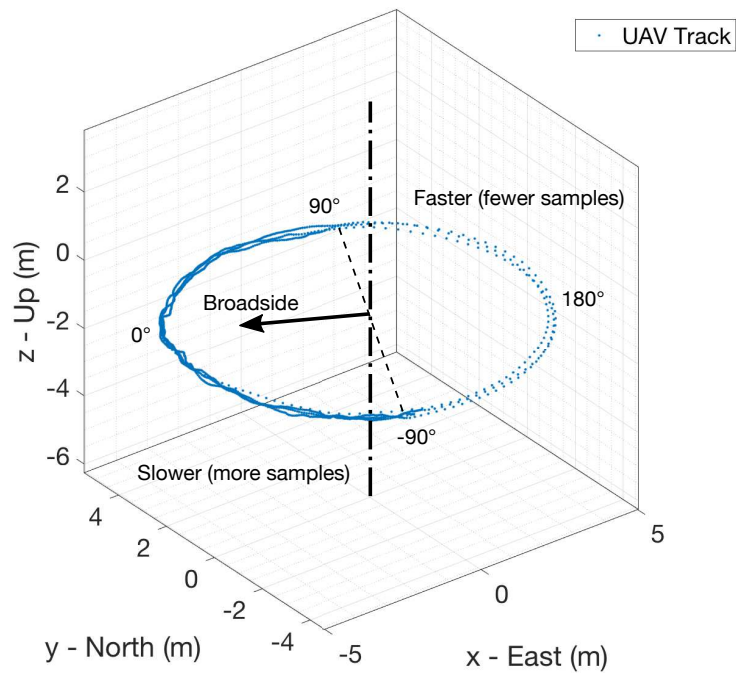


Figure 5.16: Circular flight pattern extracted from the flight log. The radius of flight is 5 m. Higher density of samples corresponds to a slower flight speed, while the lower density corresponds to a faster flight speed.

A circular flight pattern is generally less vulnerable to wind resistance since the UAV is not constantly adjusting its position to compensate for the wind forces, as it does in hover mode. On the AUT side, the recording is done continuously at an adequate sampling rate while capturing the timestamp on both the AUT and UAV, such that the RF measurements can be correlated to the probe antenna positions. Then, any necessary corrections are added and the antenna pattern can be reconstructed properly in post-processing.

The typical procedure with the M600P for a circular flight is to, after takeoff, set the point of interest (POI) as close as possible to the AUT phase center, and set the orbiting function in the flight controller application. After the POI has been established, the UAV nose will be pointing in the direction of the AUT at all times, and by setting the radius of the circle and height from the POI and an appropriate flight speed, the UAV will continuously fly in circles with the POI (AUT) in the center. As with the first hover method, accurate radius and height control from the AUT can be achieved, while also allowing sufficient gimbal alignment of the probe and AUT.

The alternative method to perform circle mode is by designing flight pattern in forms of waypoints arranged in a circle in the UAV mission planner with the desired radius and altitude. While this method allows for automated missions, the current mission planner application has a few limitations with this method that prevented safe and accurate operations, thus the former method was preferred.

### **5.3.1.3 Vertical Grid Mode**

If the AUT is an electronically steered phased array antenna, and the objective is to measure the boresight radiation levels in the orthogonal polarizations simultaneously, a vertical (or spherical) grid flight path is convenient. The term vertical implies that the scanning plane is oriented vertically with respect to the ground, but the longer

grid segments are horizontal with discrete changes in altitude. A demonstration of this scheme has been presented in the form of simulations in Chapter 3, where the objective is to measure the co-polarization mismatch between the H and V polarizations for each beam position (scanning angle of the phased array antenna). If the beam is not being steered, the family of antenna pattern cuts that can be measured with a vertical grid is virtually the whole broadside hemisphere of the 3D AUT radiation pattern. A sketch of a typical configuration is shown in 5.17.

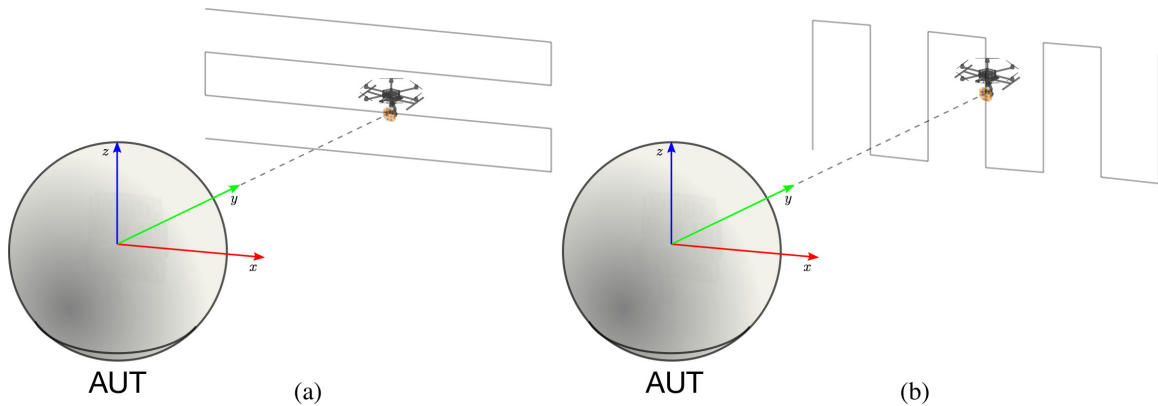


Figure 5.17: Illustration of a vertical grid mode method for UAV-based antenna measurement: (a) grid lines are at a constant altitude, (b) grid lines are vertical.

A flight track from one of the field tests is also depicted in Figure 5.18. This mission is attempted to assess the accuracy of this flight pattern, by setting the grid lines nominally spaced 10 m apart from each other, starting at 15 m AGL, at [15, 25, 35, 45] m. The mean of the grid lines in this particular mission were found to be [14.99, 25.03, 35.04, 45.01] m, with standard deviations of [8.06, 4.52, 7.86, 3.01] cm respectively for each grid line.

The most straightforward method to perform this flight pattern with the M600P is to design a flight pattern with overlapping straight lines at different altitudes at an appropriate distance away from the AUT. This is simply done in the UAV mission planner application, with the POI set to the approximate region surrounding the AUT, such that the gimbal is operating in targeting mode. The main limitation of scanning at higher altitudes is staying below 400 feet AGL, as per the FAA Part 107

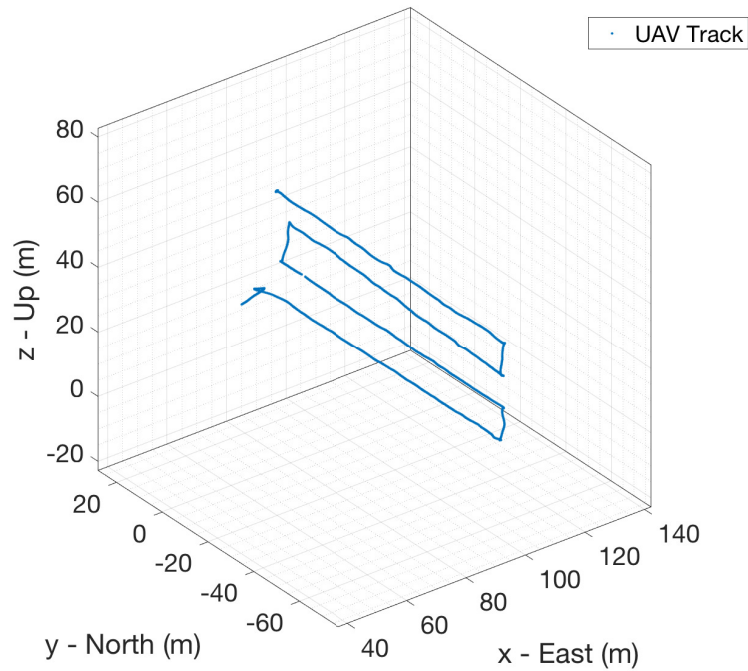


Figure 5.18: Vertical grid flight pattern extracted from the flight log. The grid lines are nominally spaced 15 m apart in height.

regulations. However, given proper planning and communication with corresponding authorities, a waiver may be obtained to work around this issue.

An alternative way to perform vertical grid scans is by having the grid lines vertical instead of horizontal (parallel to the ground). The implication of this is that the UAV would be moving up and down in altitude for discrete horizontal positions along the turning points of the grid. This may not be the preferred method since the UAV performs better in a horizontal motion rather than a vertical one.

#### 5.3.1.4 Other Modes

The above three methods have been tested in the field and found to be realizable in practice. The discussion here extends to other flight patterns that are theoretically possible, but have not been tested thoroughly in the field. Also, it is worth mentioning that some of these methods acquire more importance in NF measurements since they

are mostly analogous to scanning strategies in NF ranges. However, this work only focuses on the FF measurement aspects with the UAV.

## **Rectilinear**

Any segment of a grid can be considered a rectilinear flight path. However, a rectilinear flight pattern along the directions of the principal planes should yield the corresponding antenna patterns for that polarization. For example, for a H-polarization pattern, a rectilinear flight normal to the boresight direction in the azimuthal plane would yield an E-plane cut, while in the elevation plane it would yield an H-plane cut; the converse is true for V-polarization radiation patterns. The above definition implies that the flight paths are contained in a plane normal to the boresight of the AUT, thus, for example, if the AUT is operating at zero degrees in elevation (assuming an azimuth over elevation positioner), one flight would be horizontal (i.e., contained in the  $x$ - $y$  plane) while the other one would be vertical (i.e., only moving in the  $z$  direction). The particular case where the AUT is pointing towards zenith will be discussed in a section ahead. An illustration of a typical configuration is shown in 5.19.

The way to implement this flight in the UAV mission planner should be straightforward with the use of waypoints if the line is contained in a horizontal plane, i.e., the start and end points have the same altitude. For other rectilinear patterns that change in altitude from start to end, the flight path design gets a little more complex, since generally the mission planners do not provide enough flexibility to control the altitude of the UAV accurately.

## **Horizontal Grid**

A horizontal grid refers to one that is essentially contained in a horizontal plane parallel to the ground, and is very commonly used in aerial imaging and surveying

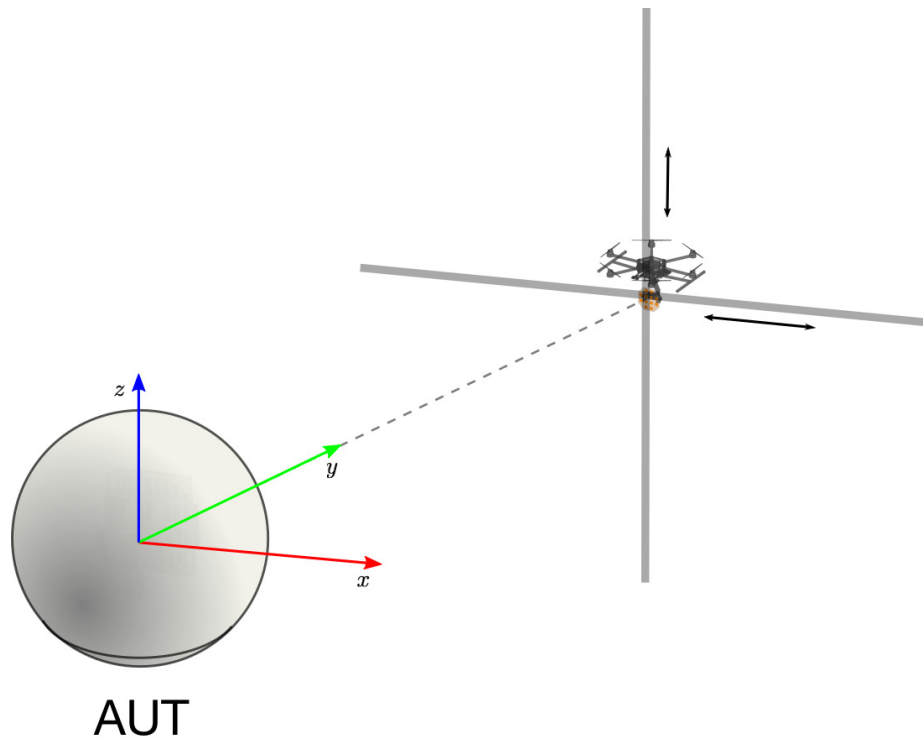


Figure 5.19: Illustration of a rectilinear mode method for UAV-based antenna measurement. The UAV scans in rectilinear flights in two orthogonal directions to extract the radiation patterns of the principal planes.

applications. This type of flight pattern acquires more importance when the AUT is operating with the elevation angle close to zenith. An illustration of a typical configuration is shown in 5.20. Like with the vertical grid, if the beam is not being

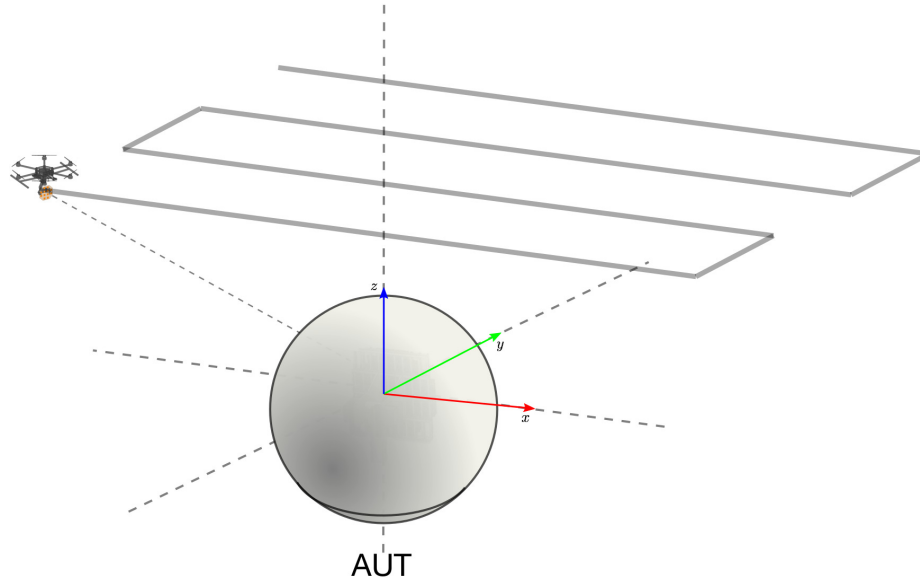


Figure 5.20: Illustration of a horizontal grid mode method for UAV-based antenna measurement. The UAV performs a horizontal scan above the AUT. This method is suitable for “bird bath” mode.

steered, the family of antenna pattern cuts that can be measured with a horizontal grid (assuming the the beam is aligned with zenith) is virtually the whole broadside hemisphere of the 3D AUT radiation pattern.

In virtue of its popularity among the general UAV audience, it is very straightforward to implement horizontal grids, since most mission planners already have this feature. Since the altitude for the horizontal grid is constant, the direction of the grid lines generally should not affect the measured pattern provided that the grid is sufficiently dense and the pattern is reconstructed appropriately in post processing. Depending on the wind conditions it might be preferable to align the grid lines parallel to the wind direction such that there are less cross-track perturbations in the overall flight pattern. Additionally, it may be desirable to align the grid lines to either one of the principal planes to obtain a better resolution in that particular cut.

## Spherical

Spherical flight patterns in azimuth are an extension of the circle mode by essentially performing various circular patterns at different altitudes, with adequately chosen radii and altitudes to cover the surface of a sphere surrounding the AUT. In this sense, a great circle cut in the horizontal plane is sampled, along with various conical cuts at different elevation angles, yielding the upper hemisphere of the 3D radiation pattern of the AUT. The practical implementation of this flight strategy should be

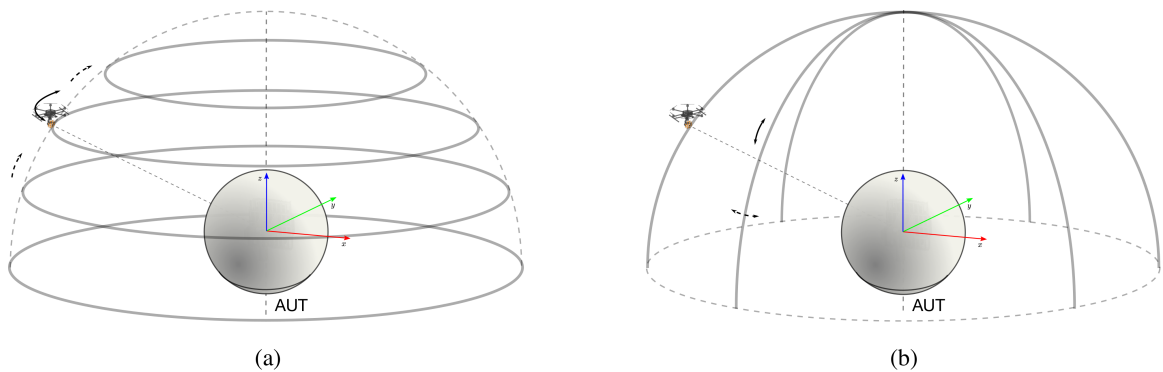


Figure 5.21: Illustration of a spherical mode method for UAV-based antenna measurement: (a) azimuth flights (conical cuts), (b) elevation flights (half great circle cuts).

similar in complexity as a circular pattern, except for varying radii and altitudes for the different circles.

Alternatively, spherical flight patterns in elevation could be possible which would in theory provide different half-elevation cuts, enough to cover the whole upper hemisphere of the sphere surrounding the AUT. The practical implications of this strategy is that it is harder to control the altitude of the UAV accurately, as currently there are no mission planners that allow arc flights with varying altitude as the main controllable parameter.

## “Bird Bath”

In “bird bath” mode, the radar or antenna system is mechanically rotated such that the boresight is aligned with zenith, and is a typically used scheme for  $Z_{DR}$  calibration in polarimetric weather radars, as the shape of the raindrops as seen from directly below is a sphere. Thus, any deviations from the ideal value of 0 dB for spherical scatterers can be corrected in-situ. Additionally, since the system is pointing away from the ground and any structure, the antenna pattern measured in this mode should be relatively free of extraneous reflections. The most relevant flight paths in this operational mode of the AUT are rectilinear and horizontal grid modes.

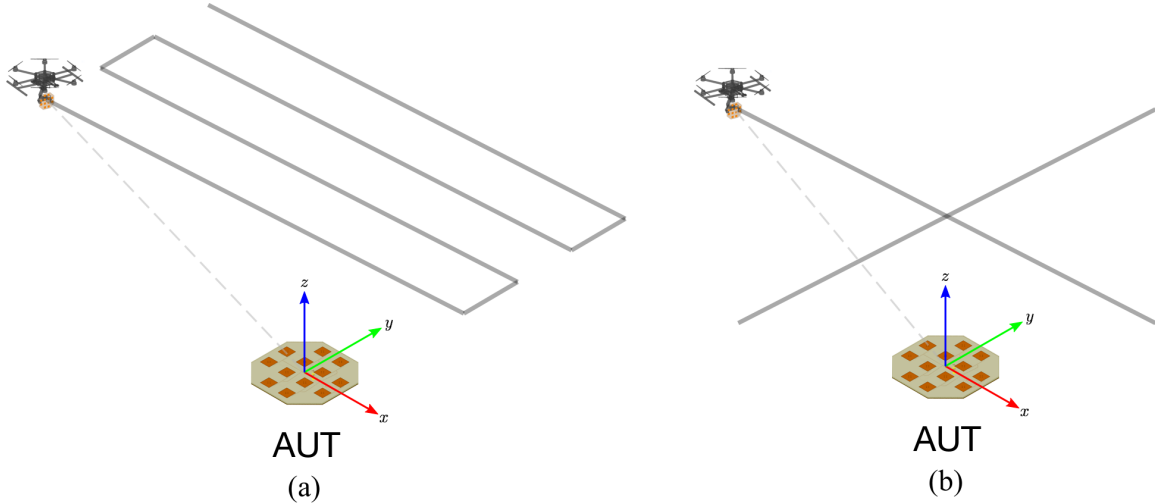


Figure 5.22: Illustration of relevant flight strategies in bird-bath mode for UAV-based antenna measurements: (a) horizontal grid, (b) rectilinear.

### 5.3.2 Results

The performance of the UAV-based antenna measurement system has been tested outdoors with two SS antennas, one as a probe, and the other one as the AUT. Both antennas have been appropriately tested indoors, however, an outdoors reference of the AUT radiation pattern is still required in order to make a fair comparison of the UAV-measured radiation pattern. In addition to the measuring the antenna

patterns of the H-polarization (E-plane), and V-polarization (H-plane) co- and cross-polarization components of the probe on a fixed mast for reference, the UAV-based measurements of the same patterns were performed in hover and circular modes.

### 5.3.2.1 Fixed Reference

To obtain a fixed outdoor reference, the SS AUT is mounted on a rotary table on top of a telescoping mast at a height of 5 m (AUT phase center to ground), which allows rotation in the azimuth direction, and is carefully aligned in the roll and pitch axes. The SS probe is mounted on the gimbal on top of another telescoping mast opposite the AUT's boresight at a range of 5 m and height of 5 m, where the alignment is controlled automatically by the gimbal controls. The measurement range and height were chosen in accordance with the guidelines presented in Chapter 3, as to avoid excessive tapering and ground reflections, as well as making sure it is in the FF region.

The antenna patterns are measured with the rotary table scanning in azimuth with the AUT connected to the receivers, while the probe is transmitting the CW signal. Figure 5.23 shows H-polarization (E-plane) and V-polarization (H-plane) patterns of both the co- and cross-polarizations of the SS probe antenna characterized indoors and outdoors. This setup takes into the account the structure of the gimbal in itself, although the structure of the UAV frame is missing. As such, this case is comparable to a case where the UAV is suspended in free space without motion perturbation due to the wind. It can be seen that the co- and cross-polarization patterns of the H and V polarizations are in general qualitative agreement between the indoor and outdoor measurements. There are, however, external environmental factors that will inevitably modify the behavior of the probe antenna in unpredictable ways, as can be seen by the higher cross-polarization levels and variation in the side lobe and null structure. This validates the possibility of measuring co-polarization levels accurately

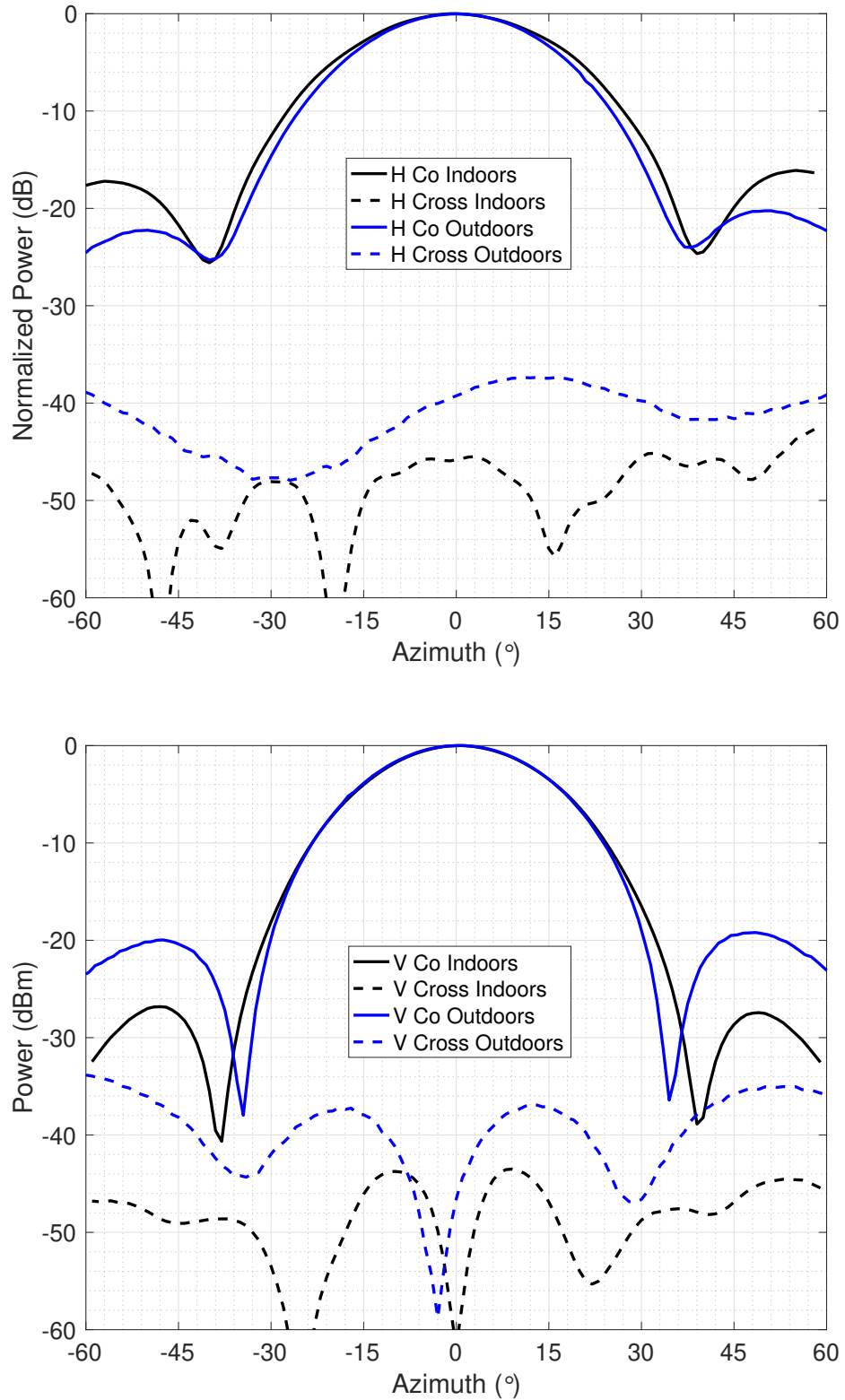


Figure 5.23: SS radiation patterns for H (top) and V (bottom) polarizations obtained from indoor chamber measurements (black) and outdoors (blue). Co-polarization patterns are shown in solid lines, while cross-polarization patterns are shown in dashed lines.

near the beam peak, while measuring cross-polarization levels down to approximately -45 dB and below at and around boresight in an outdoor configuration.

### 5.3.2.2 UAV Hover Mode

For the UAV operating in hover mode, the same height as the fixed reference has been chosen, and the method in Section 5.3.1.1 is followed. The gimbal is removed from the telescoping mast and mounted back on the UAV, and during flight, the AUT is rotating in azimuth. Figure 5.24 shows H-polarization (E-plane) and V-polarization (H-plane) patterns of both the co- and cross-polarizations taken in hover mode. Qualitatively, the antenna patterns can be extracted successfully but, without any reference to compare to, it would be difficult to assess the measurement precision. The cross-polarization levels are measured down to -33.59 dB in H, and -35.01 in V, which shows how the positioning noise and extraneous reflections are degrading the accuracy significantly, although a null in the cross-polarization is shown to be measured down to -48.91 dB off broadside. The  $\sim 4$  dB difference between the peaks in boresight has later been found to be a physical issue with the AUT SS antenna.

It can be seen that in hover mode, qualitatively, the shape of the antenna patterns are captured somewhat accurately. More so in the V-polarization patterns where the null and sidelobe levels are measured properly, with minimal distortion in the co-polarization main beam. Additionally, the cross-polarization levels are ripply and high near broadside in both cases with a similar behavior, which suggests it could be a misalignment issue and that what is being measured is in fact due to extraneous reflections. On the other hand, this experiment shows that it is possible to measure cross-polarization levels down to approximately -45 dB barring any misalignment and reflection issues.

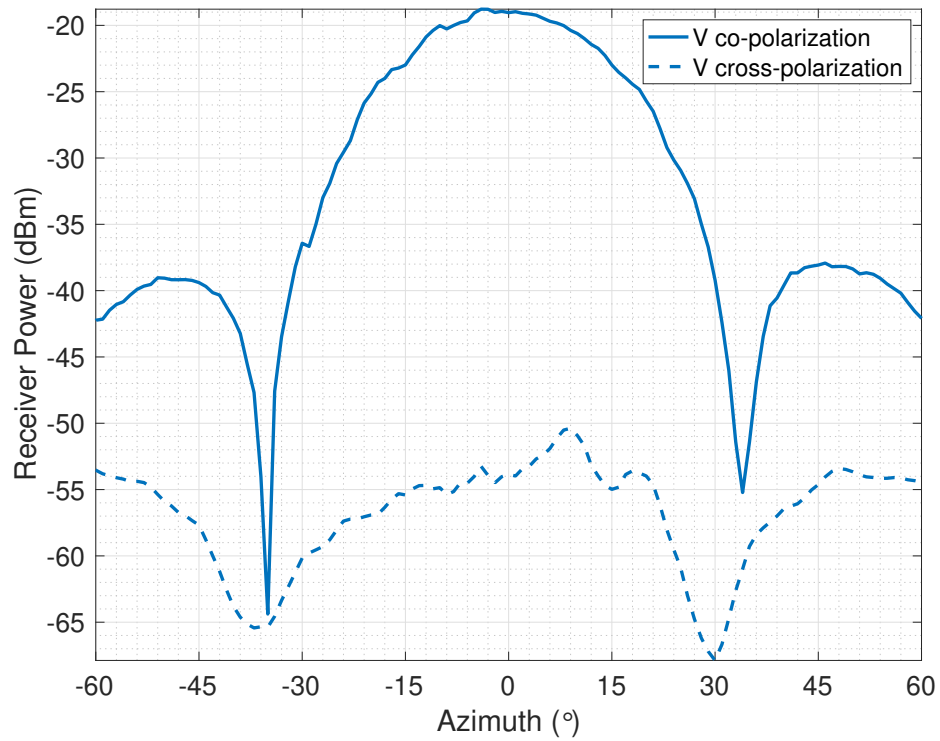
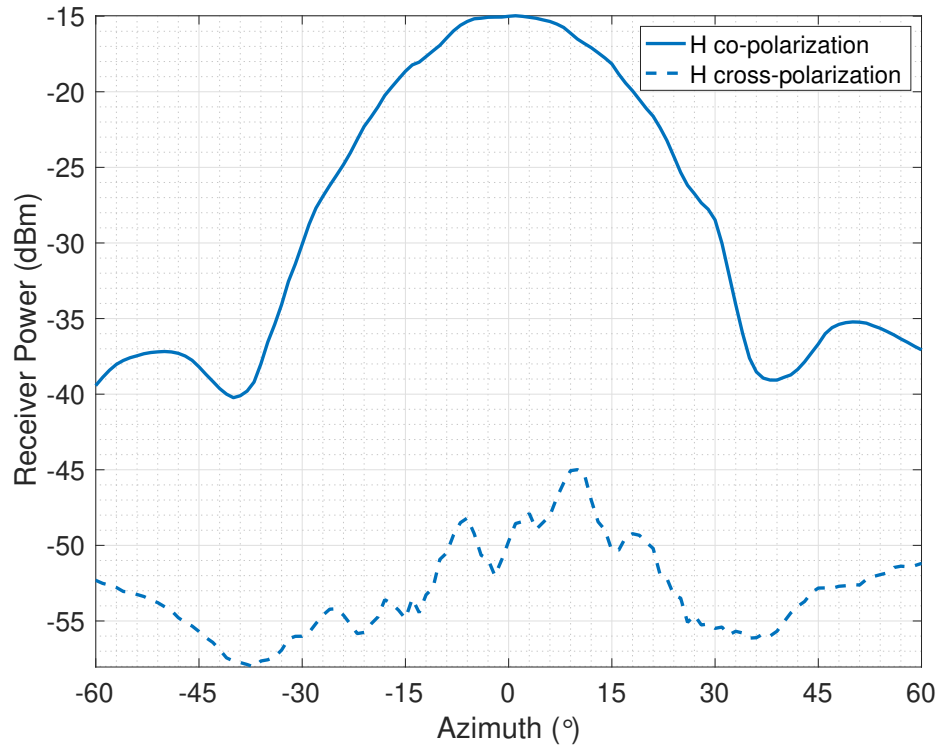


Figure 5.24: SS radiation patterns from UAV-based system in hover mode for H (top) and V (bottom) polarizations. Co-polarization patterns are shown in solid lines, while cross-polarization patterns are shown in dashed lines.

### 5.3.2.3 UAV Circular Mode

Similarly, in circular mode, the same height and range (radius) as the fixed reference is selected with a UAV flight speed of 0.7 m/s (1.6 mph). Figure 5.25 shows H-polarization (E-plane) and V-polarization (H-plane) patterns of both the co- and cross-polarizations taken in different passes in circular mode. In the different passes with the UAV in a circular mission, it is possible to measure up to -38.39 dB in the cross-polarization levels near broadside, and up to -48.46 dB off broadside, for the H-polarization pattern. The V-polarization pattern in cross-polarization was measured with a null down to approximately -62 dB. The co-polarization patterns in all cases are qualitatively reasonable, although it must be indicated that the more comparable the flight precision is to the measurement distance, the larger the error will become, i.e., in this case an uncertainty of approximately  $\pm 2.5$  dB is expected.

Since data is recorded continuously in circular mode with the AUT fixed in place, it is possible to correlate each measurement point to a time and position of the UAV. Thus, it is possible to reconstruct the antenna pattern accurately with adequate post-processing, which involves the correction of the offset of the POI location with the location of the AUT. Consequently, the patterns measured in circular mode are in better alignment with AUT than in hover mode. The shape of the antenna patterns are shown to be consistent between the different circular passes, which emphasize the repeatability of the measurements to a certain extent. The variability in the peak of the main beams are within 0.3 dB, which could be improved with further path-loss based correction. More importantly, the cross-polarization pattern in the V polarization is consistently measured close to or below -45 dB at boresight, which meets the requirements that were set forth as goals for SENSUR. The ripply structure of the H cross-polarization suggests that it could be subject to extraneous reflections or from reflections from the UAV frame itself, although a definite explanation has not yet been found.

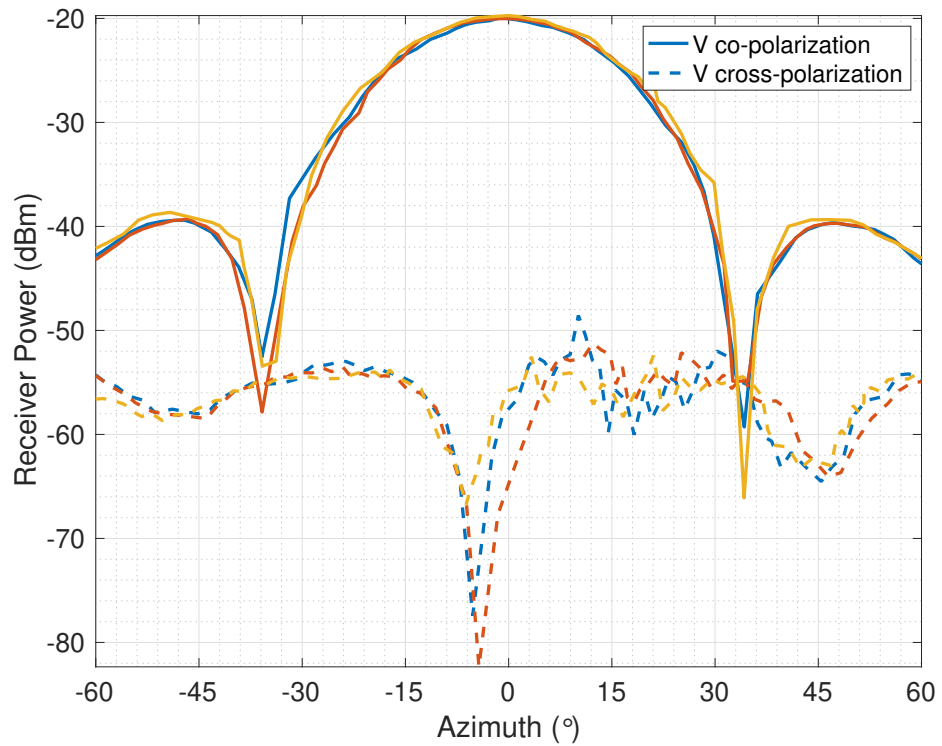
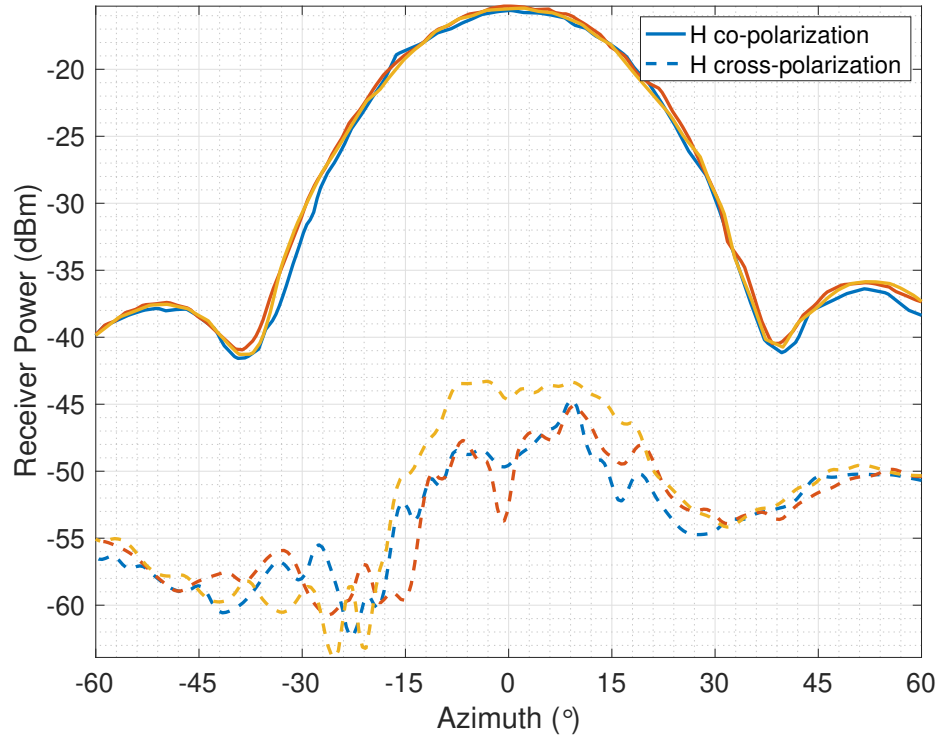


Figure 5.25: SS radiation patterns from UAV-based system in circular mode for H (top) and V (bottom) polarizations. Co-polarization patterns are shown in solid lines, while cross-polarization patterns are shown in dashed lines. Multiple passes are shown overlapped.

#### 5.3.2.4 Analysis

For a useful comparative analysis to be made, the most representative patterns of each case has been selected, as shown in Figure 5.26. The hover mode patterns are outperformed by the circular mode patterns in all cases for this particular setup. A plausible explanation for this is that when the UAV is flying with a non-zero speed, it is less susceptible to perturbations by the wind since the rotors are counteracting the wind force. Thus, assuming a hover precision of approximately  $\pm 20$  cm (approximately 1.2 m excursion with  $3\sigma$ ), the variation in the received power due to the path loss term in the link budget is expected to be within  $\pm 1$  dB, adding more uncertainty in the measurements.

The circular mode patterns are in better agreement with the fixed reference. The peaks of the H co-polarization patterns of the circular mode pattern and the reference are within 0.1 dB, while for the V co-polarization this difference is larger at less than 0.5 dB which can be further corrected by compensating for path loss. The V cross-polarization pattern of the circular mode is able to capture the null in broadside just as well as the reference, below approximately -45 dB, which successfully meets the requirements. However, the shape of the pattern seems slightly broadened, which suggests a projection issue due to the center of the AUT not being coincident with the flight pattern center as predicted.

Lastly, overall the H cross-polarization patterns from both the hover mode and circular mode look qualitatively similar to the reference, albeit with a ripple structure at and a couple of degrees off-broadside. While a plausible explanation for this behavior is most likely reflections off the UAV, this issue might have been amplified by the fact that it was later found that the SS AUT was not properly matched at the H port.

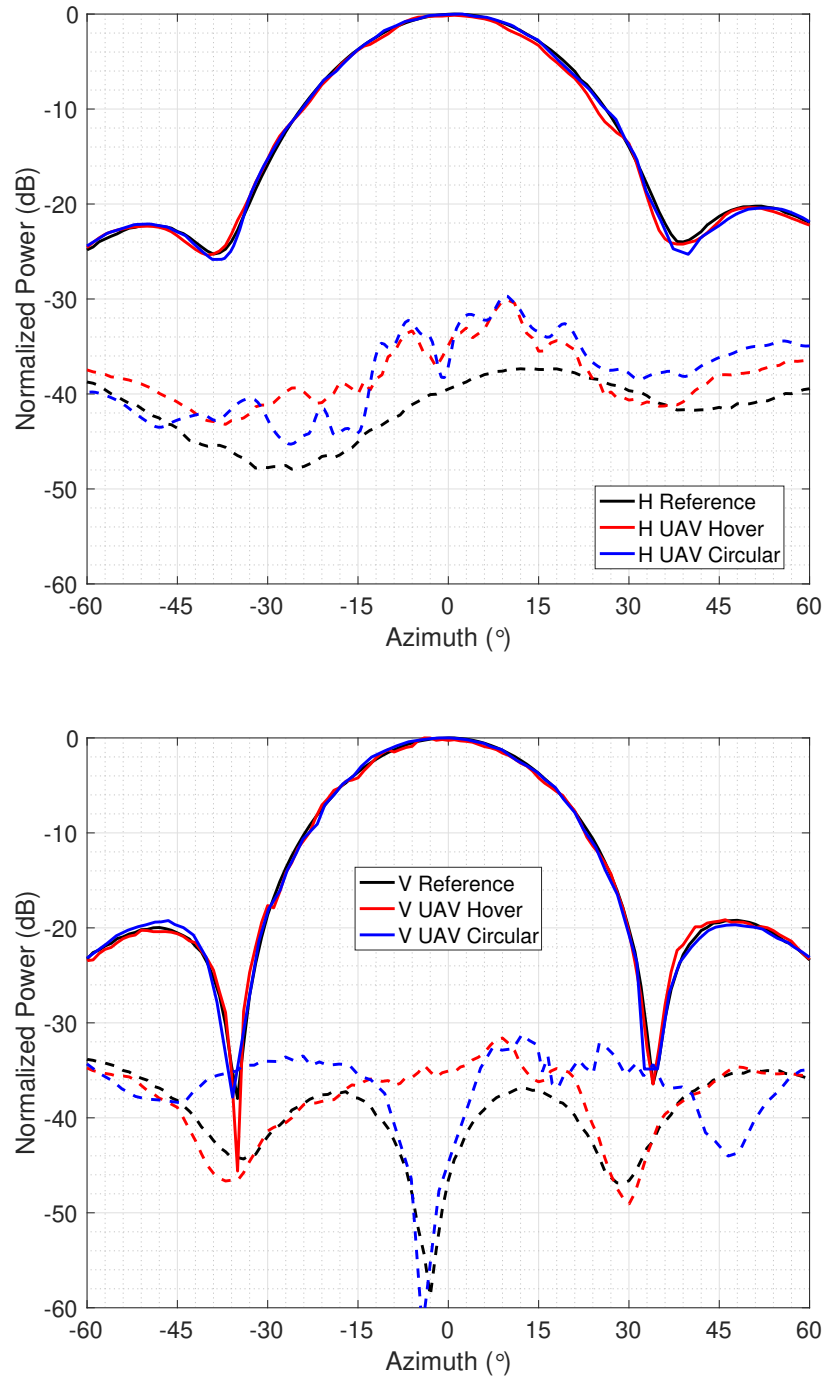


Figure 5.26: A comparison of SS radiation patterns from different sources for H (top) and V (bottom) polarizations. Co-polarization patterns are shown in solid lines, while cross-polarization patterns are shown in dashed lines. Fixed reference is shown in black, UAV-based in hover mode is shown in red, and UAV-based in circular mode is shown in blue.

## 5.4 Summary

The evolution of the platform has been discussed in Section 5.1, which summarized the challenges that were faced from the concept of the UAV-based antenna measurement system to the current status, and the decisions that were taken towards the continuous improvement of the platform. A complete description of the mechanical and RF systems comprising the UAV-based antenna measurement platform has been provided in Section 5.2, with the expected and measured performance indicators of the relevant subsystems. The different components of outdoor operations have been presented in Section 5.3 in terms of the federal and university regulations that are in place to ensure safety during missions, the methodology employed in the different field campaigns, and the results that were obtained during these missions.

With the results presented herein, it has been proven that accurate in-situ UAV-based FF measurements of antenna radiation patterns are possible, with an accuracy of within 0.1 dB of the co-polarization main beam peak (best case scenario), and cross-polarization levels of below -45 dB in broadside. While a circular mode generally showed better results than hover mode, depending on the environmental conditions, there may be a case where hover mode might outperform the circular mode. Moreover, the other flight modes that were discussed but not tested might have better performance, which is worth exploring in the near future. Nevertheless, in the best case scenario, it has been shown that the SENSR requirements can be met with this system.

## Chapter 6

### UAV-based Measurements of Real Systems

The use of polarimetric phased array systems for weather surveillance is still a challenge mainly due to the need of highly accurate polarimetric radar measurements, and this is further limited by the fact that in wide-angle electronic scanning, the beam broadens considerably at large scan angles, and the cross-polarization isolation becomes significantly degraded. To assess the performance of the system, and if necessary, to compensate for any deviations from the main requirements, it is necessary to perform an accurate characterization of the SUT.

The main focus of this chapter will be the use of the UAV-based antenna measurement system for characterizing a real system, and to subsequently analyze the polarimetric calibration capabilities with the results herein obtained. In Chapter 2, the polarimetric system requirements for SENSR/MPAR have been presented with focus on the weather surveillance mission, to establish the optimal requirements that are envisioned to be achieved in terms of the measurement capabilities of the UAV-based system. Additionally, a basic signal model and calibration schemes are then presented to evaluate the performance of the polarimetric calibration technique. In this chapter, real systems (e.g., CPPAR [6]) will be briefly described, and the field campaigns and results obtained will be discussed.

## 6.1 Cylindrical Polarimetric Phased Array Radar (CPPAR)

The results of measuring the antenna pattern of the CPPAR are presented in this section. Previous works [6], [88] involving CPPAR addressed the characterization of the system to assess the polarimetric performance thoroughly, using a fixed FF tower to obtain accurate measurements. Here, the main goal is to study how well the UAV-based system is able to replicate these fixed tower measurements. A brief description of the system is presented first, followed by the methodology and results of the UAV-based measurements of the CPPAR.

The CPPAR demonstrator [6] is a cylindrical array of 2 m in diameter and 2 m in height, populated with 96 columns of 19 dual-polarized, frequency-scanned, aperture-coupled, and stacked patch antennas designed to operate from approximately 2.7 to 3.0 GHz. For each polarization, a stripline structure excites the array elements from coaxial cable ports at the bottom of each column, resulting in an elevation beam scanning from  $0^\circ$  at 2.74 GHz, up to  $13^\circ$  at 2.95 GHz, with a beamwidth of approximately  $6^\circ$  in elevation and  $5.2\text{-}6.0^\circ$  in azimuth, depending on the excitation function.

The system was set to operate at 2.80 GHz frequency, at an elevation of  $6.5^\circ$ , with the beamformer active for 24 columns, for an azimuth scanning angle of  $0^\circ$ , and without calibration. The operation frequency was set to 2.80 GHz to stay as low in elevation as possible, while meeting the bandwidth limitations of the SS antenna. The pedestal of the CPPAR was continuously rotating with an angular velocity of  $18^\circ/\text{s}$ , while 64 pulses were being captured in each direction, with a PRT of 1 ms. For the fixed reference, the test platform is such that two horns (for each polarization) are mounted in FF at a distance of approximately 227 m, and a relative height from the CPPAR of approximately 13.7 m ( $3.3^\circ$  physical elevation), transmitting a CW



Figure 6.1: CPPAR system mounted on the rooftop of the Radar Innovations Laboratory (RIL), and the UAV-based system during a mission.

signal to the radar. This setup range is roughly three times the minimum FF distance required. Figures 6.2 shows the measured patterns in both H and V polarizations. The measurements with the fixed reference were captured in multiple consecutive scans, which are all overlaid with different colors, while the mean of the measurements is shown in a darker shade. The patterns look consistent between scans, except for a few spikes off broadside. The V-polarization power was measured slightly higher than the H-polarization with difference of 7.2 dB at boresight, presumably due to misalignment issues on the FF tower side. Similarly, the cross-polarization levels were measured at -46.20 dB and -44.91 dB for the H and V polarizations, respectively. The co-polarization beam shape is captured adequately, but for cross-polarization, off-broadside, the noise level was too high to capture the structure of the pattern. Nevertheless, for the correction matrix method, only the values near the beam peak are of interest.

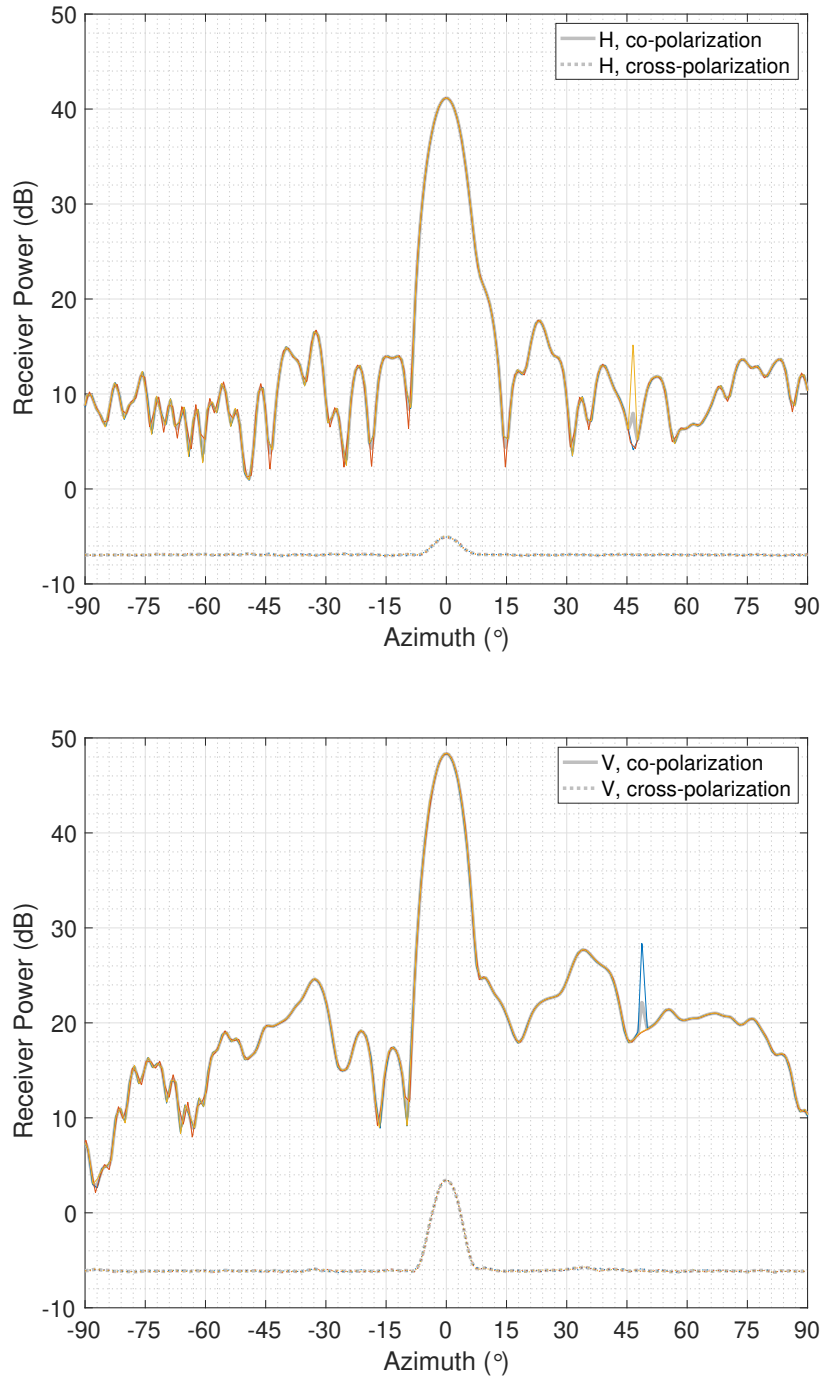


Figure 6.2: CPPAR radiation patterns measured with the FF tower (fixed reference) at 2.80 GHz for conical cuts at  $3.3^\circ$  elevation, a relative height of 13.7 m and range of 227 m. The co- and cross-polarization patterns for H (top) and V (bottom) polarizations are shown as a function of azimuth. Multiple consecutive scans are overlapped (colored) with the mean value (gray).

### 6.1.1 UAV Hover Mode

Due to physical (and regulatory) restrictions surrounding the CPPAR installation site, only the hover mode has been successfully tested. For this mission, the UAV takes off and the POI is set pointing towards the center of the AUT, then the flight range is set to 227 m and 13 m relative height to the POI (physical elevation of  $3.3^\circ$ , similar to FF tower reference). An additional set was measured at a relative height of 26 m which corresponds to the  $6.5^\circ$  elevation of the CPPAR beam at 2.8 GHz. Twitchy (polarimetric switch) was not used in this operation, and two individual missions, one with H-polarized SS and another for V-polarized SS were performed. The flight track from the mission logs is shown in Figures 6.3 and 6.4.

On this day, the wind direction and speed were SSW 25 mph on average, with maximum winds of 38 mph, which is a very undesirable condition in terms of stability. Nevertheless, two short flights of a few minutes in length were possible. It can be seen that the UAV was hovering at a mean relative distance in range from the AUT of 228.4 m and 228.4 m for the first and second flights, respectively, and at a mean relative height of 13.7 m and 14.3 m. The achieved positioning accuracy are 0.54 m, 0.80 m, and 0.12 m, in the  $x$ ,  $y$ , and  $z$  axes, respectively for the H-polarization leg, and 0.71 m, 0.85 m, and 0.19 m for the V-polarization leg. The expected variability in the signal levels due to the instability of the platform at this range is expected to be less than a tenth of a dB. Analogously, for the relative height of 26 m, the mean relative range was 227.6 m and 227.9 m, and the mean relative height was 27.1 m and 28.5 m. The achieved positioning accuracy in the second flight are 0.70 m, 0.34 m, and 0.11 m, in the  $x$ ,  $y$ , and  $z$  axes, respectively for the H-polarization leg, and 1.40 m, 2.02 m, and 0.19 m for the V-polarization leg. The decreased flight precision correlates with the wind conditions worsening throughout the time of the operations.

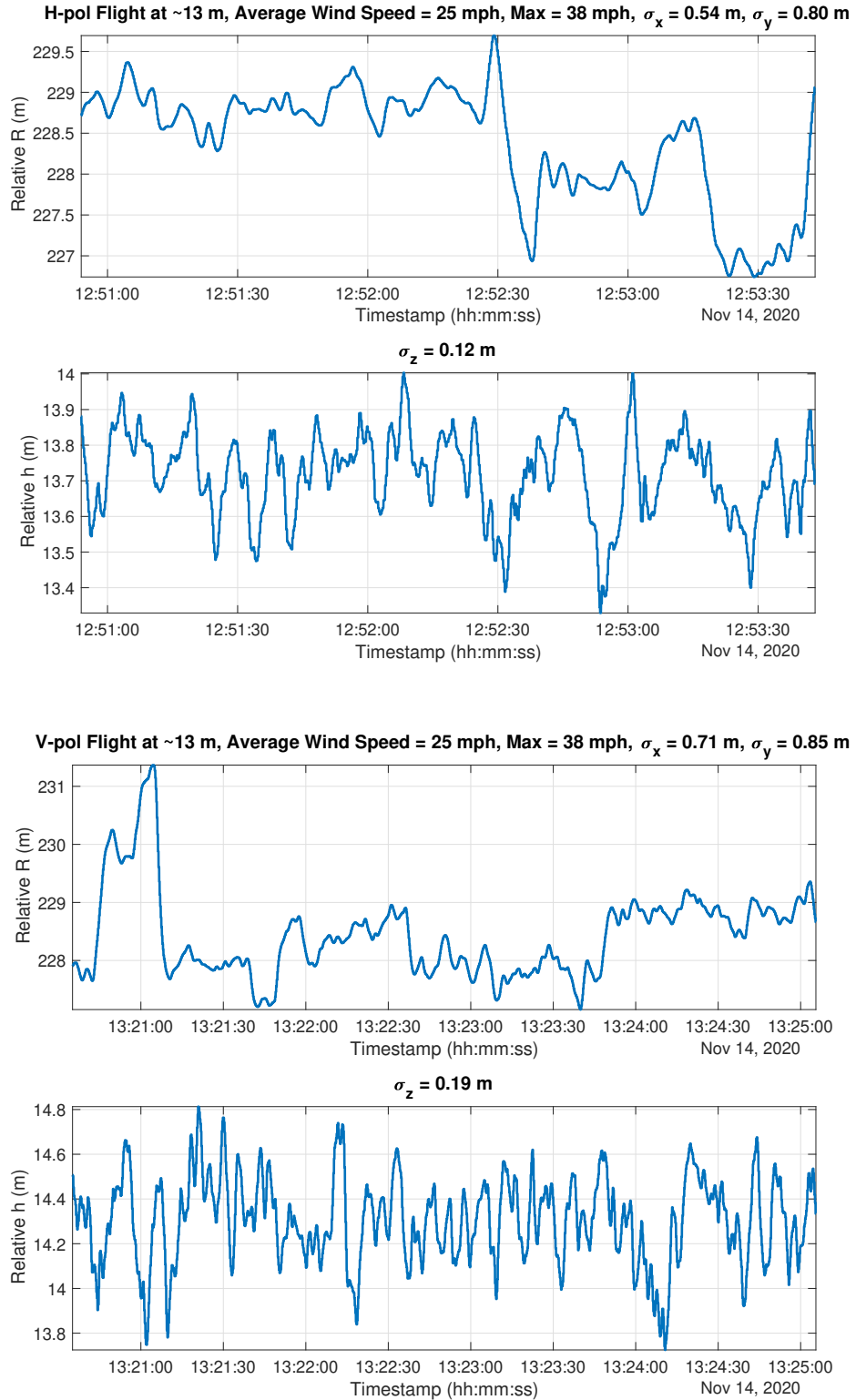


Figure 6.3: Positioning accuracy throughout the operation at ~13 m for H- (top two) and V-polarized (bottom two) probe under average wind speed of 25 mph and gusts at 38 mph. The plots show the range and the height of the UAV relative to the POI at a specific time.

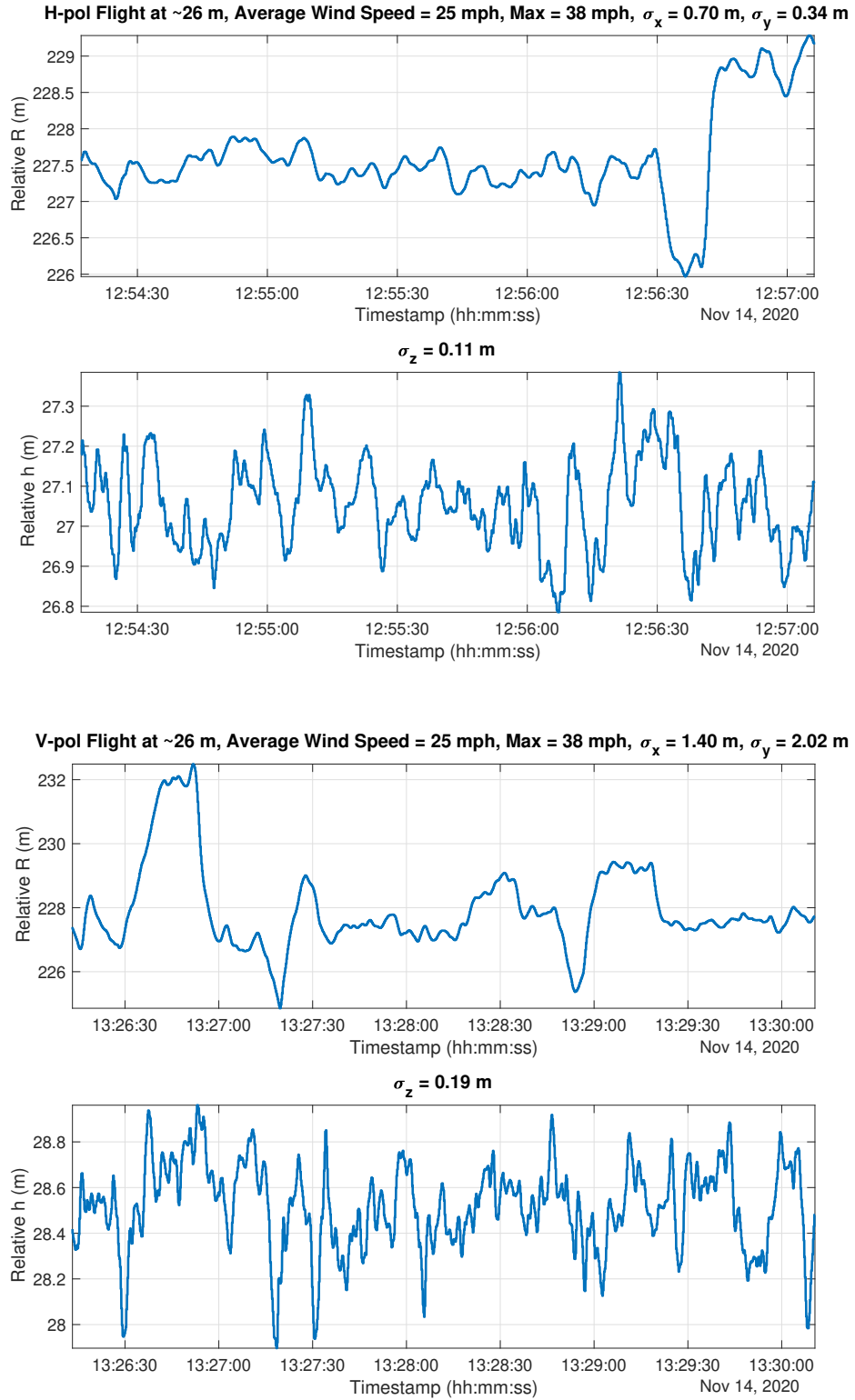


Figure 6.4: Positioning accuracy throughout the operation at  $\sim 26$  m for H- (top two) and V-polarized (bottom two) probe under average wind speed of 25 mph and gusts at 38 mph. The plots show the range and the height of the UAV relative to the POI at a specific time.

For the first mission, the antenna pattern was measured with the CPPAR rotating continuously while acquiring a number of scans of the H-co-polarization and the H-cross-polarization simultaneously. In a similar way, the second mission acquired the V-co-polarization and the V-cross-polarization patterns.

With the flight mission at 13 m, the mismatch between the H- and V-polarization beam peaks is measured at 0.79 dB at boresight, and the cross-polarization levels were measured at -51.63 dB and -45.97 dB for the H and V polarizations, respectively. The V-polarization flight missions were considerably worse with respect to wind conditions, and the spread in the received power levels is larger and more noticeable.

The flight mission at 26 m was tested because the beam direction for the 2.80 GHz frequency of the CPPAR is at  $6.5^\circ$  in elevation. At boresight, the mismatch between the H- and V-polarization beam peaks is measured at 0.34 dB. Similarly, the cross-polarization levels were measured at -52.40 dB and -46.75 dB for the H and V polarizations, respectively.

Overall, the overlapped antenna patterns show good repeatability of the system at broadside, which is critical since the polarimetric correction matrix ingests the values at the beam peak. More importantly, the cross-polarization levels are successfully measured -45 dB below the co-polarization beam peak, which is a critical requirement for polarimetric system characterization.

### **6.1.2 Analysis**

To make a fair comparison, the antenna pattern measured with the UAV at a height of 13 m will be overlapped with the one measured with the FF tower at 13.7 m.

It is observed that in both polarizations, the agreement of the patterns within the main beam is very good. Outside of the main beam, the side lobe structure is captured somewhat accurately in shape, although the levels are slightly different

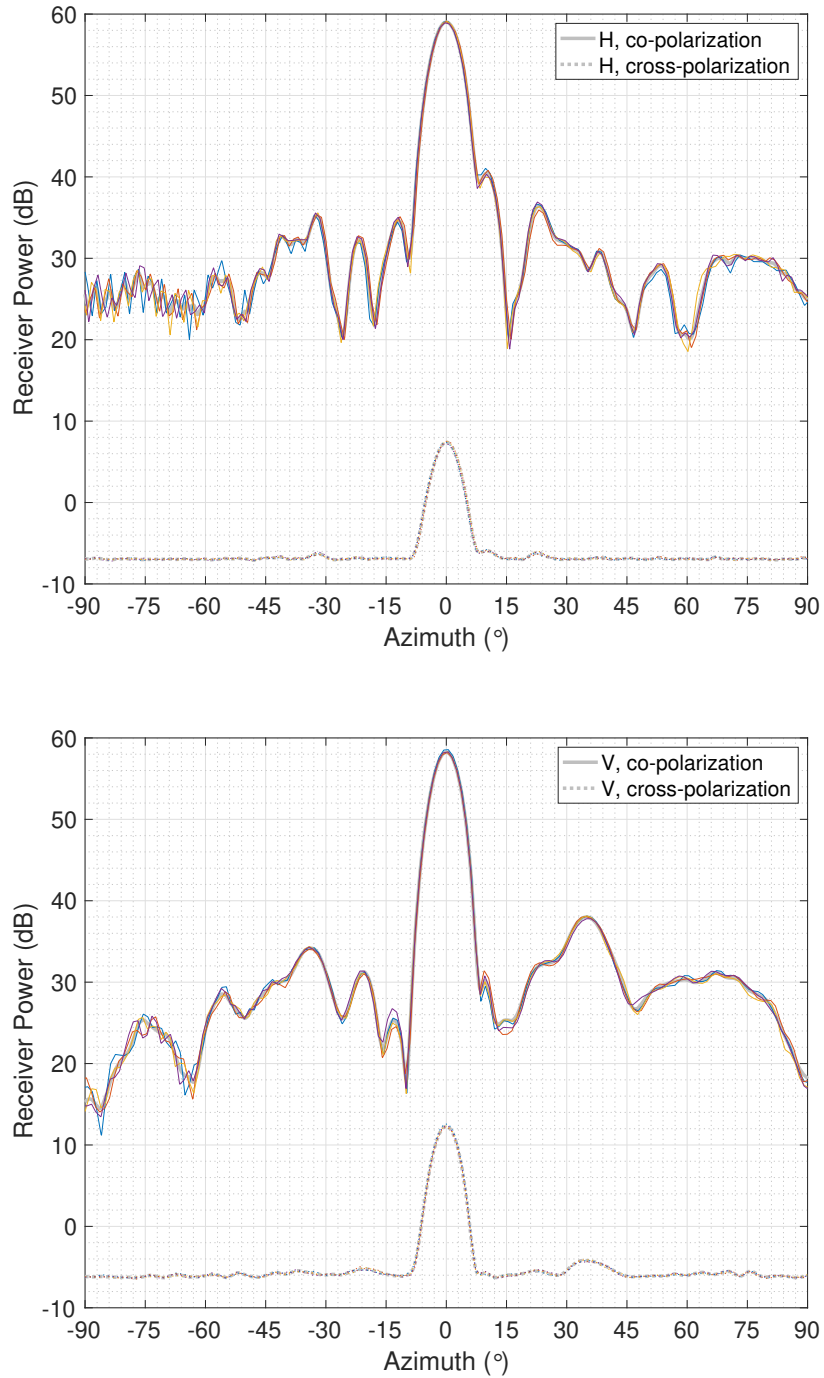


Figure 6.5: CPPAR radiation patterns measured with the UAV at 2.80 GHz for conical cuts at  $3.3^\circ$  elevation, a relative height of 13 m and range of 227 m. The co- and cross-polarization patterns for H (top) and V (bottom) polarizations are shown as a function of azimuth. Multiple consecutive scans are overlapped (colored) with the mean value (gray).

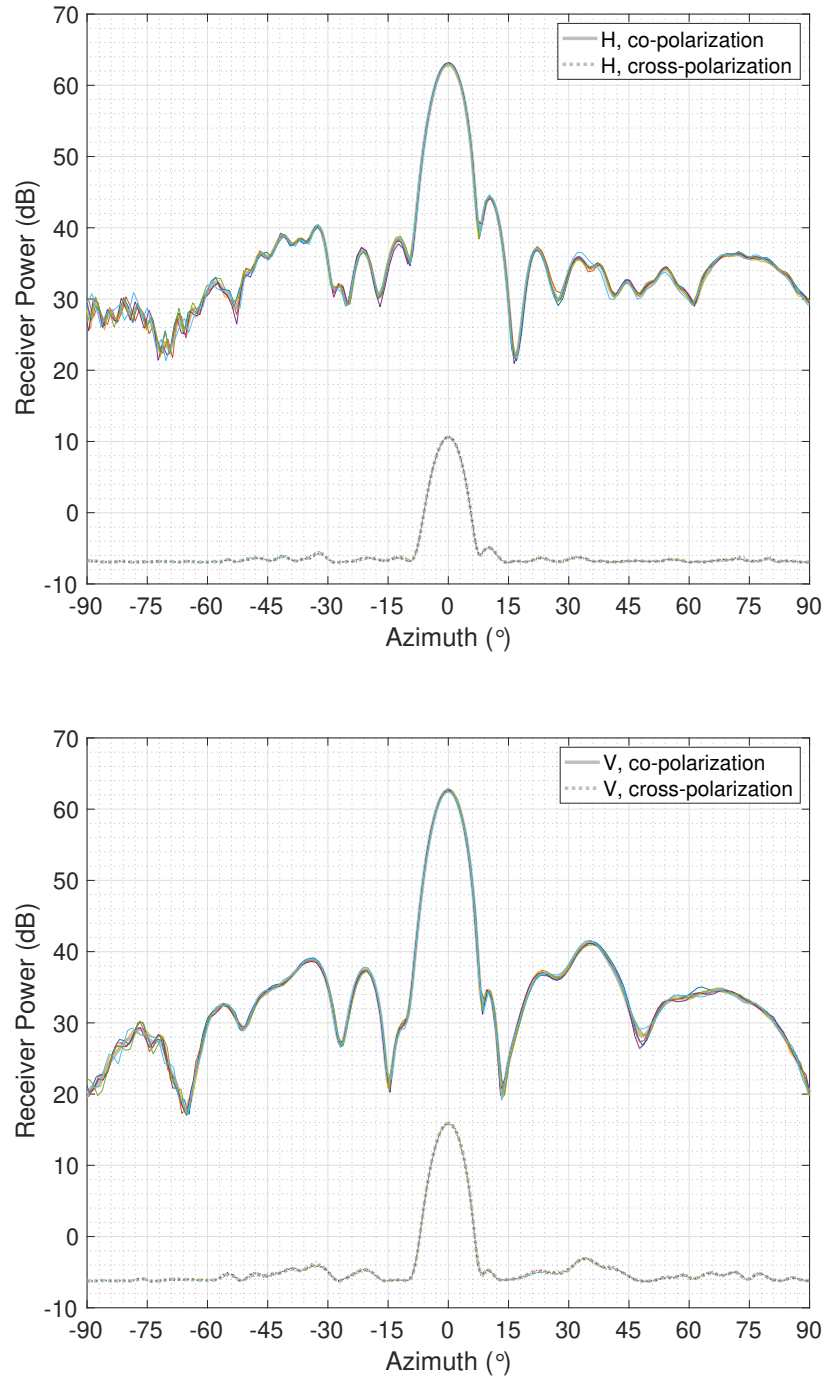


Figure 6.6: CPPAR radiation patterns measured with the UAV at 2.80 GHz for conical cuts at  $6.5^\circ$  elevation, a relative height of 26 m and range of 227 m. The co- and cross-polarization patterns for H (top) and V (bottom) polarizations are shown as a function of azimuth. Multiple consecutive scans are overlapped (colored) with the mean value (gray).

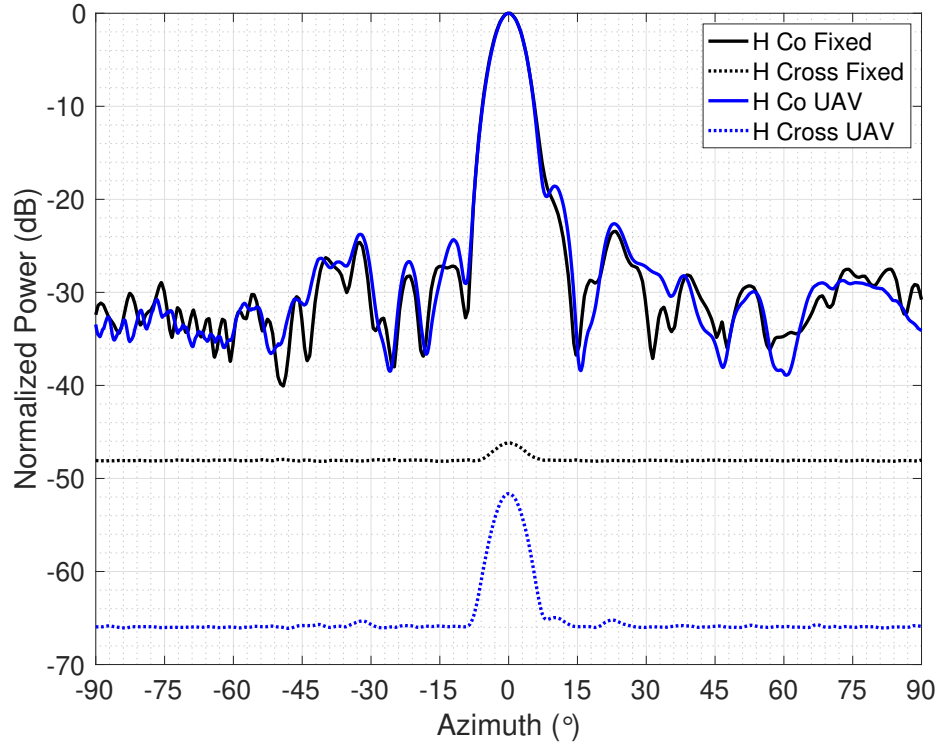


Figure 6.7: CPPAR radiation patterns measured with the FF tower (black) and the UAV (red) at 2.80 GHz for conical cuts at  $3.3^\circ$  elevation, a relative height of  $\sim 13$  m and range of 227 m. The co- and cross-polarization patterns for H (top) and V (bottom) polarizations are shown as a function of azimuth.

because the measurement heights are different, and thus different cuts are being measured essentially. Additionally, farther away from the first side lobes, the FF tower measurements are slightly more affected by reflections, as shown by the ripples, and for the V-polarization pattern, slightly better defined for the UAV-based measurement in terms of the first null. The co-polarization mismatch is measured at approximately 0.8 dB, which can be corrected with the polarimetric calibration matrix method. For the cross-polarization measurements, the UAV-based measurements less vulnerable to the noise, thus having increased sensitivity for the portion corresponding to the main beam of the co-polarization patterns. The cross-polarization levels with the UAV probe are lower than with the FF tower, and this can be explained by the fact that the SS antenna is a very low cross-polarization probe specifically designed for this task, when compared to standard horns. In both cases, the measurements are able to characterize the cross-polarization levels near or below -45 dB near boresight as it was required.

## 6.2 Summary

Although the system was uncalibrated, it was shown that the cross-polarization levels could be measured down to -45 dB at boresight successfully with the fixed reference. Moreover, with the UAV in hover mode, even with very strong winds, the measurements show a good degree of repeatability, with a mismatch in the H- and V-polarization antenna patterns of approximately 0.8 dB at a height of 13 m, and 0.3 dB at a height of 26 m, at the beam peak. More remarkably, the UAV-based measurements were shown to successfully achieve the cross-polarization levels below -45 dB as was desired, producing even better results than the fixed reference. The measurements with the UAV-based system produce the necessary data to be ingested in the calibration matrices method, to achieve the desired system-level polarimetric calibration.

With the results presented herein, it was successfully demonstrated that the UAV-based antenna characterization system is capable of obtaining accurate measurements of a real system, in order to assess its performance to make sure it meets the minimum requirements and to calibrate if necessary.

## Chapter 7

### Epilogue

#### 7.1 Conclusion

The main focus throughout this work was achieving accurate UAV-based FF antenna measurements for the characterization of radiation patterns of systems such as polarimetric weather radars, and in particular, of phased array systems, as a means to assess the RF performance of the MPAR systems to be deployed as the replacement of current dish-based radar systems in the WSR-88D network as part of the SENSR multi-agency program. The motivation and problem statement was formulated in the first chapter, addressing the need of a highly accurate in-situ measurement system capable of being deployed at multiple radar sites at a low cost, with the minimal requirements set as the ability to characterize mismatches down to 0.1 dB in the co-polarization, and below approximately -45 dB for cross-polarization patterns. With UAV-based RF measurement technologies becoming increasingly popular in the past decade, a solution was proposed that will hypothetically meet these stringent requirements.

A proper formulation of the guidelines for accurate FF measurements have been adapted from conventional outdoor ranges to a UAV-based system. This set of criteria helps minimizing the uncertainties added in the measurements generally due to extraneous reflections, tapering over the AUT aperture, and phase curvature effects.

Moreover, a simulation framework has been developed with relevant signal and transmission models for polarimetric antenna measurements, with the added error sources due to coupling, ground and UAV frame reflections, and positioning and orientation misalignment. The simulated case studies for the error analyses included an ideal fixed probe scenario similar to an elevated range setup, a mobile probe scenario analogous to the probe antenna mounted on a UAV under wind effects, and a phased array scanning scenario to assess the polarimetric beam mismatch. The simulations provide a simple way to analyze the effects of position and orientation misalignment and the error bounds in different scenarios. Overall, it has been found with the results from Chapter 3, that accurate characterization of antenna and radar systems in FF is feasible, as long as the probe antenna performance is sufficient, and the UAV flight is stable enough for the duration of the mission. If the above were found to be insufficient in simulations, a careful assessment can be made whether a probe antenna with better performance or a more stable UAV platform (implying better hardware or wind conditions) is required.

The different types of probe antennas that could potentially be used for this application have also been studied through EM simulations and indoor chamber measurements. It has been found that, in general, the wider the beamwidth of the antenna mounted on the UAV, the more ripples and higher cross-polarization contamination it produces. As such, depending on the beamwidth requirements of the particular measurement application, a careful selection of the probe antenna must be made such that the coupling with the UAV and gimbal structure be minimized. An important tradeoff to note is that the narrower the probe beamwidth, the higher tapering will occur along the AUT aperture, which may lead to additional errors. Moreover, if the probe antenna's beamwidth is too wide, the illuminating field may induce currents in surrounding structures causing additional extraneous reflections. From a mechanical point of view, larger antenna apertures lead to narrower beamwidth, but this also

means a larger and heavier antenna, which in turn diminishes the flight performance of the UAV. Finally, the co- and cross-polarization antenna patterns of the probe antenna are slightly affected by the relative orientation between the UAV frame and the gimbal. This adds an additional constraint that can further limit the operational capabilities of the system, however, it has been found that if the range of operation of the gimbal is limited to within a few degrees from the nominal boresight orientation, the RF performance of the probe is predictable and within the requirement bounds.

A predecessor to this work [31] provided a proof of concept, highlighting the capabilities and limitations of a UAV-based antenna measurement platform and polarimetric calibration for a mobile weather radar in X band. From the conception of this prototype to the current system, many iterations have been tested, and valuable lessons learned, with continuous improvement to reach the minimal measurement requirements. The evolution of each prototype has been briefly discussed in regards to the key takeaways and the limiting factors that drove to the ultimate need of an upgrade to a better platform. The system in its current state has been described in detail in terms of all of its components. As a complement to the engineering challenges, the non-scientific operational regulations that are dictated by the FAA for UAV-based missions have been briefly discussed. The methods for the flight missions that have been tested and validated in field, in addition to those theoretically possible ones, have been given a proper discussion, in terms of the accuracy and their practical implementation with the current mission planner applications. Finally, the field campaigns that yielded successful results in validating the effectiveness of the UAV-based antenna measurement system have been presented and the results obtained were compared to a fixed (best case) reference for an outdoor setting. It has been found that, depending on the wind condition and measurement procedure, the circular mode can provide better results than a hover mode, both qualitatively and quantitatively. However, there are advantages and disadvantages to each method,

mostly constrained by the operational regulations imposed by the authorities. Nevertheless, the measured co- and cross-polarization patterns were found to be in great agreement with the reference, and it has been proven that accurate antenna pattern characterization using UAVs can be achieved.

Finally, a case study where a real system's antenna patterns are measured was presented. The purpose was to study the feasibility of performing accurate UAV-based characterization of actual polarimetric weather radar systems with stringent polarimetric requirements. The results presented herein for the CPPAR system showed that, albeit some system-level limitations on the CPPAR side, the radiation patterns captured with the UAV-based system were in fairly good agreement with the reference FF-tower-measured patterns, up to a couple of degrees off boresight. However, since the basic correction matrix method only requires the information at the beam peak of the radiation patterns, this is sufficient to prove that polarimetric calibration with a UAV-based system can be successfully achieved.

The main contributions of this dissertation are summarized next:

- A cost-effective, mobile, in-situ UAV-based FF antenna characterization system for polarimetric weather radar applications.
- A formal compilation of guidelines and considerations for FF antenna measurements using UAV.
- A simulation framework for UAV-based antenna measurements for qualitative and quantitative analysis of potential error sources.
- A study on the EM scattering effects between the UAV structure and different probe antenna types, for the development of strategies to mitigate undesired reflections.
- A guideline for field practices, regulatory and operational considerations.

- A means for accurate in-situ polarimetric calibration.

To conclude, some remarks on possible future work will be presented.

## 7.2 Future Work

It should be clear that the work presented here only scratches the surface of the realm of capabilities of a UAV-based antenna characterization system, leaving ample room for future work and improvements upon the system. The discussion herein will be divided into what can be improved in each of the chapters of this dissertation considering the results that were obtained, and what alternative approach or application it may be useful for.

Chapter 3 presented a formal design guideline and requirements of a UAV-based antenna characterization system in FF, from a theoretical perspective backed with a simulation framework to assess the expected error levels in the field. The simulation framework uses ideal antenna patterns to present a study of the RF errors that may be incurred due to extraneous reflections, positioning and orientation misalignment due to the wind, and other factors. A way to improve upon this framework is by ingesting actual measured patterns instead of ideal ones to better assess the accuracy of the measurement effort outdoors. Additionally, the ground reflection model used is very simple and may not produce realistic results, although they are sufficient for this context to evaluate the possible type of perturbations that can be expected. Other more complex ways to improve upon the main contributions of this include but are not limited to:

- Extend the error analysis to other operating frequencies (generalize for different applications).
- More detailed simulation the transmitted/received pulses between the AUT and the probe antenna in the form of simulated ADC or I/Q signals.

- Increased terrain complexity by using mapped terrain models for a given location, and with the aid of EM solvers for accurate ray tracing.
- Implementing more environmental conditions and flight patterns, or extending the current feature to be able to import actual flight data to produce synthetic measurements.
- Explore the feasibility of NF measurements with a similar treatment.

In short, the future work in this chapter mainly relates to improving each of the module of the simulation framework and further exploring the capabilities of using the UAV-based system for NF measurements.

Chapter 4 presented a study on the effects of the UAV frame and gimbal on the antenna pattern of the probe antenna for different types of antennas, through EM simulations and supported by indoor measurements. A number alternative methods to improve the radiation characteristics of the UAV-mounted probe have been studied in this context, including:

- Use of flared structures in addition to the probe antenna.
- Placement of adequate RF absorbers in areas with higher induced surface currents in the structure.
- Offsetting the gimbal position relative to the UAV frame.

However, a proper formulation of contamination mitigation strategies (to reduce the ripples in the radiation patterns, and the cross-polarization levels from the UAV frame), and definite proof of their effectiveness still remains. Furthermore, a theoretical modeling of the extraneous radiation phenomenon from the UAV structure may help accelerate this system characterization process.

In terms of the flight strategies and methodology presented in Chapter 5 for outdoor operations, a customized mission planner software with more precise gimbal

tuning, waypoint design, and automated controls may be developed that is tailored exactly to the needs for performing RF measurements. Additionally, more control on the transmitter and receiver hardware will help accelerate the measurement and post-processing considerably. This also implies the implementation of measurement modes with improved signal processing strategies to mitigate many factors that add uncertainty in the measurements.

For the contents of Chapter 6 and calibration related improvements, further testing with other systems will be required, as well as element-level characterization of the system to study the feasibility of using the UAV-based system to produce accurate element-level calibration of any given antenna or radar system. Additionally, other system characterization functionality such as radome inspection, point-target calibration, may be incorporated in the platform, or be readily available as exchangeable equipment for the gimbal payload, to provide a complete characterization suite.

As a final remark, if most of the above suggestions are addressed in the near future, a very robust and sophisticated UAV-based characterization platform can be envisioned as a standalone solution for any desired RF application.

## Bibliography

- [1] A. Y. Umeyama, J. L. Salazar-Cerreno, and C. J. Fulton, “UAV-based far-field antenna pattern measurement method for polarimetric weather radars: Simulation and error analysis,” *IEEE Access*, vol. 8, pp. 191 124–191 137, 2020. DOI: 10.1109/ACCESS.2020.3027790.
- [2] A. Y. Umeyama, J. L. Salazar-Cerreno, and C. Fulton, “UAV-based antenna measurements for polarimetric weather radars: Probe analysis,” *IEEE Access*, vol. 8, pp. 191 862–191 874, 2020. DOI: 10.1109/ACCESS.2020.3027779.
- [3] J. E. Stailey and K. D. Hondl, “Multifunction phased array radar for aircraft and weather surveillance,” *Proceedings of the IEEE*, vol. 104, no. 3, pp. 649–659, 2016.
- [4] C. Fulton, J. Salazar, D. Zrnic, D. Mirkovic, I. Ivic, and D. Doviak, “Polarimetric phased array calibration for large-scale multi-mission radar applications,” in *2018 IEEE Radar Conference (RadarConf18)*, IEEE, 2018, pp. 1272–1277.
- [5] D. J. McLaughlin, E. A. Knapp, Y. Wang, and V. Chandrasekar, “Distributed weather radar using X-band active arrays,” in *2007 IEEE Radar Conference*, IEEE, 2007, pp. 23–27.
- [6] C. Fulton, J. L. Salazar, Y. Zhang, G. Zhang, R. Kelly, J. Meier, M. McCord, D. Schmidt, A. D. Byrd, L. M. Bhowmik, *et al.*, “Cylindrical Polarimetric Phased Array Radar: Beamforming and calibration for weather applications,” *IEEE Transactions on Geoscience and Remote Sensing*, vol. 55, no. 5, pp. 2827–2841, 2017.

- [7] T. D. Crum and R. L. Albery, “The WSR-88D and the WSR-88D operational support facility,” *Bulletin of the American Meteorological Society*, vol. 74, no. 9, pp. 1669–1688, 1993.
- [8] G. Zhang, R. J. Doviak, D. S. Zrnic, J. Crain, D. Staiman, and Y. Al-Rashid, “Phased array radar polarimetry for weather sensing: A theoretical formulation for bias corrections,” *IEEE transactions on geoscience and remote sensing*, vol. 47, no. 11, pp. 3679–3689, 2009.
- [9] D. Zrnić, R. Doviak, G. Zhang, and A. Ryzhkov, “Bias in differential reflectivity due to cross coupling through the radiation patterns of polarimetric weather radars,” *Journal of Atmospheric and Oceanic Technology*, vol. 27, no. 10, pp. 1624–1637, 2010.
- [10] M. D. Hudlow, R. K. Farnsworth, and P. R. Ahnert, “NEXRAD technical requirements for precipitation estimation and accompanying economic benefits,” 1985.
- [11] Y. Wang and V. Chandrasekar, “Polarization isolation requirements for linear dual-polarization weather radar in simultaneous transmission mode of operation,” *IEEE Transactions on Geoscience and Remote Sensing*, vol. 44, no. 8, pp. 2019–2028, 2006.
- [12] I. R. Ivić, “An approach to simulate the effects of antenna patterns on polarimetric variable estimates,” *Journal of Atmospheric and Oceanic Technology*, vol. 34, no. 9, pp. 1907–1934, 2017.
- [13] E. E. A. S. Committee, *IEEE standard test procedures for antennas*, 1979. Institute of Electrical & Electronics Engineers (IEEE), 1979, vol. 149.
- [14] J. S. Hollis, T. Lyon, and L. Clayton, *Microwave antenna measurements*. Scientific-Atlanta, 1970.
- [15] C. A. Balanis, *Antenna Theory: Analysis and Design*. Wiley-Interscience, 2005.

- [16] S. T. P. Duthoit, *UAV-Based In Situ Antenna Characterization: Analysis and Design Requirements*. Master's Thesis, 2018.
- [17] J. Steele, "Measurement of antenna radiation patterns using a tethered balloon," *IEEE Transactions on Antennas and Propagation*, vol. 13, no. 1, pp. 179–180, 1965.
- [18] J.-E. Lejerkranz and F. Enquist, "Field strength measurement and antenna radiation pattern plotting using heli-borne equipment," in *1988 International Broadcasting Convention, IBC 1988*, IET, 1988, pp. 137–142.
- [19] R. Manton and K. Beeke, "HF antenna radiation patterns over real terrain," in *1988 International Broadcasting Convention, IBC 1988*, IET, 1988, pp. 143–147.
- [20] G. Virone, A. M. Lingua, M. Piras, A. Cina, F. Perini, J. Monari, F. Paonessa, O. A. Peverini, G. Addamo, and R. Tascone, "Antenna pattern verification system based on a micro unmanned aerial vehicle (UAV)," *IEEE Antennas and Wireless Propagation Letters*, vol. 13, pp. 169–172, 2014.
- [21] G. Virone, F. Paonessa, O. A. Peverini, G. Addamo, R. Orta, R. Tascone, A. Lingua, M. Piras, P. Bolli, G. Pupillo, *et al.*, "Antenna pattern measurement with UAVs: Modeling of the test source," in *2016 10th European Conference on Antennas and Propagation (EuCAP)*, IEEE, 2016, pp. 1–3.
- [22] F. Paonessa, G. Virone, P. Bolli, G. Pupillo, J. Monari, F. Perini, A. Mattana, G. Naldi, M. Poloni, M. Schiaffino, *et al.*, "The UAV-based test source as an end-to-end verification tool for aperture arrays," in *2016 International Conference on Electromagnetics in Advanced Applications (ICEAA)*, IEEE, 2016, pp. 886–889.

- [23] F. Paonessa, G. Virone, E. Capello, G. Addamo, O. A. Peverini, R. Tascone, P. Bolli, G. Pupillo, J. Monari, M. Schiaffino, *et al.*, “VHF/UHF antenna pattern measurement with unmanned aerial vehicles,” in *2016 IEEE Metrology for Aerospace (MetroAeroSpace)*, IEEE, 2016, pp. 87–91.
- [24] F. Paonessa, G. Virone, I. Aicardi, A. Lingua, M. Piras, P. Maschio, P. Bolli, G. Addamo, O. Peverini, R. Orta, *et al.*, “Recent results in antenna pattern measurement with UAVs,” in *2015 International Conference on Electromagnetics in Advanced Applications (ICEAA)*, IEEE, 2015, pp. 720–721.
- [25] G. Virone, F. Paonessa, E. Capello, O. Peverini, G. Addamo, R. Tascone, R. Orta, M. Orefice, A. Lingua, M. Piras, *et al.*, “UAV-based antenna and field measurements,” in *2016 IEEE Conference on Antenna Measurements & Applications (CAMA)*, IEEE, 2016, pp. 1–3.
- [26] G. Virone, F. Paonessa, O. Peverini, G. Addamo, R. Orta, R. Tascone, and P. Bolli, “Antenna pattern measurements with a flying far-field source (hexacopter),” in *2014 IEEE Conference on Antenna Measurements & Applications (CAMA)*, IEEE, 2014, pp. 1–2.
- [27] G. Virone, F. Paonessa, A. Tibaldi, Z. Farooqui, G. Addamo, O. A. Peverini, R. Tascone, P. Bolli, A. Mattana, J. Monari, *et al.*, “UAV-based radiation pattern verification for a small low-frequency array,” in *2014 IEEE Antennas and Propagation Society International Symposium (APSURSI)*, IEEE, 2014, pp. 995–996.
- [28] F. Paonessa, G. Virone, G. Addamo, O. A. Peverini, R. Tascone, E. de Lera Acedo, E. Colín-Beltrán, N. Razavi-Ghods, P. Bolli, G. Pupillo, *et al.*, “UAV-based pattern measurement of the SKALA,” in *2015 IEEE International Symposium on Antennas and Propagation & USNC/URSI National Radio Science Meeting*, IEEE, 2015, pp. 1372–1373.
- [29] F. Üstüner, E. Aydemir, E. Güleç, M. İlarıslan, M. Çelebi, and E. Demirel, “Antenna radiation pattern measurement using an unmanned aerial vehicle

- (UAV),” in *2014 XXXIth URSI General Assembly and Scientific Symposium (URSI GASS)*, IEEE, 2014, pp. 1–4.
- [30] A. M. Picar, C. Marqué, M. Anciaux, H. Lamy, and S. Ranvier, “Antenna pattern calibration of radio telescopes using an UAV-based device,” in *2015 International Conference on Electromagnetics in Advanced Applications (ICEAA)*, IEEE, 2015, pp. 981–984.
- [31] S. Duthoit, J. L. Salazar, W. Doyle, A. Segales, B. Wolf, C. Fulton, and P. Chilson, “A new approach for in-situ antenna characterization, radome inspection and radar calibration, using an unmanned aircraft system (UAS),” in *2017 IEEE Radar Conference (RadarConf)*, IEEE, 2017, pp. 0669–0674.
- [32] M. García-Fernández, Y. Á. López, A. Arboleya, B. González-Valdés, Y. Rodríguez-Vaqueiro, M. E. D. C. Gómez, and F. L.-H. Andrés, “Antenna diagnostics and characterization using unmanned aerial vehicles,” *IEEE Access*, vol. 5, pp. 23 563–23 575, 2017.
- [33] G. Pupillo, G. Naldi, G. Bianchi, A. Mattana, J. Monari, F. Perini, M. Poloni, M. Schiaffino, P. Bolli, A. Lingua, *et al.*, “Medicina array demonstrator: Calibration and radiation pattern characterization using a UAV-mounted radio-frequency source,” *Experimental Astronomy*, vol. 39, no. 2, pp. 405–421, 2015.
- [34] J. L. Salazar, A. Umeyama, S. Duthoit, and C. Fulton, “UAS-based antenna pattern measurements and radar characterization,” in *2018 IEEE Conference on Antenna Measurements & Applications (CAMA)*, IEEE, 2018, pp. 1–4.
- [35] A. Y. Umeyama, J. L. Salazar-Cerreño, B. M. Wolf, and C. J. Fulton, “Recent development in UAV-based antenna pattern characterization for weather radars,” in *2019 IEEE Conference on Antenna Measurements & Applications (CAMA)*, IEEE, 2019, pp. 199–202.

- [36] J. Yin, P. Hoogeboom, C. Unal, H. Russchenberg, F. van der Zwan, and E. Oudejans, “UAV-aided weather radar calibration,” *IEEE Transactions on Geoscience and Remote Sensing*, vol. 57, no. 12, pp. 10 362–10 375, 2019.
- [37] E. De Lera Acedo, P. Bolli, F. Paonessa, G. Virone, E. Colin-Beltran, N. Razavi-Ghods, I. Aicardi, A. Lingua, P. Maschio, J. Monari, *et al.*, “SKA aperture array verification system: Electromagnetic modeling and beam pattern measurements using a micro UAV,” *Experimental Astronomy*, vol. 45, no. 1, pp. 1–20, 2018.
- [38] P. Bolli, G. Pupillo, F. Paonessa, G. Virone, S. J. Wijnholds, and A. M. Lingua, “Near-field experimental verification of the EM models for the LOFAR radio telescope,” *IEEE Antennas and Wireless Propagation Letters*, vol. 17, no. 4, pp. 613–616, 2018.
- [39] M. G. Fernandez, Y. A. Lopez, and F. L.-H. Andres, “On the use of unmanned aerial vehicles for antenna and coverage diagnostics in mobile networks,” *IEEE Communications Magazine*, vol. 56, no. 7, pp. 72–78, 2018.
- [40] M. Garcia-Fernandez, Y. A. Lopez, and F. L.-H. Andres, “Unmanned aerial system for antenna measurement and diagnosis: Evaluation and testing,” *IET Microwaves, Antennas & Propagation*, vol. 13, no. 13, pp. 2224–2231, 2019.
- [41] M. García Fernández, Y. Álvarez López, and F. Las-Heras, “Dual-probe near-field phaseless antenna measurement system on board a UAV,” *Sensors*, vol. 19, no. 21, p. 4663, 2019.
- [42] A. Martínez Picar, C. Marqué, M. Anciaux, and H. Lamy, “Directional pattern measurement of the BRAMS beacon antenna system,” 2015.
- [43] P. Bolli, F. Paonessa, G. Pupillo, G. Virone, M. Arts, A. Lingua, J. Monari, and S. Wijnholds, “Antenna pattern characterization of the low-frequency receptor of LOFAR by means of an UAV-mounted artificial test source,” in *Ground-based and Airborne Telescopes VI*, International Society for Optics and Photonics, vol. 9906, 2016, p. 99063V.

- [44] G. Virone, F. Paonessa, O. A. Peverini, G. Addamo, P. Bolli, and E. de Lera Acedo, “UAV-based technique for the characterization of the Intrinsic Cross-Polarization Ratio (IXR),” in *2017 11th European Conference on Antennas and Propagation (EUCAP)*, IEEE, 2017, pp. 3825–3828.
- [45] P. Bolli, S. J. Wijnholds, E. de Lera Acedo, A. Lingua, J. Monari, F. Paonessa, G. Pupillo, and G. Virone, “In-situ characterization of international low-frequency aperture arrays by means of an UAV-based system,” in *2017 XXXIIInd General Assembly and Scientific Symposium of the International Union of Radio Science (URSI GASS)*, IEEE, 2017, pp. 1–4.
- [46] F. Paonessa, G. Virone, P. Bolli, G. Pupillo, S. Wijnholds, S. Matteoli, A. Lingua, M. Piras, I. Aicardi, and P. Maschio, “Recent results on the characterization of the LOFAR radio telescope by means of a micro UAV,” in *2017 International Conference on Electromagnetics in Advanced Applications (ICEAA)*, IEEE, 2017, pp. 1752–1753.
- [47] F. Paonessa, G. Virone, S. Matteoli, P. Bolli, G. Pupillo, S. J. Wijnholds, A. M. Lingua, G. Addamo, and O. A. Peverini, “In-situ verification of aperture-array polarimetric performance by means of a micro UAV: Preliminary results on the LOFAR low band antenna,” in *2018 2nd URSI Atlantic Radio Science Meeting (AT-RASC)*, IEEE, 2018, pp. 1–4.
- [48] L. Van Hoorebeeck, J. Cavillot, H. Bui-Van, F. Glineur, C. Craeye, and E. de Lera Acedo, “Near-field calibration of SKA-Low stations using unmanned aerial vehicles,” in *2019 13th European Conference on Antennas and Propagation (EuCAP)*, IEEE, 2019, pp. 1–5.
- [49] L. Ciorba, G. Virone, F. Paonessa, S. Matteoli, P. Bolli, E. de Lera Acedo, N. R. Ghods, J. Abraham, E. C. Beltrán, K. Z. Adami, *et al.*, “Near-field phase reconstruction for UAV-based antenna measurements,” in *2019 13th European Conference on Antennas and Propagation (EuCAP)*, IEEE, 2019, pp. 1–4.

- [50] G. Virone, F. Paonessa, S. Matteoli, L. Ciorba, G. Addamo, O. Peverini, G. Pupillo, E. de Lera Acedo, E. Colín-Beltrán, N. R. Ghods, *et al.*, “The SKA aperture array verification system: Measured digitally-beam-formed radiation patterns,” in *2019 IEEE International Symposium on Antennas and Propagation and USNC-URSI Radio Science Meeting*, IEEE, 2019, pp. 395–396.
- [51] S. J. Wijnholds, G. Pupillo, P. Bolli, and G. Virone, “UAV-aided calibration for commissioning of phased array radio telescopes,” in *2016 URSI Asia-Pacific Radio Science Conference (URSI AP-RASC)*, IEEE, 2016, pp. 228–231.
- [52] F. Paonessa, G. Virone, P. Bolli, G. Addamo, S. Matteoli, and O. A. Peverini, “UAV-based antenna measurements: Improvement of the test source frequency behavior,” in *2018 IEEE Conference on Antenna Measurements & Applications (CAMA)*, IEEE, 2018, pp. 1–3.
- [53] F. Paonessa, G. Virone, P. Bolli, and A. M. Lingua, “UAV-based antenna measurements: Scan strategies,” in *2017 11th European Conference on Antennas and Propagation (EUCAP)*, IEEE, 2017, pp. 1303–1305.
- [54] F. Paonessa, G. Virone, A. M. Lingua, M. Piras, I. Aicardi, P. Maschio, O. A. Peverini, G. Addamo, R. Orta, R. Tascone, *et al.*, “Effect of the UAV orientation in antenna pattern measurements,” in *2015 9th European Conference on Antennas and Propagation (EuCAP)*, IEEE, 2015, pp. 1–2.
- [55] J. Schreiber, “Antenna pattern reconstitution using unmanned aerial vehicles (UAVs),” in *2016 IEEE Conference on Antenna Measurements & Applications (CAMA)*, IEEE, 2016, pp. 1–3.
- [56] M. Garcia-Fernandez, Y. Alvarez-Lopez, and F. Las-Heras, “UAV-based antenna measurement and diagnostics for circularly polarized antenna arrays,” in *2018 IEEE International Symposium on Antennas and Propagation & USNC/URSI National Radio Science Meeting*, IEEE, 2018, pp. 525–526.

- [57] M. G. Fernández, Y. Á. López, and F. L.-H. Andrés, “Antenna measurement and diagnostics processing techniques using unmanned aerial vehicles,” in *2019 13th European Conference on Antennas and Propagation (EuCAP)*, IEEE, 2019, pp. 1–5.
- [58] M. G. Fernández, Y. Á. López, and F. L.-H. Andrés, “Advances in antenna measurement and characterization using unmanned aerial vehicles,” in *2019 13th European Conference on Antennas and Propagation (EuCAP)*, IEEE, 2019, pp. 1–5.
- [59] T. Fritzel, H. Steiner, J. Habersack, H. Schippers, and J. Ferrante, “Antenna pattern measurements of full-size air vehicles with an airborne near-field test facility (ANTF),” in *European Test & Telemetry Conference, ETTC*, 2005.
- [60] T. Fritzel, R. Strauß, H.-J. Steiner, C. Eisner, and T. Eibert, “Introduction into an UAV-based near-field system for in-situ and large-scale antenna measurements,” in *2016 IEEE Conference on Antenna Measurements & Applications (CAMA)*, IEEE, 2016, pp. 1–3.
- [61] V. Klassen, B. Levitan, I. Prosvirkin, and S. Topchiev, “Development of hardware and software complex for measurement of direction patterns of large aperture antennas with the use of unmanned aerial vehicle and GLONASS system,” in *2016 International Conference on Engineering and Telecommunication (EnT)*, IEEE, 2016, pp. 80–85.
- [62] J. M. Miller and E. Decrossas, “Using small unmanned aerial systems and helium aerostats for far-field radiation pattern measurements of high-frequency antennas,” in *2018 IEEE Conference on Antenna Measurements Applications (CAMA)*, 2018, pp. 1–4.
- [63] C. Wasserzier, J. G. Worms, and D. W. O’Hagan, “A concept for far field measurements of large dimension antennas in an open area test site performed by UAS,” in *2019 20th International Radar Symposium (IRS)*, 2019, pp. 1–10.

- [64] F. Paonessa, G. Virone, A. Sarri, K. Dell’Omodarme, L. Fiori, G. Addamo, S. Matteoli, and O. A. Peverini, “UAV-mounted corner reflector for in-situ radar verification and calibration,” in *2018 IEEE Conference on Antenna Measurements Applications (CAMA)*, 2018, pp. 1–4.
- [65] C. J. Fulton, “Digital array radar calibration and performance monitoring techniques for direct conversion and dual polarization architectures,” PhD thesis, Purdue University, 2011.
- [66] R. Doviak, V. Bringi, A. Ryzhkov, A. Zahrai, and D. Zrnić, “Considerations for polarimetric upgrades to operational WSR-88D radars,” *Journal of Atmospheric and Oceanic Technology*, vol. 17, no. 3, pp. 257–278, 2000.
- [67] G. F. Masters and S. F. Gregson, “Coordinate system plotting for antenna measurements,” in *AMTA Annual Meeting & Symposium*, 2007.
- [68] N. A. Aboserwal, J. L. Salazar, and C. Fulton, “Current polarization impact on cross-polarization definitions for practical antenna elements,” in *2016 IEEE International Symposium on Phased Array Systems and Technology (PAST)*, 2016, pp. 1–5. DOI: 10.1109/ARRAY.2016.7832550.
- [69] H. T. Friis, “A note on a simple transmission formula,” *proc. IRE*, vol. 34, no. 5, pp. 254–256, 1946.
- [70] R. J. Mailloux, *Phased array antenna handbook*. Artech house, 2017.
- [71] R. J. Doviak *et al.*, *Doppler radar and weather observations*. Courier Corporation, 2006.
- [72] V. N. Bringi and V. Chandrasekar, *Polarimetric Doppler weather radar: principles and applications*. Cambridge university press, 2001.
- [73] A. Y. Umeyama Matsumoto, “The bootstrap dual polarimetric spectral density estimator,” 2016.

- [74] M. R. Kumjian, “Principles and applications of dual-polarization weather radar. part i: Description of the polarimetric radar variables.,” *Journal of Operational Meteorology*, vol. 1, 2013.
- [75] L. Lei, G. Zhang, and R. J. Doviak, “Bias correction for polarimetric phased-array radar with idealized aperture and patch antenna elements,” *IEEE Transactions on Geoscience and Remote Sensing*, vol. 51, no. 1, pp. 473–486, 2012.
- [76] A. Byrd, “Simulation of polarimetric phased array weather radars,” 2016.
- [77] C. Cutler, A. King, and W. Kock, “Microwave antenna measurements,” *Proceedings of the IRE*, vol. 35, no. 12, pp. 1462–1471, 1947.
- [78] V. Chandrasekar and R. J. Keeler, “Antenna pattern analysis and measurements for multiparameter radars,” *Journal of Atmospheric and Oceanic Technology*, vol. 10, no. 5, pp. 674–683, 1993.
- [79] D. J. Wasielewski, I. R. Ivic, and J. R. Mendoza, “Calibration of a dual-polarization planar phased-array radar using a far-field tower,” in *99th American Meteorological Society Annual Meeting*, AMS, 2019.
- [80] Y. Wu and W. Huang, “Studies and analysis on unintentional electromagnetic radiation of UAV,” in *2015 IEEE 6th International Symposium on Microwave, Antenna, Propagation, and EMC Technologies (MAPE)*, IEEE, 2015, pp. 479–482.
- [81] A. Rizwan, D. Biswas, and V. Ramachandra, “Impact of UAV structure on antenna radiation patterns at different frequencies,” in *2017 IEEE International Conference on Antenna Innovations & Modern Technologies for Ground, Aircraft and Satellite Applications (iAIM)*, IEEE, 2017, pp. 1–5.
- [82] E. Ngai, A. Fenn, A. Eapen, and E. Newman, “Radiation characteristics of small antennas on small UAV platforms,” in *IEEE Antennas and Propagation Society Symposium, 2004.*, IEEE, vol. 1, 2004, pp. 173–176.

- [83] A. V. Khristenko, M. O. Konovalenko, M. E. Rovkin, V. A. Khlusov, A. V. Marchenko, A. A. Sutulin, and N. D. Malyutin, “Magnitude and spectrum of electromagnetic wave scattered by small quadcopter in X-band,” *IEEE transactions on antennas and propagation*, vol. 66, no. 4, pp. 1977–1984, 2018.
- [84] W. C. Jakes and D. C. Cox, *Microwave mobile communications*. Wiley-IEEE Press, 1994.
- [85] J. Cihlar and F. T. Ulaby, “Dielectric properties of soils as a function of moisture content,” 1974.
- [86] A. Mancini, J. L. Salazar, R. M. Lebrón, and B. L. Cheong, “A novel instrument for real-time measurement of attenuation of weather radar radome including its outer surface. part i: The concept,” *Journal of Atmospheric and Oceanic Technology*, vol. 35, no. 5, pp. 953–973, 2018.
- [87] C. Boyer and C. Fulton, “UAV-based calibration for polarimetric phased array radar,” in *(poster) 16th Annual AMS Student Conference*, 2017.
- [88] H. Saeidi Manesh, “High-performance antenna arrays for multifunction phased array radar (MPAR) application,” 2019.

# Appendix A

## Part 107 Regulations

To conduct UAV operations with small UAS (unmanned aircraft systems) the FAA established rules in Part 107<sup>1</sup> regarding the use of UAVs weighing less than 55 lbs, covering a broad spectrum of commercial and government uses. The following is an extract from the summary of the Part 107 rules for small unmanned aircraft, with certain additional details that pertain to UAV operations for scientific research and under the authority of the University of Oklahoma.

### A.1 General

Part 107 does not apply to:

- Model aircraft that satisfy all of the criteria specified in Section 336 of Public Law 112-95.
- Public aircraft.
- Section 44807 exempted aircraft operating under regulations.
- Air carrier operations.

---

<sup>1</sup>Part 107 refers to the proposed part 107 of Chapter 14 of the Code of Federal Regulations, i.e., 14 CFR Part 107.

The rule codifies the FAA’s enforcement authority in Part 101 by by prohibiting model aircraft operators from endangering the safety of the NAS.

## A.2 Operational Limitations

- Unmanned aircraft must weigh less than 55 lbs (25 kg).
- Visual line-of-sight (VLOS) only; the unmanned aircraft must remain within VLOS of the remote pilot in command (RPIC) and the person manipulating the flight controls of the small UAS. Alternatively, the unmanned aircraft must remain within VLOS of the visual observer.
- At all times the small unmanned aircraft must remain close enough to the RPIC and the person manipulating the flight controls of the small UAS for those people to be capable of seeing the aircraft with vision unaided by any device other than corrective lenses.
- Small unmanned aircraft may not operate over any persons not directly participating in the operation, not under a covered structure, and not inside a covered stationary vehicle.
- Daylight-only operations, or civil twilight (30 minutes before official sunrise to 30 minutes after official sunset, local time) with appropriate anti-collision lighting.
- Must yield right of way to other aircraft.
- May use visual observer (VO) but not required.
- First-person view camera cannot satisfy “see-and-avoid” requirement but can be used as long as requirement is satisfied in other ways.
- Maximum ground speed of 100 mph (87 knots).

- Maximum altitude of 400 feet above ground level (AGL) or, if higher than 400 feet AGL, remain within 400 feet of a structure.
- Minimum weather visibility of 3 miles from control station.
- Operations in Class B, C, D and E airspace are allowed with the required ATC (air traffic control) permission.
- Operations in Class G airspace are allowed without ATC permission.
- No person may act as a RPIC or VO for more than one unmanned aircraft operation at one time.
- No operations from a moving aircraft.
- No operations from a moving vehicle unless the operation is over a sparsely populated area.
- No careless or reckless operations.
- No carriage of hazardous materials.
- Requires preflight inspection by the RPIC.
- A person may not operate a small unmanned aircraft if he or she knows or has reason to know of any physical or mental condition that would interfere with the safe operation of a small UAS.
- Foreign-registered small unmanned aircraft are allowed to operate under Part 107 if they satisfy the requirements of Part 375.
- External load operations are allowed if the object being carried by the unmanned aircraft is securely attached and does not adversely affect the flight characteristics or controllability of the aircraft.

- Transportation of property for compensation or hire allowed provided that:
  - The aircraft, including its attached systems, payload and cargo weigh less than 55 pounds total;
  - The flight is conducted within visual line of sight and not from a moving vehicle or aircraft; and
  - The flight occurs wholly within the bounds of a State and does not involve transport between (1) Hawaii and another place in Hawaii through airspace outside Hawaii; (2) the District of Columbia and another place in the District of Columbia; or (3) a territory or possession of the United States and another place in the same territory or possession.
- Most of the restrictions discussed above are waivable if the applicant demonstrates that his or her operation can safely be conducted under the terms of a certificate of waiver.

### **A.3 Remote Pilot in Command Certification and Responsibilities**

- Establishes a RPIC position.
- A person operating a small UAS must either hold a remote pilot airman certificate with a small UAS rating or be under the direct supervision of a person who does hold a remote pilot certificate (RPIC).
- To qualify for a remote pilot certificate, a person must:
  - Demonstrate aeronautical knowledge by either:
    - \* Passing an initial aeronautical knowledge test at an FAA-approved knowledge testing center; or

- \* Hold a Part 61 pilot certificate other than student pilot, complete a flight review within the previous 24 months, and complete a small UAS online training course provided by the FAA.
- Be vetted by the Transportation Security Administration.
- Be at least 16 years old.
- Part 61 pilot certificate holders may obtain a temporary remote pilot certificate immediately upon submission of their application for a permanent certificate. Other applicants will obtain a temporary remote pilot certificate upon successful completion of TSA security vetting. The FAA anticipates that it will be able to issue a temporary remote pilot certificate within 10 business days after receiving a completed remote pilot certificate application.
- Until international standards are developed, foreign-certificated UAS pilots will be required to obtain an FAA-issued remote pilot certificate with a small UAS rating.

A RPIC must:

- Make available to the FAA, upon request, the small UAS for inspection or testing, and any associated documents/records required to be kept under the rule.
- Report to the FAA within 10 days of any operation that results in at least serious injury, loss of consciousness, or property damage of at least \$500.
- Conduct a preflight inspection, to include specific aircraft and control station systems checks, to ensure the small UAS is in a condition for safe operation.
- Ensure that the small unmanned aircraft complies with the existing registration requirements specified in §91.203(a)(2).

A RPIC may deviate from the requirements of this rule in response to an in-flight emergency.

## **A.4 Aircraft Requirements**

FAA airworthiness certification is not required. However, the RPIC must conduct a preflight check of the small UAS to ensure that it is in a condition for safe operation.

## **A.5 University Research Operation Requirements**

In addition to the above provisions, as part of the University of Oklahoma's risk management guidelines for UAV operations, certain additional requirements must be met prior to conducting field operations. For the sake of brevity, only those non-overlapping rules are listed here.

- UAS operating under the University's authority must meet University's operating requirements for aircraft maintenance and pre-flight and post-flight inspections.
- All UAS must be registered with the FAA and operated by an appropriately licensed RPIC. The license must be in the RPIC's possession and available for inspection at the time of the flight.
- University's Norman Campus is located almost entirely within five (5) miles of Max Westheimer Airport. The RPIC must obtain approval from the airport before flight and must comply with all airport directives throughout the flight.
- Applicants must submit evidence of the RPIC's proficiency with the make/model of the UAS proposed to be used, unless the UAS weighs less than five (5) pounds. For this purpose, to be considered proficient in the operation of a particular make/model of UAS, the RPIC must have logged evidence of a minimum of

five (5) hours of flight time using said make/model of UAS, and have logged at least three (3) take-offs and landings. RPICs who are otherwise qualified but lack evidence of proficiency with a particular make/model of UAS can make arrangements to practice at a safe location until proficiency can be demonstrated.

- UAS operations may not take place within 500 feet of non-participating people unless adequate safety measures have been undertaken to protect them. This requirement may be waived for good cause shown. It is the applicant's responsibility to demonstrate that waiver of this requirement is essential for the operation and that the flight is designed to ensure safety of people and property.
- UAS operations may not generally take place within 400 feet of a building/structure or vehicles, unless adequate safety measures have been undertaken to protect them and the executive officer with authority over the building/structure agrees to the operation.
- UAS operations must cease immediately if severe weather or high winds threaten the integrity of the operation.
- UAS operations are prohibited on home football game days and special event days.
- UAS operations should be scheduled, when possible, at times when the risk of nonparticipating persons coming within range of the UAS is minimized (e.g., weekends, before/after business hours).
- UAS operated by third party vendors must provide a certificate of insurance identifying the University of Oklahoma as a certificate holder.

Additionally, since the UAVs used in the framework of the project are property of the University of Oklahoma, they are insured through OU Risk Management, which requires flightworthiness certification.